Development of novel laser diagnostic techniques for the quantitative study of premixed flames

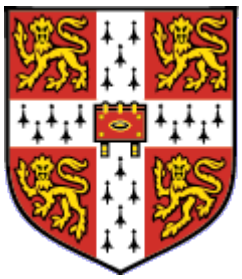

Robin Simon MacPherson Chrystie

Jesus College

University of Cambridge

A thesis submitted for the degree of

Doctor of Philosophy

October 2009

Development of novel laser diagnostic techniques for the quantitative study of premixed flames

Robin S.M. Chrystie

Summary

The main topic of this thesis concerns the development and application of laser diagnostic techniques for accurate temperature measurements and for the determination of flamefront properties in premixed flames that can serve as input data for computational fluid dynamical (CFD) models in technical combustion. The work comprises of a number of related studies, to address problems of relevance in the field of combustion research.

The first part of this work involves the development and testing of an improved method for the computation of flamefront curvature in lean premixed turbulent flames. Measurements of spatially resolved heat release rate along the flamefront were then compared with the curvature data and it could be shown that a significant correlation exists between local rate of heat release and flamefront curvature. The results here agree with predictions from CFD models and improve on previous experimental attempts to find a correlation between curvature and heat release.

In the second part of this work, the focus was shifted towards the development and application of improved thermometry techniques. One study was on the improvement and application of a coherent anti-Stokes Raman spectroscopy (CARS) setup to an acoustically-forced turbulent lean premixed flame stabilised on a burner, whose design was modelled to mimic phenomena of relevance in industrial combustors. In a related previous study reported in the literature two-line OH planar laser induced fluorescence had been applied to this flame and it was suspected that the results were inaccurate. Using CARS, these inaccuracies could be verified, amounting to discrepancies in temperature of up to 47% compared to the true temperatures.

A major effort towards the end of this project was focused on the improvement of traditional thermometry techniques, in order to make them more accurate, faster, and spatially resolved. A technique based on indium two-line atomic fluorescence (TLAF) thermometry was developed and applied, which employed a novel extended cavity diode laser design, and it was shown for the first time that temperature measurements with high accuracy and precision could be performed in low pressure sooting flames without recourse to calibration. Both the high precision and accuracy of the technique allowed for the deduction that the temperature in the flames studied here is relatively insensitive to changes in pressure in stark contrast to the soot volume fraction.

Finally, it is shown for the first time that low power diode lasers can be used in combination with indium TLAF to measure spatially and temporally highly resolved temperatures in a quasi-continuous fashion. We demonstrated such measurements at effective rates of 3.5 kHz in a steady laminar test flame yielding an unprecedented precision of 1.5 % at ~2000 K at this measurement rate.

Preface

This dissertation is the result of my own work and includes nothing which is the outcome of work done in collaboration except where specifically indicated in the text.

In total, this document contains approximately 43,000 words and 50 figures, and does not exceed the word limit stated by the Engineering degree committee.

I confirm that the work contained in this dissertation, or any part thereof, has not been submitted for any other degree.

The research presented here has been carried out at the Department of Chemical Engineering and Biotechnology, University of Cambridge between October 2005 and December 2008.

Reason is the illusion of reality.

Hazrat Inayat Khan

Acknowledgements

I would like to express my gratitude to the following people and organisations:

Iain burns, who has served as my technical supervisor during my project. It has been a real pleasure working with Iain. He has provided direction and a deep interest in my work. Thanks also to Iain for organising our research visit to the University of Lille and inspiring me to learn the language of French.

Johan Hult, for his unrelenting zeal and extensive knowledge of optical physics. His patience and clear explanations have been invaluable.

Clemens Kaminski, for the opportunity to work on this interesting project, and for his continuous dynamism and support.

Babatunde Ayoola, for the provision of his experimental dataset and useful discussions.

Georg Hartung, for providing experimental training, motivation and guidance.

All other members of the Laser Analytics Group for providing an engaging research environment.

The UK Engineering and Physical Sciences Research Council (EPSRC) and Rolls-Royce plc. for providing a CASE studentship.

My family and friends for their encouragement and support.

List of Publications

Part of this work has been presented and/or submitted for publication elsewhere:

1. **CHRYSTIE, R.S.M.,** BURNS, I.S., HULT, J. & KAMINSKI, C.F**.**
   "On the improvement of two-dimensional curvature computation and its application to turbulent premixed flame correlations"
   Measurement Science and Technology, 19, 125503 (2008)

2. **CHRYSTIE, R.S.M.,** BURNS, I.S., HULT, J. & KAMINSKI, C.F.
   "High-repetition-rate combustion thermometry with two-line atomic fluorescence excited by diode lasers"
   Optics Letters, 34(16), 2492 (2009)

3. **CHRYSTIE, R.S.M.,** BURNS, I.S., CANT, R.S., ARMITAGE, C.A. & KAMINSKI, C.F.
   "Coherent anti-Stokes Raman Scattering temperature validation of CFD for turbulent acoustically-forced lean premixed flames"
   Experiments in Fluids, (awaiting publication)

4. BURNS, I.S., **CHRYSTIE, R.S.M.,** MERCIER, X., WARTEL, M., FACCINETTO, A., DESGROUX, P., LAMOUREUX, N., HULT, J. & KAMINSKI, C.F.
   "Accurate spatially-resolved thermometry in low-pressure sooting flames by two-line atomic fluorescence"
   Optics Letters, (awaiting publication)

5. **CHRYSTIE, R.S.M.**, BURNS, I.S., HULT, J. & KAMINSKI, C.F.
   "CARS measurements in an acoustically-forced lean premixed ethylene-air flame"
   Presented at GRC, Oxford (2007)

6. **CHRYSTIE, R.S.M.**, BURNS, I.S., HULT, J. & KAMINSKI, C.F.
   "CARS temperature measurements in an acoustically-forced burner"
   Presented at IOP Young Researchers Meeting, Loughborough (2007)

Contents

Chapter 1

Introduction

For the foreseeable future, combustion will continue to be the chief means of deriving energy for electrical power and transport (Stern 2007). In light of increasingly stringent legislation on emissions, engineers face the challenge of designing combustion units featuring greater efficiency, whilst also constraining oxides of nitrogen (NO_X) and soot emission (Veynante and Vervisch 2002). An understanding of combustion and underlying flame phenomena is fundamental to improve upon combustor design. Despite the use of combustion over millennia, there are still many aspects that are not properly understood. This is attributable to the complex coupling of heat and mass transport, chemical reactions and turbulence that render realistic combustion systems difficult to computationally model.

1.1 Modelling challenges

Computational modelling of combustion is important, because it forms an integral part of gaining an understanding of flame phenomena, through the prediction of quantities such as temperature, composition and flow-field

velocities. Such prediction permits improved combustor design and performance. The advantage of modelling offers a way to design combustors without recourse to costly and time consuming fabrication of prototypes. Despite the appeal of the power and convenience of modelling, there are a number of shortcomings. These are attributable to limitations in current computational power, and hence the need to make assumptions in the models to render them computationally tractable. The assumptions originate from the need to simplify the tremendous complexity of combustion dynamics, especially in the turbulent case. Turbulence on its own has been difficult to understand and been a subject of investigation for many years in the scientific community. However, the presence of simultaneous chemical reactions in flames magnifies the complexity of the coupling between the flow-field dynamics, and the heat and mass transfer effects. With this in mind, most attempts to model flames have not hitherto provided reliable predictions of temperature, soot volume fractions and NO_X concentrations (Chakraborty and Cant 2005). It is therefore paramount to be able to improve and validate current models by acquiring high fidelity experimental data to which computations can be compared.

1.2 Need for accurate diagnostics

To be useful in model validation, experimental data is required to be both accurate and precise, due to the sensitivity of the flame dynamics in models to variables such as temperature, composition and local velocities (Veynante and Vervisch 2002). To add to this challenge, experimental data is also required to be spatially- and temporally- well resolved because of the inhomogeneous and

rapidly fluctuating scalar and flow fields within the combustion gases. Traditional approaches to measuring temperature and concentrations involved the use of probes, which are invasive and lead to inaccurate results. However, the generation of laser diagnostics has largely overcome these problems (Eckbreth 1996; Kohse-Höinghaus *et al.* 2005). Such diagnostics are employed widely today, owing to the improved reliability and availability of modern laser systems. Typically, laser techniques involve the focussing of a beam within the flame and then detecting either absorption, laser induced fluorescence or Raman scattering within the flame, for instance. Hitherto, most of these techniques have relied on the use of powerful lasers, which are bulky, expensive and complex to operate. However within this decade, there have been developments in the use of diode lasers for flame thermometry (Peterson and Oh 1999; Burns *et al.* 2004; Hult *et al.* 2005). These devices are inexpensive, considerably smaller and easier to operate, thus overcoming the shortcomings of their predecessors.

1.3 Novelties of this work

This thesis deals with improvement of existing and development of new diagnostic tools to measure flame parameters, most notably temperature. In this work, we make use of novel diode lasers to achieve accurate thermometry that had previously only been achieved through use of large and bulky traditional laser systems (*e.g.* Nd:YAG or Ar^+-ion pumped dye lasers). The use of such diode lasers will enable future research by other groups to be conducted at considerably lower cost and simplicity of operation. Further to the development of diode laser technology, we have also improved the

application of existing diagnostic tools to acquire flame parameters with greater accuracy in real systems. Both the development and improvement of techniques pave the way to being able to acquire high fidelity experimental data for technical combustion. The focus of this work is the accurate measurement of temperature in flames, as it continues to be difficult to achieve. Accurate determination of temperature in flames is important, because it allows for the development of better computational models, and hence improved predictive power of complex combustion behaviour. Notable temperature dependent combustion phenomena that are of interest in the research community are flame instability and soot formation. Both depend crucially on input temperature data, for flame instability is driven by temperature fluctuations and the kinetics of soot formation is non-linearly dependent on flame temperature.

In this work, we performed measurements to investigate flame instability using an acoustically-forced turbulent lean premixed flame stabilised on a burner, whose design was modelled to mimic instability in industrial combustors. Coherent anti-stokes Raman scattering (CARS) of vibrationally excited nitrogen molecules was used to re-examine temperatures that appeared unrealistic in previous two-line OH PLIF measurements (Ayoola *et al.* 2009) of the same flame. The novel application of the well established CARS technique to this flame provides a fairer comparison of the experimental data with modelling results in the literature. Such accurate temperature data makes an important contribution for developing insight into the behaviour of the flame stabilised on the model burner.

We then developed a technique that delivers accurate temperature measurements in sooting flames. As will be seen in later sections, the use of novel diode lasers in conjunction with indium two-line atomic fluorescence (TLAF) allows temperature to be resolved in laminar sooting flames with the best accuracy for the first time (Burns *et al*. 2009 *preprint*). It will become clear that this is a significant improvement upon past attempts using traditional laser systems, which are bulky, expensive and subject to laser mode noise (Dec and Keller 1986). The new technique is set to replace CARS in the future, as it is capable of measuring temperature in low pressure flames and has a large temperature range over which measurements can be performed with sufficient sensitivity.

Using the same diode lasers, another technology was developed in this work to measure temperature in flames at high repetition rates in the kHz range (Chrystie *et al.* 2009). This novel application of blue diode lasers to technical combustion was made possible by the continuous output of the lasers, which can be externally modulated at kHz rates. The use of blue diode lasers in conjunction with indium TLAF is a novel development on the work of Dec and Keller, (1986), with improved accuracy and convenience of implementation at considerably lower expense. Such quasi-continuously resolved temperatures at kHz rates offer an opportunity for more comprehensive validation of computational fluid dynamic (CFD) models and greater insight into turbulent flame dynamics.

Finally as part of the goal of making improvements to existing diagnostic tools, further contributions to the insight of turbulent premixed flame

dynamics were made. This was done by re-examining the relationship between the curvature of flamefronts and the local rate of burning. Flamefronts were demarcated by pixelated contours, whose curvature was measured by an improved technique developed by the author (Chrystie *et al.* 2008). The novel technique allowed the identification of the correlation between the curvature at a point on the flamefront and the associated local rate of burning. It was shown by using our improved method of computing curvature that an identifiable trend exists between all three flames studied, which was not evident in the results of Ayoola et al. (2006). The correlations shown in this work now agree with those observed in similar flames in the literature.

1.4 Specific objectives

The following are the main objectives of the present thesis:

- To improve the accuracy and precision of curvature measurements from pixelated images of flamefronts towards a more complete understanding of the relationship between local rate of burning at the flamefront and flamefront curvature through development of image processing techniques.

- To obtain accurate temperature measurements of a lean turbulent premixed flame stabilised on a model burner by employing CARS thermometry that was difficult to achieve in past attempts using OH PLIF.

- To develop and demonstrate the possibility of high repetition (kHz) rate temporally resolved temperature measurements based on the development of the indium TLAF method using blue diode lasers.

- To demonstrate the possibility of acquiring high fidelity temperature data within challenging low pressure sooting premixed flames by using the diode laser based indium TLAF method.

1.5 Thesis outline

This thesis is structured as follows: in chapter 2 the principles of the experimental methods used in this work are described. We cover the principles of the heat release rate imaging technique, and the background to laser induced fluorescence, that was used in the work relating to flamefront curvature and local burning rate at the flamefront. The thermometry techniques used in this work, including CARS and diode laser based indium TLAF, are also described.

In chapter 3, the results from the improvement of computing curvature in flamefronts are presented, in addition to the consideration of the application of the improved technique to ascertain the relationship between the local burning rate and flamefront curvature.

In chapter 4, improved temperature measurements using CARS were obtained in lean premixed flames stabilised on a model burner. The results show the distribution of temperature for vortically distorted flames that underwent acoustic forcing. These distributions are also compared to previous two-line OH laser induced fluorescence temperature measurements.

In chapter 5, we demonstrate calibration free temperature measurements in low pressure sooting flames using diode laser indium TLAF. In chapter 6, we report on the wavelength locking of extended cavity diode lasers (ECDLs) to continuously temporally resolve temperature in indium seeded flames using TLAF at kHz rates. The dissertation then concludes in chapter 7 with a summary of the results, with regard to the objectives outlined above, and a brief outlook on suggested future work.

In the following sections, aspects of both combustion and laser diagnostics are outlined, in order to place the work into context. The dynamics of combustion relating to the specific studies in this work are presented. It should become apparent why there is a need for accurate and precise laser diagnostics for technical combustion. A brief review of laser diagnostics relating to the work here is also presented. It will become clear what the relative advantages and drawbacks are of the well established laser techniques.

1.6 Dynamics of combustion

In this section, we review the nature of combustion with regards to the work presented in this thesis. The flame type studied in this work is premixed, which is an important flame type to study, owing to the widespread use of its applications. Examples include flame kernels within internal combustion engines, and lean burn technology currently being developed for gas turbine combustors. Premixed combustion is achieved by mixing gaseous oxidant and fuel; for most parts of this study air was used as the oxidant. Here, the

mechanisms of premixed combustion are briefly described, which sets the context for the development of the laser based techniques in this study.

The laminar flame is the simplest case to gain understanding of the fundamentals of premixed combustion. The laminar flame consists of a thin flamefront, where most of the reactions occur. The effect of this is represented graphically by the temperature and concentration profiles across the flamefront, as shown in Fig. 1.1.

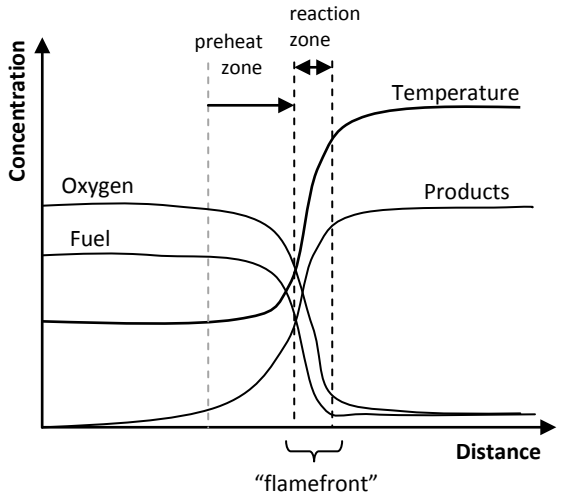

Figure 1.1: Profiles of temperature and concentration of major species across a flamefront for a typical premixed flame.

Here, the reactants, oxygen and fuel are rapidly consumed over a small distance and simultaneously the temperature of the gases rises steeply with a rapid increase in product composition. This narrow region, where rapid changes exist, is known as the "flamefront", which is preceded by the preheat zone (Warnatz *et al.* 1996). The preheat zone is the region on the approach to

the reaction zone, which is relatively cool and where pyrolysis reactions occur. Pyrolysis consists of the endothermic decomposition of the hydrocarbon fuel to smaller intermediates, such as CH_3, CH_2 and CH_3OH (Turns 2000). The intermediates subsequently react exothermically to release the majority of the heat in the flame, as shown by the increase in the gradient of the temperature profile within the reaction zone. The gradients within the flamefront are generally steep, such that the thickness of the flamefront would typically be ~0.5 mm for a hydrocarbon fuel burnt in air at atmospheric pressure (Warnatz *et al.* 1996).

The steep temperature gradients at the flamefront are caused by the strongly exothermic nature of the reactions. Once the molecules overcome their activation energies, a large amount of heat is released, which induces sudden changes in temperature. This is reflected in the narrow reaction zone where there is a soar in temperature, as seen in Fig. 1.1. This fact, in combination with the exponential dependence of the reaction rate (see Eqn. 1.1), causes the behaviour of the flame to be sensitively dependent on the distributions of temperature.

$$r \propto A_{ex} e^{\frac{-E_{act}}{R_o T}} \tag{1.1}$$

Here, r is the reaction rate, A_{ex} is the pre-exponential factor, R_o is the universal gas constant of the unburned mixture, T is the temperature, and E_{act} is the activation energy.

Furthermore, some species of interest in combustion are highly sensitive to temperature, such as NO_X and soot. Steele *et al.* (1995) had shown for lean hydrocarbon flames with a fuel/air equivalence ratio of 0.55 that there is a three-fold increase in NO emission from only 1650 to 1800 K. In the same temperature interval, soot can also increase by approximately the same amount for rich premixed hydrocarbon flames (Haynes and Wager 1981).

The sensitive temperature dependence of combustion is further compounded by the presence of turbulence in real combustion systems. This reinforces the need to procure high fidelity experimental data to help validate models successfully. To illustrate the need for accurate diagnostics, a little background on modelling is informative: The common equations in modelling consist of momentum, energy and mass balances (Warnatz *et al.* 1996). The first of these is referred to as Navier-Stokes, where the fluid motion is modelled. This is a time-dependent equation, which computes the three components of velocity over the entire spatial domain. Navier-Stokes is also density and viscosity dependent, and is hence coupled to the energy equation. The is because the output of the energy equation is temperature, which determines the properties of the gaseous mixture, such as density, viscosity and thermal conductivity. The temperature is also dependent on the rate of reaction, which is contained in the mass balance equations for all the species modelled participating in the chemical reactions. Although it is theoretically possible to model combustion perfectly from the above equations without recourse to assumptions, this would require a tremendous amount of computational power. In order to overcome these limitations, it is customary to simplify the physics and chemistry of combustion. A common approach is

to simplify the set of chemical reactions, which serves to neglect the modelling of some intermediates involved in the reaction pathways (Chakraborty and Cant 2005). This results in a smaller number of mass balance equations to compute. Another simplification applied to the mass balances is the substitution of multi-component diffusion coefficients for bi-component ones. This is an assumption that has to be applied with care, as the neglect of multi-component diffusion can overlook counter diffusion effects for light molecules, such as hydrogen atoms (Kadowaki and Hasegawa 2005). The hydrogen atoms acting as important chemical intermediates in the flame can also undergo diffusion from cooler to hotter regions driven by temperature gradients, owing to the Soret effect (Kadowaki and Hasegawa 2005). Likewise, the Dufour effect is responsible for inducing diffusion of heat by the presence of concentration gradients. Both the Soret and Dufour effects are often omitted in models (Veynante and Vervisch 2002).

Such assumptions in models, as described above, need to be tested to check whether the output of the models crucially depends on them. The testing can be performed by comparison to experimental data. Such data is required to be high fidelity for combustion, both from a spatial- and temporal-resolution perspective. To illustrate this requirement with respect to validating temperatures from a model, experimental data should resolve the Batchelor length- and time-scales. These scales are important, since they are the finest scales over which scalar properties can be measured in turbulent flames. For example, the Batchelor lengthscale is the smallest distance over which a temperature gradient can exist (Batchelor 1959), and hence be measured. The issue of temporal resolution is related indirectly to the lengthscale, in which

higher frequency fluctuations of temperature in the turbulent gases correspond with smaller lengthscales. Within the spectrum of frequencies present in turbulent gases, the highest frequency is known as the Batchelor frequency and is inversely proportional to the Batchelor lengthscale. Typical Batchelor frequencies in turbulent flames are less than ~20 kHz (Wang *et al.* 2005).

It has been explained above the need for highly resolved experimental data, in order to test models and the effects of their assumptions on the authenticity of the computations. This was done for temperature; however other properties of the flame can be measured to contribute further to the validation of models. A comprehensive validation is required, because of the many degrees of freedom involved in the modelling of combustion processes. One example of another set of flame properties that can be measured is the curvature of, and the local rates of burning at, the flamefront (Ayoola *et al.* 2006). In turbulent combustion, vortices wrinkle the flamefront, which causes the flamefront to be contorted in a particular configuration at an instant in time. The adopted curvatures of the flamefront influence the local properties, and hence burning characteristics (Williams 1986). Two ways that flamefront wrinkling can affect the local flame properties are illustrated in Fig. 1.2.

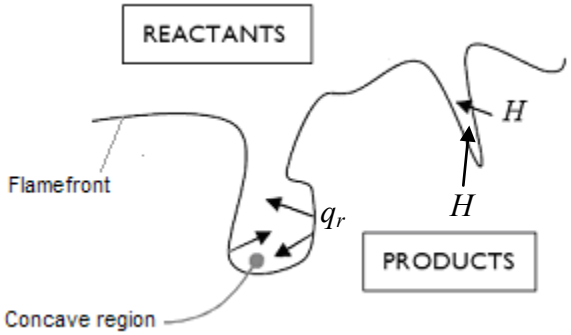

Figure 1.2: Schematic of example flamefront-vortex interactions.

For the left pocket concave to the reactants, a radiative heat, q_r, trap is established. This raises the temperature of the reactants within the pocket, hence would enhance the local rate of burning (Mantel and Samaniego 1999a,b). This effect was shown to be significant, even for non-sooting and lean premixed methane/air flames near the point of extinction (Ju *et al.* 1998). Mass transfer effects also influence the burning rate. For example, the diffusion of the hydrogen radical (H) generated from the flamefront is focussed into concave regions, as shown in Fig. 1.2. This causes an increase in concentration of H at the concave pocket, and hence enhances the local rate of reaction (Najm and Wyckoff 1997). The influence of wrinkling on the flame properties have been shown to determine the local rate of burning, as confirmed by other researchers (Veynante and Vervisch 2002). The results of their models had shown that the magnitude of the flamefront curvature for concave pockets enhances the local rate of burning. It is therefore possible for pockets to exist with large curvatures and correspondingly enhanced localised rates of burning. To ensure that these effects can be captured when using experimental diagnostics, it is important to possess high spatial resolution.

This is necessary, in order to properly resolve the curvature of the flamefront and the local rate of burning. It is also necessary for the diagnostic to be well temporally resolved, in order to capture the instantaneous configuration of the wrinkled flamefront. These two requirements of a diagnostic are necessary, in order to obtain accurate data for model validation.

1.7 Measurement of flamefront curvature and flame speed

Thus far, the requirements of a diagnostic that can spatially and temporally resolve flamefront curvature and local flame speed have been established. One technique that fulfils these criteria is the heat release rate (HRR) method (Najm and Paul 1998). This diagnostic allows the heat release from the exothermic reactions to be spatially resolved in 2-D at an instant in time. A measure of the flame speed can then be computed from the images of HRR. However, in order to obtain images of HRR, laser induced fluorescence (LIF) images of the OH and CH_2O radicals naturally present within a flame have to be captured. The two LIF snapshots of the OH and CH_2O radicals are captured simultaneously, and then the product of the LIF images results in a measure of the HRR. This technique works on the principle of choosing certain electronic transitions in the two radicals, so that the product of the fluorescences correlates with the HRR, and hence rate of burning in the flame (Najm and Paul 1998). As well as being able to measure the HRR using this technique, the curvature of the flamefront can also be captured simultaneously. This is done using the outline of the OH LIF images, which corresponds to the delineation of the flamefront.

1.8 Review of thermometry

Although the measurement of curvature and flame speed is important in validating models, measurement of temperature is also important in a similar vein. This section reviews standard thermometry ranging from sturdy traditional methods to the more complex, high fidelity laser techniques. This section highlights the advantages of the latter methods with regard to the need for accurate and precise data in the study of combustion. It will become apparent that laser diagnostics offer these requirements for the most part, yet improvements still need to be made to obtain better quality experimental data. In this work, we develop for example a new laser technique that offers high repetition rate measurements at little expense (Chrystie *et al*. 2009), whereupon the method and results are showcased in later chapters.

1.8.1 Thermocouples

This traditional method is commonly used in applications not requiring high accuracy, for example online monitoring and control of thermal devices such as domestic gas appliances. Nevertheless before more sophisticated techniques were available, thermocouples were employed to measure temperature in flames. The problem with thermocouples is due to their invasiveness, consisting of a metallic probe that perturbs the flow patterns of flames (Eisner and Rosner 1985). This is caused by the finite size of the probe, limiting the technique's spatial resolution. Transient combustion is also difficult to measure, owing to limited temporal resolution of thermocouples caused by the finite thermal inertia of the probe. Sooting flames can be a

challenge to obtain accurate temperatures, as radiative heat transfer must carefully be accounted. Furthermore, care should be taken that catalytic effects (Hayhurst and Kittelson 1977) do not occur when measurements are taken in chemically reacting systems such as flames.

1.8.2 Optical techniques

The alternative thermometry techniques are based on optical principles, which are non-intrusive, and such techniques can offer high spatial and temporal resolution. Before the use of lasers, optical techniques used either lamps or captured the self-induced fluorescence within the flame. Such traditional methods include line-reversal, pyrometry and chemiluminescence. The main drawback of these is that they are line-of-sight methods, which offer limited spatial resolution leading to spatial averaging in inhomogeneous flames. However, laser based techniques can overcome this problem by exploiting a number of physical processes that occur at the molecular scale, which are outlined in the following sections.

1.8.3 Rayleigh scattering

As one of the earlier techniques, Rayleigh scattering involves directing laser light into the flame and detecting the scattered light. Figure 1.3 represents the process at the molecular energy level, whereby any molecule or atom in the measurement volume is excited to a virtual energy level and the resulting signal is identical in wavelength to the incident radiation. The signal is proportional to the number density of atoms or molecules in the sample

volume and more importantly the Rayleigh cross-section (Eckbreth 1996). The latter parameter is composition dependent, therefore knowledge of the composition is usually required to determine the temperature. This can be evaded by performing thermometry in flames, which possess similar cross-sections throughout space, thus eliminating the composition dependence of temperature, as performed by Wang *et al*. (2005). Nevertheless, simultaneous Rayleigh-Raman measurements can be performed to determine the cross-section at a certain flame position by retrieving the composition from the Raman technique. This is an iterative method, since the Raman technique is both temperature and composition dependent. The drawback of Rayleigh occurs when particles are present in the combustion gases, leading to unwanted Mie scattering that interferes with the Rayleigh signal and hence rendering the measurements useless.

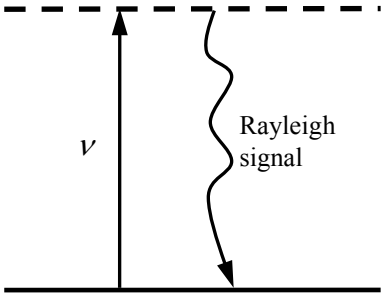

Figure 1.3: Energy level diagram for the Rayleigh process. Dashed and solid lines represent the virtual and real energy levels respectively.

1.8.4 Raman scattering

An alternative is the Raman technique, which eliminates the problem of Mie scattering, because Raman is an inelastic process, and hence detection is performed at a different wavelength to the incident radiation (Banwell and McCash 1994). This is demonstrated by the energy level diagram in Fig. 1.4, whereby a molecule is excited to a virtual energy level and the resulting signal is either Stokes or anti-Stokes frequency shifted by an amount $\Delta E/h$.

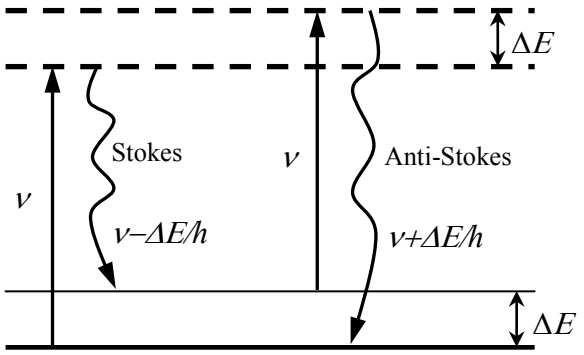

Figure 1.4: Energy level diagram for the Raman process. Dashed and solid lines represent the virtual and real energy levels respectively.

By using a laser with one wavelength many ro-vibrational transitions can be probed; Fig. 1.4 shows an example of a pair of shifted transitions. The resulting collection of wavelengths can be detected using a spectrometer, allowing composition and temperature data to be simultaneously obtained from the Raman spectra. The limitation of the technique is the generation of weak signals, which are of the order of 10^{14} times less intense than the

incident radiation (Eckbreth 1996). This therefore requires the use of very powerful lasers that are expensive and involves complex experimental setups.

1.8.5 Coherent anti-stokes Raman scattering

To overcome the problem of weak Raman signals, Coherent anti-Stokes Raman Scattering (CARS) can be used. The benefit originates from the coherent beam-like nature of the signal, which can be collected through a narrow slit on a spectrometer, significantly reducing the quantity of background interference (Eckbreth 1996). A simplified representation of the process is shown in Fig. 1.5.

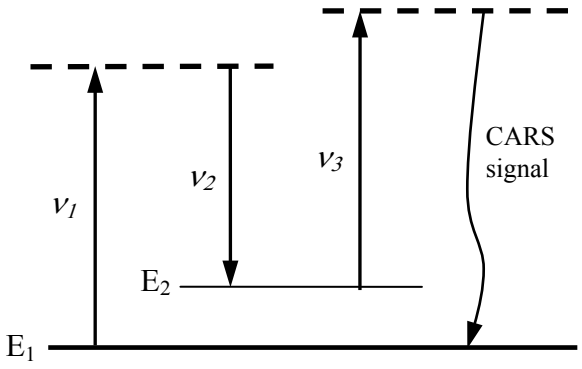

Figure 1.5: Energy level diagram for the CARS process. Dashed and solid lines represent the virtual and real energy levels respectively.

The signal is generated by the careful overlap of three laser beams of usually two different colours ν_1 and ν_2, pump and Stokes laser wavelengths respectively, by focussing at the measurement volume. Here, these beams interact such that the probed molecule is excited by the pump and Stokes

beam to energy level E_2 *via.* a virtual energy level. Whilst in the temporarily excited state, another photon from the pump beams inelastically scatters-off from level E_2 to generate the coherent CARS signal with frequency, $\nu_{CARS} = 2\nu_1 - \nu_2$. More detail is provided on this complex technique in Eckbreth, (1996). Although CARS is a promising method and is very capable of delivering highly accurate temperatures, it is far from straightforward to implement. Powerful lasers are needed along with many optics, rendering the technique expensive. Very careful alignment is required to ensure the laser beams overlap, and hence guaranteeing the generation of the CARS signal.

1.8.6 Two- line laser induced fluorescence

Laser induced fluorescence is the alternative class of diagnostic, which involves the excitation of atoms or molecules to real energy levels resulting in spontaneous fluorescence. One variant is two-line atomic fluorescence (TLAF). This opens up the exciting possibility of exploiting TLAF for making accurate and precise temperature measurements in flames (Zizak *et al.* 1984). TLAF involves the sequential excitation of an atom using two lasers of different wavelengths, as shown by the energy level diagram for TLAF in Fig. 1.6. Figure 1.6 shows an example TLAF scheme that could be used to measure temperature where detection of the fluorescence is performed at the same wavelength ($F_A = F_B$). Here, the atom is excited by one laser (ν_{20}) then by the other (ν_{21}) to obtain fluorescence that returns the atom to energy level 1 above the ground state 0. In order to obtain appreciable signal intensities, level 1 should be sufficiently close to the ground state, where there is a significant population of atoms residing in that energy state. Various probe

species could be used for TLAF thermometry, however an appropriate choice should be made based on the application. In this work, a Group III metal such as indium was used because the separation in levels 0 and 1 causes their relative population to be a sensitive function over the range of temperatures within the flames of interest in this study (Omenetto *et al.* 1972).

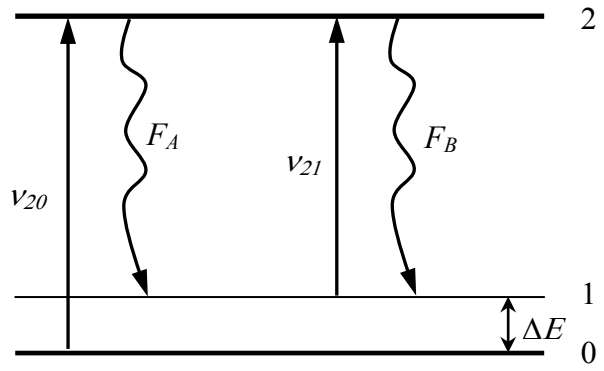

Figure 1.6: Energy level diagram for the resonant TLAF process.

The temperature is computed from the ratio of F_A and F_B, using the Boltzmann equation to relate temperature to population. The major advantage of the TLAF scheme here is its independence of the collisional quenching rate, which originates in the common upper state leading to its cancellation in the quotient of F_A and F_B (Daily 1997). Hitherto, most studies using TLAF have involved the use of Argon-ion pumped continuous wave dye lasers (Elder *et al.* 1984; Dec and Keller 1986). Here, we develop a more compact and less expensive alternative using blue diode lasers (Chrystie *et al.* 2009; Burns *et al.* 2009 *preprint*), which are more robust and easier to use, whilst also possessing better spectral purity leading to improved temperature precision.

Chapter 2

Experimental Methodology

In this chapter, the general principles of the experimental techniques used in this work are described. Specific details are covered in subsequent chapters. This chapter is organised as follows: firstly, a technique for the measurement of temperature in flames is described, which is based on Two-Line Atomic Fluorescence (TLAF). The TLAF technique is presented in detail in chapters 5 and 6, where applications are described on laminar premixed flames. Here, the general principles of TLAF are considered as well as the spectroscopy of atomic indium, which served as a thermometric marker. Then, a technique for the measurement of spatially resolved heat release rates in hydrocarbon flames is described. This diagnostic allows the simultaneous resolution of flamefront curvature and local heat release rate. Finally, CARS thermometry is described and is the subject of chapter 4, which presents spatially resolved temperature measurements from a turbulent premixed flame.

2.1 Indium TLAF Thermometry

2.1.1 Energy Levels in Atomic Indium

A major section of the work in this thesis is based on the Laser Induced Fluorescence (LIF) method. One such technique here is indium TLAF for the purpose of measuring temperature in flames. This involves the seeding of indium atoms into flames and their excitation using diode lasers. The resulting fluorescence was used to infer flame temperature. Indium was chosen as a temperature marker in flames, owing to the sensitive dependence of the fluorescence signals to temperature (Omenetto *et al.* 1972). This is attributable to the close spacing of two low energy electronic levels within indium, as represented by the states: $5^2P_{1/2}$ and $5^2P_{3/2}$ in Fig. 2.1.

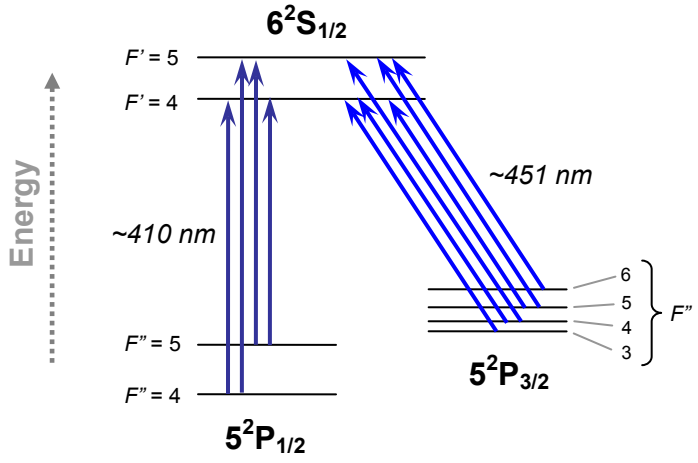

Figure 2.1: The three electronic energy levels of the indium atom including hyperfine structure.

Figure 2.1 also shows a third energy level, $6^2S_{1/2}$; this serves as the common upper state in indium TLAF. As indicated in Fig. 2.1, the indium atom can be excited from either of the lower energy levels to the upper state by irradiation either near 410 or near 451 nm. Figure 2.1 shows further structure in the energy levels, called hyperfine structure, which is explained below. As shall be seen, it will be important to account for this structure, in order to model TLAF spectra accurately. The computation of model spectra is necessary, so that they can be fitted to experimental spectra, with temperature as a fit parameter. The best fit allows the temperature to be inferred.

The following outlines the electronic structure of indium; for a more detailed treatment, the reader is referred to Eckbreth, (1996) and Axner *et al.* (2004). Indium's ground state electronic configuration can be denoted by $4D^{10}5S^25P^1$, where S, P, and D represent the electronic angular momentum quantum numbers, L, of 0, 1 and 2 respectively, and the prefixed numbers denote the electronic shell. The ground state is split into two sub-levels, shown as $5^2P_{1/2}$ and $5^2P_{3/2}$ in Fig. 2.1. The splitting is caused by spin-orbit coupling, which results from coupling of the total orbital angular momentum of the electrons, L, with the total spin, S. The coupling is characterised by the total angular momentum quantum number J, which can adopt multiple values between the limits $(L+S)$ and $|L-S|$, between which J increases in steps of unity. For the indium ground state, one thus obtains $J = 1/2, 3/2$, and the split levels are denoted by the term symbols: $5^2P_{1/2}$ and $5^2P_{3/2}$. In contrast, the excited state shown in Fig. 2.1 is not split because $J = 1/2$ only, and the term symbol is thus $6^2S_{1/2}$.

Further to spin-orbit splitting, each energy level is further split into sublevels with very small differences in energy between them, which are in the order of GHz (Deverall *et al.* 1953). The effect is termed 'hyperfine-splitting', which is caused by the coupling of the angular momentum of the nucleus, *I,* to the total angular momentum of the electrons, *J*. The nuclear angular momentum of all isotopes of indium adopts a value of $I = 9/2$ (Mills *et al.* 1988), and this couples to *J* to yield another quantum number termed *F*, referred to as the total angular momentum of the whole atom. Similar to *J*, the *F* quantum number can increase by unity between $|J-I|$ and $(J+I)$. For the $5^2P_{1/2}$ and $6^2S_{1/2}$ states of indium, $F = 4, 5$ but for the $5^2P_{3/2}$ state, one has $F = 3, 4, 5, 6$.

2.1.2 Hyperfine Energy Structure at 410 and 451 nm

There are selection rules for *F* that dictate which transitions from certain hyperfine splittings in each spin-orbit-split level are allowable, according to $\Delta F = 0, \pm 1$ (Banwell and McCash 1994). The result is that a high-resolution spectrum of the $5^2P_{1/2} \rightarrow 6^2S_{1/2}$ transition near 410 nm consists of four peaks corresponding to the 4"→4', 4"→5', 5"→4' and 5"→5' lines, where the prime denotes the upper level, and double prime the lower levels. These four permitted transitions are shown as hyperfine lines in the spectrum of Fig. 2.2 (b). An excitation scan over the $5^2P_{3/2} \rightarrow 6^2S_{1/2}$ transition, near 451 nm, results in six peaks, corresponding to the 3"→4', 4"→4', 4"→5', 5"→4', 5"→5' and 6"→5' lines, which is shown in Fig. 2.2 (a).

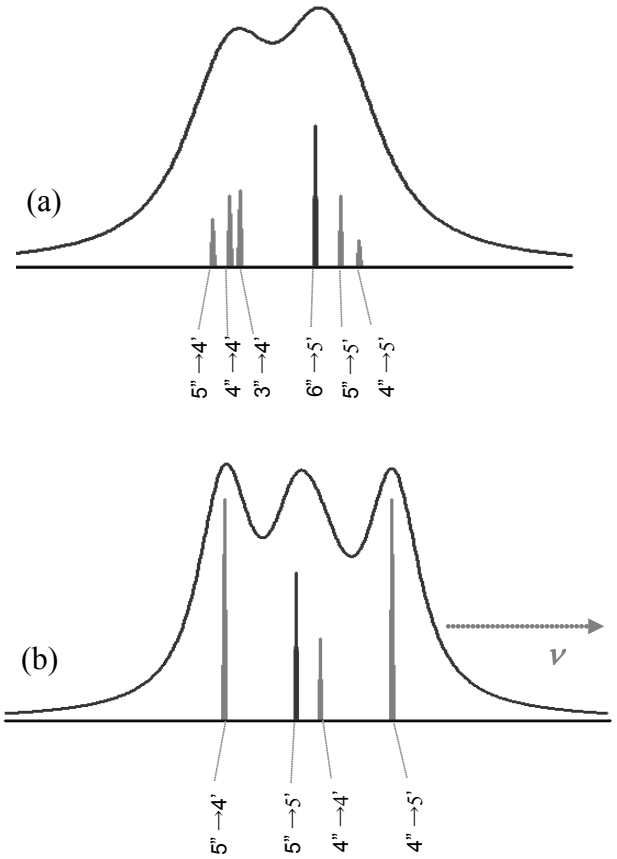

Figure 2.2: Schematic of spectra at atmospheric pressure for (a) 451 nm and (b) 410 nm, including hyperfine lines.

2.1.3 Broadening of Indium Spectra

Despite the representation of the hyperfine lines as spikes in Fig. 2.2, each transition is spectrally broadened through various mechanisms that occur at the molecular scale. The spectra, as shown by the grey curves in Fig. 2.2, are derived from the summation of these broadened lines. The following section describes the contributions to the overall spectral broadening and the relevant background theory, used in the modelling of high resolution indium spectra in

this work. The emitted light from atoms in the gaseous phase is not monochromatic. Spectral broadening results from physical processes that occur during the emission of photons from the excited atoms or during the interaction of atoms with incident photons. These processes affect the spectral signature and are outlined below.

The fundamental broadening mechanism common to all spectroscopic studies is natural broadening (Herzberg 1950). This effect originates from uncertainties in the energy of the states involved in the transition, attributable to the Heisenberg uncertainty principle. Natural broadening is only significant when both pressure and temperature are very low. For indium, the natural linewidths of the transitions, $\Delta\nu_N$, are only 25 MHz. This is a typical value that is far smaller than that of Doppler and pressure broadening in this flame, which are 2200 and 5400 MHz respectively at 2000 K and 1 atm. Doppler and pressure broadening are described below.

A well known broadening mechanism is Doppler broadening. This manifests itself in two forms, namely during absorption of incident photons from the laser source, or during emission when the fluorescence is detected. The former Doppler effect, which is of concern in this work, is based on the principle that the relative velocity of the photons interacting with the indium atoms must always be at the speed of light, *c,* as seen by the atoms. This relativistic phenomenon implies that the indium atoms experience either blue or red shifting of the true wavelength emitted from the laser source. This implies that the ability of indium to be excited is not only dependent on the laser source wavelength but also on the component of the atom's velocity in

the direction of the incoming photon. The velocity distribution of indium atoms in the sample volume is described by a Maxwellian distribution (McQuarrie and Simon 2000). Hence, there will only be a proportion of atoms in resonance with the excitation light. An excitation scan involves the sweeping of the laser wavelength and the fluorescence is recorded as a function of excitation wavelength. The resulting spectrum features Doppler broadened lines (Herzberg 1950) with a corresponding width, $\Delta\nu_D$, given in Eqn. 2.1.

$$\Delta\nu_D = \nu_o\sqrt{\frac{8k_BT\ln 2}{mc^2}} \tag{2.1}$$

Here, ν_o is the centre frequency of the transition, k_B is the Boltzmann constant, m is the atomic mass and T is the temperature.

Another broadening mechanism that is predominant in combustion at atmospheric conditions is pressure broadening. This phenomenon is caused by the perturbation of indium by other species (predominantly nitrogen for air/fuel flames) during fluorescence (Nefedov *et al.* 1999). This leads to temporal phase disruptions, whose frequency distribution is given by its Fourier transform. The breadth of the distribution, $\Delta\nu_L$, is proportional to pressure, assuming ideal gas behaviour. However, the effects of pressure not only lead to spectral broadening, they also lead to spectral shifts in the centre frequency of the transition. The magnitude of the shift is proportional to $\Delta\nu_L$ (Eberz *et al*. 1984). As for the case of Doppler broadening, pressure broadening is also a function of temperature. However, temperature effects on

pressure broadening are not straightforward to predict in theory. Some assumptions in the theory are made (*e.g.* the impact pressure broadening approximation (Nefedov *et al.* 1999; Hult *et al.* 2004)), leading to the Lorentzian width being dependent on temperature raised to the power of -0.7 as seen in Eqn. 2.2.

$$\Delta\nu_L(T,P) = \Delta\nu_L(T_{ref},P_{ref})\left(\frac{P}{P_{ref}}\right)\left(\frac{T}{T_{ref}}\right)^{-0.7} \tag{2.2}$$

Here, $\Delta\nu_L(T_{ref}, P_{ref})$ is the Lorentzian width at reference conditions, and P is pressure.

By considering both Doppler and Lorentzian broadening, an overall spectral lineshape can be modelled from the convolution of the two effects (Eckbreth 1996), resulting in a so-called Voigt profile, as expressed in Eqn. 2.3:

$$g(\nu) = \frac{2}{\Delta\nu_D}\frac{a}{\pi}\sqrt{\frac{\ln 2}{\pi}}\cdot\int_{-\infty}^{\infty}\frac{e^{-y^2}}{a^2+(x-y)^2}dy \tag{2.3}$$

Here a and x are defined as:

$$x = 2\sqrt{\ln 2}\,\frac{(\nu-\nu_o)}{\Delta\nu_D} \tag{2.4}$$

$$a = \sqrt{\ln 2}\,\frac{\Delta\nu_L}{\Delta\nu_D} \tag{2.5}$$

The parameter, a, indicates the relative importance of each broadening contribution. For $a << 1$, the Doppler mechanism dominates (Eckbreth 1996). However, under flame conditions the general Voigt formulation, expressed by Eqn. 2.3, gives the most accurate representation of true lineshapes. The Lorentzian contribution within Voigt profiles is portrayed in Fig. 2.3. Here, the green profile is almost entirely Doppler in nature. For increasing Lorentzian contribution, the overall Voigt profile widens.

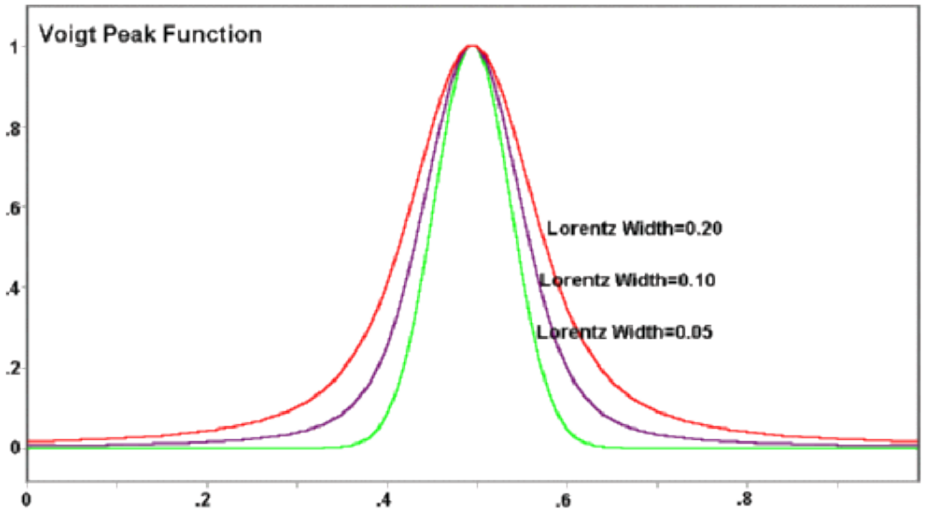

Figure 2.3: The normalised Voigt distribution for varying Lorentzian contributions. The green distribution is predominantly Doppler (Gaussian) in character (adapted from Thermo Fisher Scientific).

2.1.4 Two-Line Atomic Fluorescence Thermometry

The Voigt profile is essential for correctly modelling LIF spectra, since both Lorentzian and Doppler contributions are significant. Model spectra are required, in order to be fitted to experimental ones, so that temperature can be

computed from experimental data. The first step to computing temperature requires the integration of fitted model spectra with respect to wavelength. The integrated result is equivalent to the detected fluorescence power. Because the broadening mechanisms are elastic (Nefedov *et al.* 1999), the fluorescence power can be equated to that in the absence of spectral dispersion, whose relation is given by Eqn. 2.6.

$$F_{2i} = (\varepsilon_2 - \varepsilon_i) A_{2i} N_2 V \left(\frac{\Omega}{4\pi} \right) \tag{2.6}$$

Here, $\varepsilon_2 - \varepsilon_i$ is the energy difference between the upper state 2 and one of the two lower states i. V is the measurement volume of the imaged point, A_{2i} is the transition probability for spontaneous emission, and N_2 is the number density of atoms in the upper state. By focussing the incident laser beams to a point, the amount of LIF can be detected from the focal point with a solid collection angle Ω.

By knowing the integrated fluorescence power is equivalent to F_{2i} for a transition $2 \rightarrow i$ (where i = 1 or 0), we can compute temperature from the experimental spectra. The following analysis illustrates how this is possible by considering the population dynamics of the indium atom and its electronic states in detail. Figure 2.4 represents the detection scheme used in this work, and illustrates the processes that determine the proportion of indium atoms, N, that can be in electronic states 0, 1 or 2.

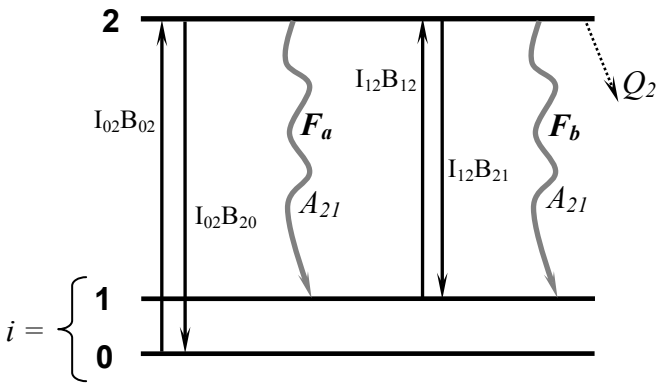

Figure 2.4: The TLAF detection scheme used in this work.

Here, N_i is the number density of atoms residing in state i. A_{2i} is the transition probability for spontaneous emission, F. B_{2i} and B_{i2} are the coefficients for stimulated emission and stimulated absorption respectively, I_{i2} is the laser irradiance at the wavelength corresponding to transition $i \rightarrow 2$, and Q_2 is the total rate of de-excitation from the upper state by collisional quenching and other non-radiative losses. The terms beside the arrows all have units of s^{-1}.

The temperature can be derived by considering the excitation and de-excitation processes. A population balance can be used to calculate the proportion of atoms that are in a particular energy state, as shown in Eqn. 2.7:

$$N_i I_{i2} B_{i2} = N_2 I_{i2} B_{2i} + N_2 A_{20} + N_2 A_{21} + N_2 Q_2 + \frac{dN_2}{dt} \qquad (2.7)$$

Here, we assume that the atoms in state 2 have reached equilibrium, thus rendering the time derivative to zero. In addition to neglecting stimulated emission due to the low population of the upper state, this gives:

$$N_2 = \frac{N_i I_{i2} B_{i2}}{A_{20} + A_{21} + Q_2} \tag{2.8}$$

The two fluorescence signals F_a and F_b, can be expressed as a quotient as in Eqn. 2.9, which one sees as being independent of the quenching coefficient Q_2. This is an important advantage of the TLAF technique over other thermometry methods, since the quenching term is composition dependent and often unknown (Axner *et al.* 2004).

$$\frac{F_a}{F_b} = \frac{N_0 I_{02} B_{02}}{N_1 I_{12} B_{12}} \tag{2.9}$$

$$\frac{A_{2i}}{B_{2i}} = \frac{g_2}{g_i} \cdot \left(\frac{8\pi h}{\lambda_{i2}^3} \right) \tag{2.10}$$

Here, g_i is the degeneracy of energy state i, h is Planck's constant and λ_{i2} is the wavelength associated with transition $i \rightarrow 2$. Equation 2.10 (Demtröder 2004) in conjunction with Eqn. 2.9 yields:

$$\frac{F_a}{F_b} = \frac{g_1 N_0 I_{02} A_{20} \lambda_{20}^3}{g_0 N_1 I_{12} A_{21} \lambda_{21}^3} \tag{2.11}$$

Through use of the Boltzmann equation (Eqn. 2.12), one can estimate the number of atoms in each energy state at temperature, *T*. For conditions of thermal equilibrium, the TLAF equation can then be derived through substitution of Eqn. 2.11 into Eqn. 2.12.

$$T = \frac{(\varepsilon_1 - \varepsilon_0)/k}{\ln\left(\frac{N_0 g_1}{N_1 g_0}\right)} \tag{2.12}$$

The resulting TLAF equation for temperature becomes:

$$T = \frac{(\varepsilon_1 - \varepsilon_0)/k}{\ln\left(\frac{F_a/I_{02}}{F_b/I_{12}}\right) + 3\ln\left(\frac{\lambda_{21}}{\lambda_{20}}\right) + \ln\left(\frac{A_{21}}{A_{20}}\right)} \tag{2.13}$$

2.2 Heat Release Rate Imaging

In this section, we outline the background to the heat release rate imaging technique used to generate the data for the work covered in chapter 3. The heat release rate (HRR) imaging method is another technique that is based on the principle of LIF. HRR imaging reveals a quantity that relates to the reaction rate in flames. It involves the quasi-simultaneous electronic excitation of OH and CH_2O radicals, which are naturally present in hydrocarbon-fuelled flames. The choice of excitation wavelengths is crucial here, in order to obtain high signal strength and desired quenching behaviour. The latter property is desired, so that the product of the OH and CH_2O signals mimics the reaction rate in flames. The following sections outline the principles.

2.2.1 Molecular Perspective of Laser Induced Fluorescence

Thus far, the essence of laser induced fluorescence has already been established in the indium TLAF technique above. Here, the HRR technique is based on LIF of molecules. Knowledge of molecular structure and associated energy levels enables the ideal choice of excitation wavelength. This allows the desired fluorescence spectra to be recorded, whose product mimics the rate of burning in flames. The principles of molecular LIF can be best illustrated by starting from the simple model of a diatomic molecule, for which OH is an important example. We shall thus make the discussion specific to the OH radical. Figure 2.5 (a) shows two masses (atoms) attached

by a spring, which acts as a physical model of the natural vibration of a diatomic molecule.

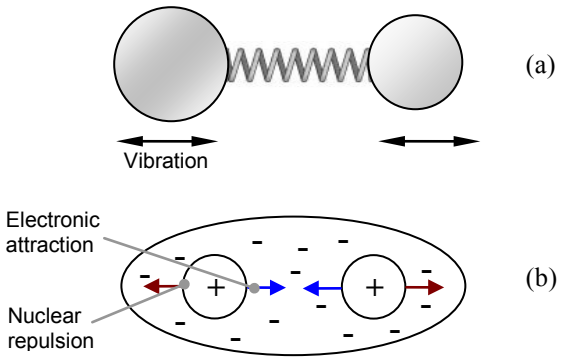

Figure 2.5: (a) Ball and spring model of a diatomic molecule, (b) Simplified representation of two nuclei surrounded by an electron cloud.

Figure 2.6 shows how the potential energy of the diatomic system varies with internuclear distance, x (Banwell and McCash 1994). The corresponding curves are called Morse potentials (Herzberg 1950). When the two masses are close to each other, the spring is compressed and the corresponding potential energy is high. As the masses move apart, the potential energy decreases towards the minimum. The internuclear distance, x_{eq}, at the minimum corresponds to the bond length. This is the distance at which the molecule is most stable. As the masses move further apart, the potential energy increases again, in correspondence with the increase in tension of the spring. This simple model would result in a potential curve with symmetry about $x = x_{eq}$, reflecting a simple harmonic oscillator potential, however the Morse curve reflects a more realistic model of the molecular bond than the simple spring model and this is represented physically in Fig. 2.5 (b). Here, the two nuclei

are surrounded by a cloud of electrons, which bond the nuclei together. The cloud represents a bonding orbital, in which the electrons move in-between the nuclei 95 % of the time (Banwell and McCash 1994), thus pulling the atoms together. However, anti-bonding orbitals also exist, where the electrons are in a higher energy state, and far from being concentrated between the nuclei, are greatest outside them. This promotes nuclear repulsion. However, the overall bonding is a summation of the bonding and anti-bonding orbitals, in which bonding dominates. The overall bonding character is shown by the Morse curves of Fig. 2.6. The asymptotic behaviour of the Morse curve for increasing x is due to the decreasing influence of the electrons in binding the nuclei together (Herzberg 1950), when the two nuclei move further away from each other. Figure 2.6 also shows horizontal lines on the Morse curve, which represent the quantised energy levels due to vibration. The vibrational levels are denoted as v = 0, 1, 2.... Each vibrational level is characterised by an amount of energy, $E_{vib}(v)$, relative to the minimum energy level of a Morse curve, given by Eqn. 2.14 (Banwell and McCash 1994).

$$E_{vib}(v) = h\omega_o\left(v+\frac{1}{2}\right)\left[1-x_e\left(v+\frac{1}{2}\right)\right] \qquad (2.14)$$

Here, the natural frequency of the molecular vibrations is given by $\omega_o = 1/2\pi c.\sqrt{(k/\mu)}$, where k is the bond stiffness and μ is the reduced mass of the two atoms. x_e is the anharmonicity constant that accounts for the asymmetry of the curve. The selection rules for the vibrational transitions follows $\Delta v = \pm 1, \pm 2, \pm 3$ ... (Banwell and McCash 1994) with energy differences of $\Delta E = hc\omega_o(1\text{-}2x_e)$ for $v'' = 0 \rightarrow v' = 1$ and similarly $\Delta E = 2hc\omega_o(1\text{-}3x_e)$ for $v'' = 0$

$\rightarrow v' = 2$. As x_e is small, the transition $v'' = 0 \rightarrow v' = 2$ is approximately double that of the former, however the probability for the transition (*i.e.* the transition strength) decreases. The probability decreases rapidly with increasing Δv, therefore the transition $v'' = 0 \rightarrow v' = 1$ is the strongest and is known as the fundamental transition. $v'' = 0 \rightarrow v' = 2$ as the first overtone *etc*. The differences between these energy levels correspond to excitation wavelengths within the infra-red range.

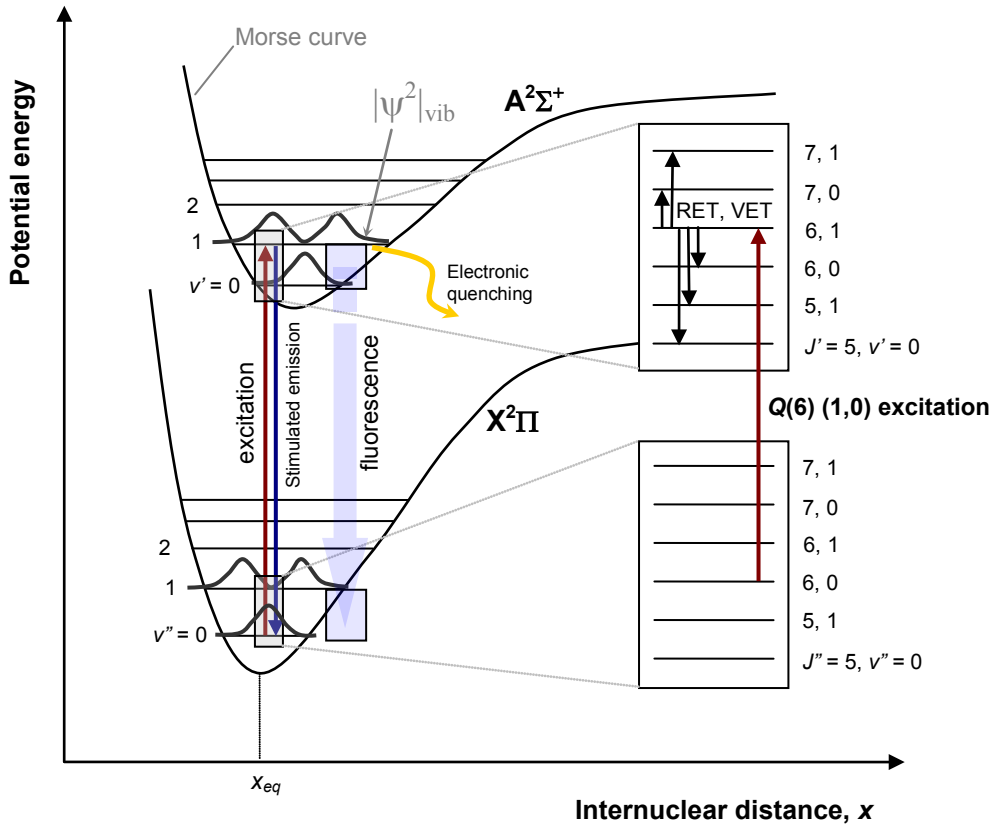

Figure 2.6: Energy structure of a diatomic molecule, using OH as an example.

2.2.2 Electronic Transitions in Diatomic OH

Hitherto, we have discussed the vibrational dynamics of diatomics in general in terms of a Morse curve. However, molecules can be excited to different electronic states, in which the vibrational characteristics are altered. This is represented graphically in Fig. 2.6 for the OH radical used in the HRR method. Two curves are shown: one for the electronic groundstate, $X^2\Pi$, and the neighbouring state $A^2\Sigma^+$. Here, X and A denote the ground and the next-excited electronic levels respectively. The numeric superscript denotes the multiplicity of the electronic state, $2S + 1 = 2$, where the collective spin of the electrons is $S = ½$. Π and Σ refer to the total electronic orbital angular momentum, Λ, about the molecular axis. Different Λ are labelled Σ, Π, Δ, Φ, *etc.* corresponding to values of 0, 1, 2, 3, *etc*. As seen in Fig. 2.6, the main difference between the curves is the amount of potential energy. When a diatomic molecule is excited to another electronic level, there can also be a change in vibrational state; this is termed a vibronic transition. Under electronic excitation, there are no selection rules governing vibrational transitions (Herzberg 1950). However, there are probabilities associated with certain vibronic transitions according to the Frank-Condon principle. Here, the probability of a vibronic transition is high when there is maximum overlap between the vibrational wavefunctions (Herzberg 1950). The magnitude of the wavefunctions, $|\psi_{vib}|^2$, for some of the vibrational states is shown for OH in Fig. 2.6. For $v'' = 0 \rightarrow v' = 1$, there is good overlap between the functions. This leads to a high absorption rate, and hence consequently results in a higher LIF signal. In addition to stimulated absorption, stimulated emission can also take place, as shown in Fig. 2.6. In the example case of OH, a

vibronic transition can be made near 283 nm from $X^2\Pi$ ($v'' = 0$) to $A^2\Sigma^+$ ($v' = 1$). However for the HRR technique to work properly, the wavelength needs to be fine-tuned. This can be achieved by selecting an energy level at a finer spectroscopic resolution. These levels are characterised by the rotation of the molecules, whose angular momentum is quantised into rotational levels. Each vibrational state has a set of rotational levels; this is shown in Fig. 2.6 for the vibrational bands (1,0) in both $X^2\Pi$ and $A^2\Sigma^+$. Each rotational level is given a quantum number J, and possesses energy, E_{rot}, given in Eqn. 2.15 (Herzberg 1950).

$$E_{rot}(J) = h\left(B_v J(J+1) - D_v J^2 (J+1)^2\right) \tag{2.15}$$

Here, B_v is the rotational constant, D_v is the centrifugal distortion constant. The rotational constant is given in Eqn. 2.16 (Herzberg 1950), where r_o denotes the bond length and μ is the reduced mass:

$$B_v = \frac{h}{8\pi^2 \mu r_o^2} \tag{2.16}$$

Similar to the vibrational case, a correction term is needed, which accounts for the molecule being a non-rigid rotator (Herzberg 1950). This is expressed by the centrifugal distortion constant, D_v, in Eqn. 2.15. Unlike for vibronic transitions, the rotational selection rules are strict during an electronic transition. The allowed rotational transitions are: $\Delta J = J' - J'' = -1, 0, +1$, which are termed the P, Q and R branches respectively. For exciting OH as

part of the HRR method, the specific transition $Q(J'' = 6)$ (1,0) was excited, as shown in Fig. 2.6.

2.2.3 Decay Processes of Energy Levels

After excitation, the molecule loses its energy through various processes. The dominant mechanism is collisional quenching, where energy is lost without the release of radiation. This occurs in various forms, such as rotational energy transfer (RET), vibrational energy transfer (VET) and electronic quenching. RET and VET involves the transfer of angular and vibrational motion to neighbouring molecules, as indicated on the energy levels in Fig. 2.6. Electronic quenching involves the transfer of electronic energy to neighbouring molecules. In addition to these processes, the excited molecule can of course also lose energy by emission of fluorescence. The processes are shown in Fig. 2.6, where a multitude of transitions occur within the vibrational band ($v' = 1$, $v'' = 0$). The broad fluorescence spectrum is due to RET and VET, which distribute the molecules into a series of rotational and vibrational levels in the upper electronic state. The corresponding fluorescence spectrum will thus be shaped by these energy transfer processes and the Frank-Condon principle.

2.2.4 Factors Determining the Intensity of LIF

Electronic quenching is the dominant mechanism that reduces the number of molecules that can fluoresce (Kohse-Hoinghaus and Jeffries 2002). The quantity that indicates how much signal can be obtained is the quantum

efficiency, *A/(A+Q),* where the Einstein coefficient, *A,* is 2×10^5 s^{-1} and the quenching coefficient, *Q,* is 5.6×10^8 s^{-1} for OH in hydrocarbon flames at atmospheric pressure (Luque and Crosley 1999; Tsujishita and Hirano 1996). Accordingly, the proportion of molecules available for fluorescence can be reduced to 3.6 %. Furthermore, we have already seen that the Frank-Condon principle determines the probability of molecules that can be excited; by similar arguments it also governs the likelihood of photon emission from the upper to a given lower state. The signal strength is of course strongly dependent on the population of molecules in the lower probed ro-vibrational state prior to excitation. The higher this population, the larger the amount of absorption of the excitation light. At thermal equilibrium, the vibrational and rotational states are distributed according to Boltzmann statistics (Herzberg 1950), as shown in Fig. 2.7 for OH at T = 1500 K. The distributions are given in Eqns. 2.17 and 2.18.

$$\frac{N_v}{N_0} = \exp(-(E_v - E_o)/k_B T) \tag{2.17}$$

$$\frac{N_J}{N_0} = (2J''+1)\exp(-E_J/k_B T) \tag{2.18}$$

Here, N_v and N_J are the proportion of molecules in the pre-excited states for vibration and rotation respectively. The subscript '*0*' denotes the lowest level for either *v* or *J*. *E* denotes the energy level and k_B is the Boltzmann constant.

To obtain maximum LIF, *v"* and *J"* should be chosen, so that maximum signals are obtained, *i.e.* the most populated states should be excited. This is

also true for the excitation of OH of the HRR method where v'' = 0 (at electronic groundstate), as shown in Fig. 2.7 (a). However, J'' = 6 (at v'' = 0 and groundstate) was chosen as a state to excite at T = 1500 K, which does not coincide with the maximum relative population. The reason to excite from this state is particular to the HRR technique and will become clear in section 2.2.6.

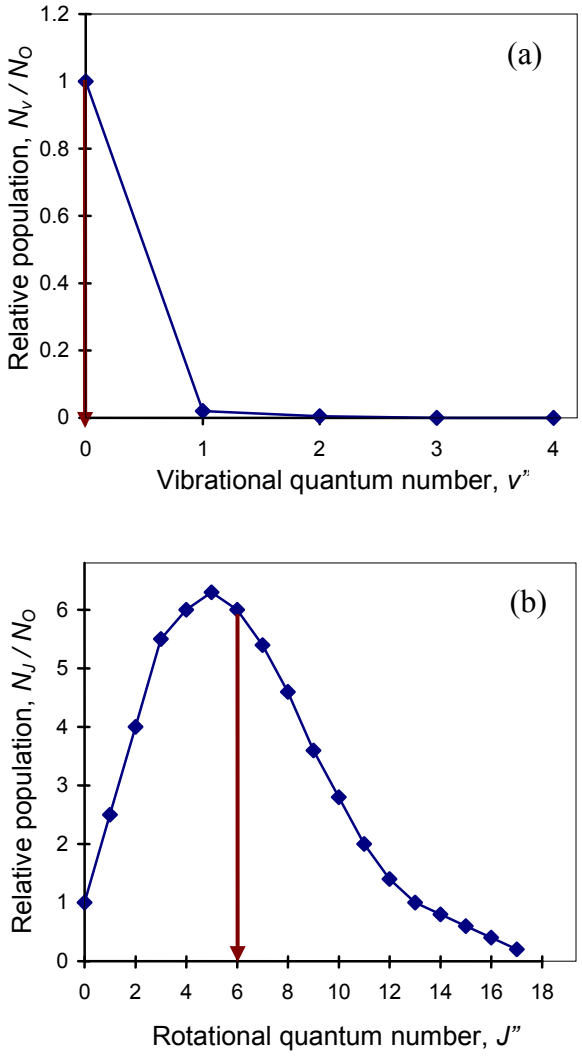

Figure 2.7: Vibrational and rotational population distributions of OH in the ground electronic state at T = 1500 K. Red arrows denote states from which excitation occurs in OH (adapted from Ayoola 2005)

2.2.5 Spectroscopy of CH_2O

In the HRR method, naturally occurring CH_2O in the flame is excited in addition to the OH molecule. The discussion thus far has focussed on the example molecule of OH. The spectroscopic treatment of CH_2O is similar to that of OH above, however there are a few notable differences. CH_2O is a polyatomic molecule and is spectroscopically more complex. It is composed of four atoms, and is non-linear in spatial configuration unlike diatomic molecules. This increases the degrees of freedom in which the molecule can vibrate. There are a total of six vibrational configurations (*i.e.* number of configurations $3N$-6 = 6 where N = 4 atoms) (Banwell and McCash 1994). These are numbered from v_1 to v_6, as illustrated in Fig. 2.8.

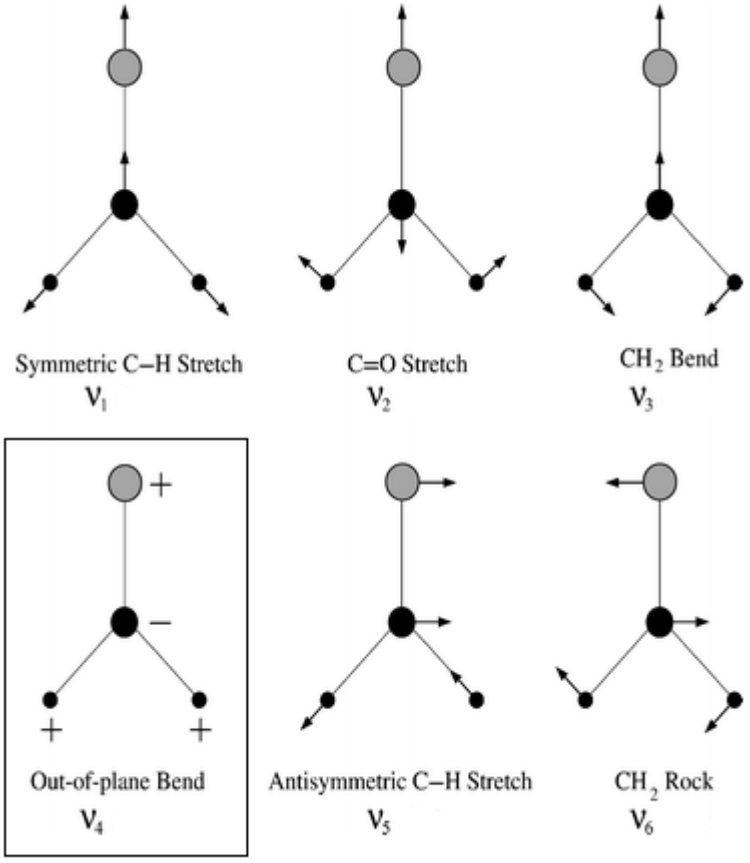

Figure 2.8: The vibrational modes of CH_2O. The highlighted mode, v_4, was excited in the HRR technique (adapted from the RSC).

Owing to the non-linear polyatomic configuration, there exist only four non-degenerate electronic states, denoted as: A_1, A_2, B_1, B_2 (Band 1956). This is in stark contrast to diatomic molecules such as OH, where there are an infinite number of possible non-degenerate electronic states. The electronic transition from the ground state A_1 to the first excited state A_2 is denoted as: $\tilde{X}A_1 \rightarrow$

$\tilde{A}A_2 4_0^1$. Here, 4_0^1 denotes the vibrational mode, v_4, from which the molecule is excited. The transition 4_0^1 is represented in Fig. 2.9, where the superscript denotes the upper vibrational level v' = 1 and the subscript denotes the lower level of v" = 0.

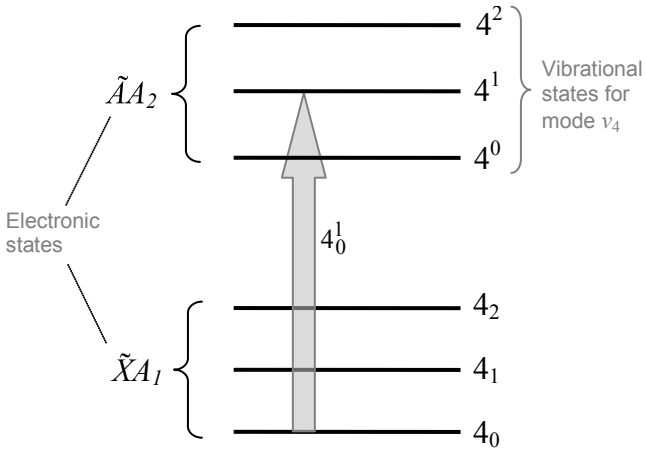

Figure 2.9: Vibrational levels showing the $\tilde{X}A_1 \rightarrow \tilde{A}A_2 4_0^1$ transition in CH_2O.

The transition $\tilde{X}A_1 \rightarrow \tilde{A}A_2$ used in the HRR technique was chosen because of the well-defined vibrational bands and rotational structures in the range of 260 to 360 nm (Ayoola 2005). This allows the temperature dependence of quenching to be modelled more easily, as quenching cross-section data are not available in the literature. This is necessary, in order to achieve a product of the OH and CH_2O signals that mimics the reaction rate in hydrocarbon flames. Such modelling resulted in the choice of the specific transition $\tilde{X}A_1 \rightarrow$

$\tilde{A}A_2\,4_0^1$ near 353 nm. The mode v_4 at 4_0^1 was chosen, because it is the only mode which allows electronic excitation. This is because all the other modes are electric-dipole forbidden (Brand 1956).

2.2.6 Principles of the HRR Technique

The need to excite the OH (and CH_2O) molecule at a specific wavelength has been established. The transitions can be excited by irradiating the flame with a laser beam at 283 and 353 nm for OH and CH_2O LIF respectively. High spatial resolution of the technique in 2-D is also required, in order to measure HRR at various points in the flame simultaneously. This is useful, so that locally resolved measures of flame speed can be estimated, which is elaborated in chapter 3. The spatially resolved excitation in 2-D is achieved by expanding the laser beam through planar-concave and spherical-convex lenses, as shown in Fig. 2.10.

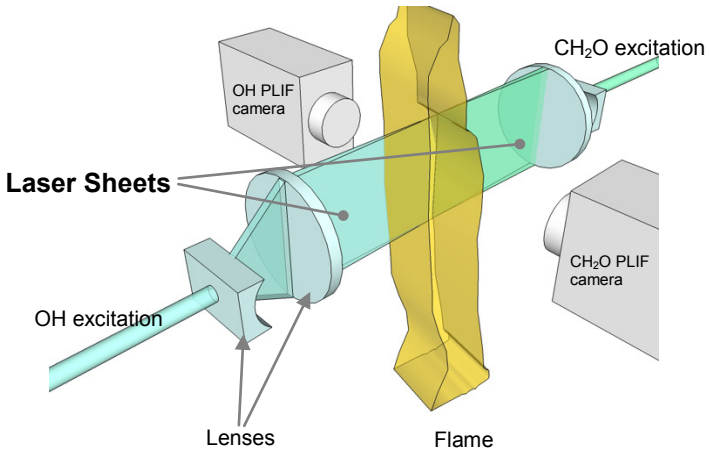

Figure 2.10: The PLIF setup used to excite OH and CH_2O in the flame.

The resulting beam shape is a flat sheet and is focussed in the direction of propagation. OH and CH_2O molecules are excited within each laser sheet and the fluorescence is captured on intensified CCD cameras that are located at right angles to the beam propagation directions. This technique is known as Planar Laser Induced Fluorescence (PLIF). PLIF usually requires the use of pulsed lasers with high peak output power. Excitation is performed for both OH and CH_2O with an intermission of the order of 500 ns. These timescales are small in contrast to that of turbulent flames by three orders of magnitude, thus rendering the PLIF measurements quasi-instantaneous in flame timescales (Wang *et al*. 2005). The images of PLIF for both molecules are captured on separate cameras, which are carefully aligned to image the same cross-section within the flame. In order to derive the Heat Release Rate (HRR), the images of PLIF recorded on the two cameras are multiplied together. The experimental details for this method are given in chapter 3.

Thus far, we have discussed the principles of imaging OH and CH_2O. Such knowledge forms the basis for the HRR method. The reasons for taking the product of the PLIF images from the two cameras are elaborated below. The following argument for this is based on the example hydrocarbon methane in Fig. 2.11.

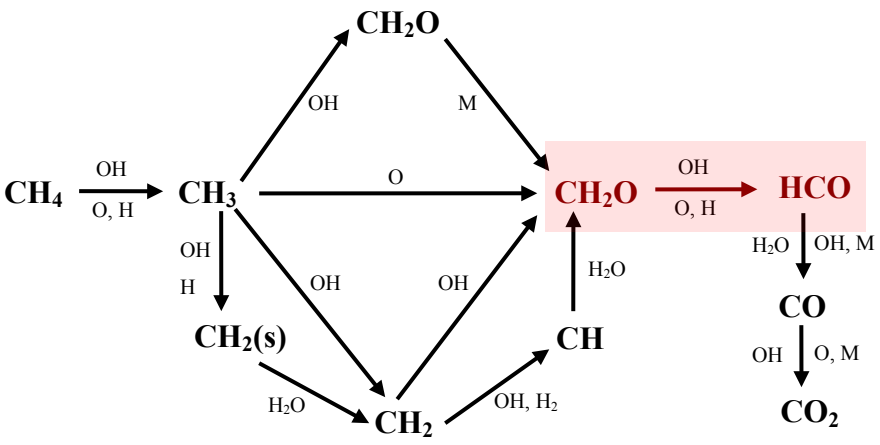

Figure 2.11: Simplified reaction scheme for methane combustion in air (adapted from Turns 2000).

Figure 2.11 shows a simplified reaction scheme for premixed methane/air combustion (Turns 2000). It shows the breakdown of methane to intermediates, before the formation of CO_2. In the development of the HRR method (Najm *et al.* 1998), the intermediate HCO concentration was found to correlate well with the overall HRR, and was therefore identified as a suitable heat release marker. This is because the formation of HCO is in the final set of reactions, as depicted from CH_2O to CO_2, which are all exothermic. The removal rate of HCO is very fast in contrast to its formation rate. Therefore, the concentration of HCO is proportional to the formation rate (Najm *et al.* 1998). Owing to the exothermic reaction leading to HCO, the formation rate of HCO is proportional to the overall HRR. Therefore, the HCO concentration is proportional to the HRR.

So far, the argument has focussed on premixed methane/air flames as an example of the applicability of the HRR method. However, the above is also applicable to similar hydrocarbons up to C_3 and from lean to slightly rich fuel/air mixtures (Najm *et al.* 1998; Fayoux *et al.* 2004). In this work, results from the study of C_2H_4/air flames were used, as described in chapter 3. Although HCO has been shown to be a good HRR marker, the molecule's accessible electronic states are strongly predissociative, leading to low levels of LIF (Lee and Chen 1996). Excited HCO is also strongly quenched. Low concentration levels of HCO due to the fast removal rate of the molecule also contribute to low levels of LIF. These contributions make it difficult to obtain sufficiently high signal-to-noise levels, and therefore an alternative approach was used to measure HRR. The technique was originally developed by Najm *et al.* (1998), and involves the measurement of OH and CH_2O as described above. This approach works, because the formation rate of HCO is proportional to the HRR. The formation rate can therefore be estimated by measuring PLIF of both OH and CH_2O, using such transitions that the product of their PLIF signals correlates with the forward reaction rate in Eqn. 2.19.

$$(OH\ LIF)(CH_2O\ LIF) \propto k(T)[OH][CH_2O] \tag{2.19}$$

Here, *k(T)* is the rate constant and [OH] represents the concentration of OH. The temperature dependence, *f(T),* of the LIF product should be proportional to *k(T)*, in order that the LIF product correlates with the HRR. In the present work, it was verified through simulations that *f(T)* was proportional to *k(T)* over the temperature range of 900 → 1500 K (Ayoola *et al.* 2006). To achieve

proportionality between *k(T)* and *f(T)*, certain transitions were chosen in OH and CH_2O. This is the reason for exciting the *Q*(6) (1,0) $X^2\Pi \rightarrow A^2\Sigma^+$ line near 283 nm, whilst also maximising the amount of LIF, as discussed previously. The same principle applies to CH_2O, in which the $\tilde{X}A_1 \rightarrow \tilde{A}A_2 4_0^1$ line near 353 nm was excited. For more detail of the HRR methodology, refer to Najm *et al.* (1998) and Ayoola *et al.* (2006).

2.3 CARS Thermometry

Another laser diagnostic that was used in this work involved the excitation of vibrational energy levels in molecules. Here, Coherent anti-Stokes Raman Scattering (CARS) was used to measure temperature in premixed hydrocarbon/air flames. CARS was used to excite vibrational modes in nitrogen in the electronic groundstate. Nitrogen was chosen as the probe species due to the large concentrations present within the air for premixed combustion. In what follows, the principles of CARS, and how it is implemented in practice, are explained.

2.3.1 CARS in Terms of Molecular Energy Levels

Vibrational CARS is performed, and here follows a short description of the energy levels in nitrogen. In Fig. 2.12, the energy levels are represented by vibrational levels and their rotational manifolds for v = 0 and 1 at the electronic groundstate $X^1\Sigma^+$ for nitrogen.

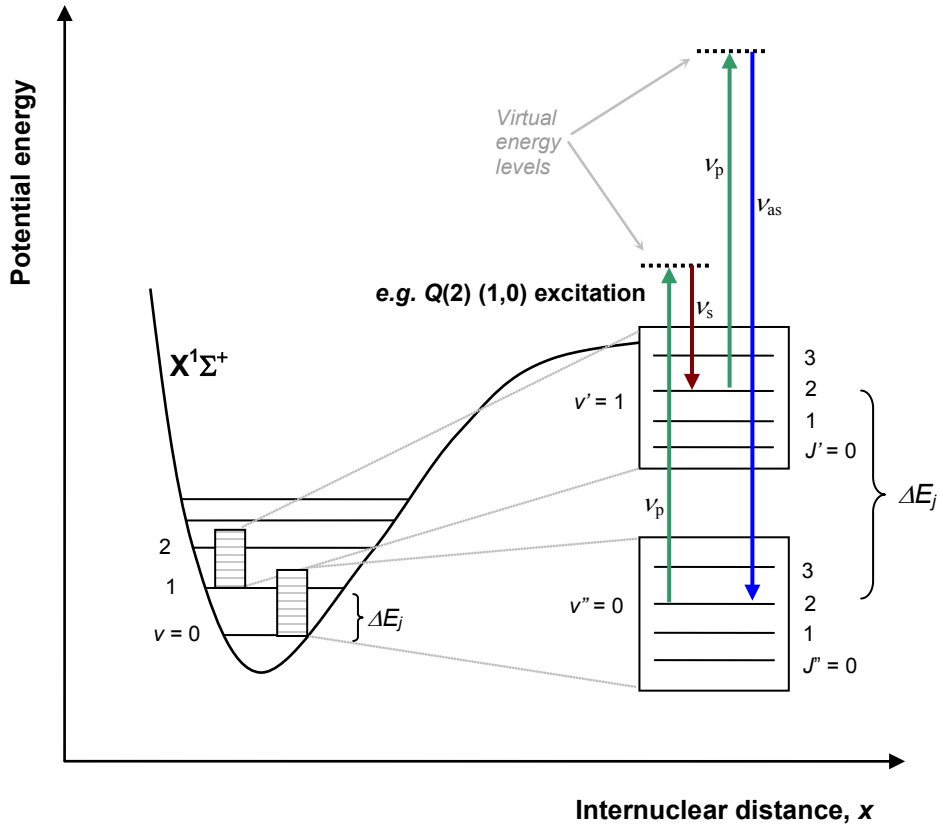

Figure 2.12: Energy diagram for vibrational CARS in nitrogen at ground state. One rotational transition: $J = 2'' \rightarrow 2'$ for $v = 0'' \rightarrow 1'$ is shown as an example. Green arrows denote pumping *via*. ν_p, red arrow corresponding to Stokes at ν_s, and the anti-Stokes signal in blue at ν_{as}.

To demonstrate the CARS process, an example transition is shown in Fig. 2.12. Nitrogen must first be excited with a combination of wavelengths that match the energy differences in the molecule, as shown by the Raman transition, ΔE_j, for $v = 0'' \rightarrow 1'$. This is achieved by employing lasers with radiation frequencies of ν_p and ν_s, to excite the molecule to the next vibrational level *via*. a virtual energy level (Druet and Taran 1981). This is shown by the green and red arrow combination in Fig. 2.12 that results in the

transition: $Q(2)$ (1,0). The CARS signal is then generated by scattering radiation from the excited state with radiation frequency ν_p. This is done again *via.* a second virtual energy level, which yields the CARS signal of frequency $\nu_{as} = 2\nu_p - \nu_s$, as represented by the blue arrow in Fig. 2.12.

2.3.2 Experimental Considerations for CARS

To implement CARS, radiation at 532 nm from a frequency-doubled Nd:YAG laser is commonly used. These lasers are used due to their high power and availability (Kohse-Hoinghaus and Jeffries 2002). To match the resonances, ΔE_j, in nitrogen, a dye laser at 606 nm is used. Two beams at 532 nm and one at 606 nm were aligned and focussed through a convex lens, as shown in Fig. 2.13. CARS is performed by focussing and overlapping the beams to a point where they generate the signal. Focussing furthermore increases the intensity of the signal. The intersection region is the measurement volume, as shown in Fig. 2.13, and determines the spatial resolution. The spatial resolution is affected by the crossing angles of the beams, such that a tighter focus would result in a smaller volume of overlap at the point of intersection. The angles of the beams cannot however be arbitrarily chosen, in order to ensure that the CARS signal can be generated. The alignment must obey closure of the wave vectors (Druet and Taran 1981), as shown in the vector diagram of Fig. 2.13.

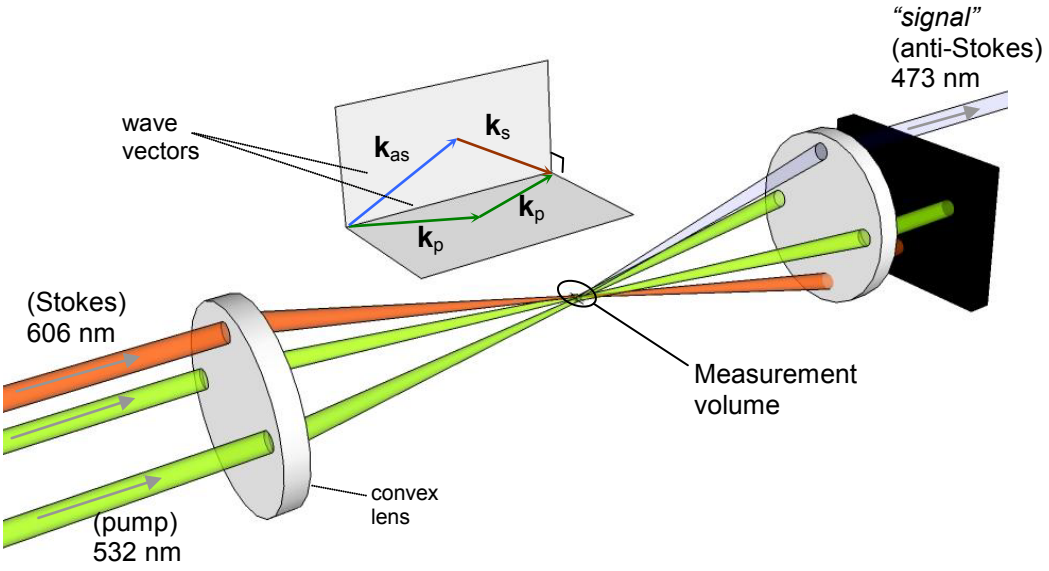

Figure 2.13: Arrangement of beams in relation to the folded BOXCARS scheme represented by the vector diagram. The subscripts of the wave vectors **k** are given: 'as' (anti-Stokes), 's' (Stokes) and 'p' (pump).

This is expressed by Eqn. 2.20. This is the condition where the signal is maximised.

$$\left\| \mathbf{k}_{as} - 2\mathbf{k}_p + \mathbf{k}_s \right\| = 0 \tag{2.20}$$

This is referred to as the phase-matching condition, where the wave vector, $\mathbf{k}_i$, at wavelength λ_i is defined as:

$$\left\| \mathbf{k}_i \right\| = \frac{2\pi}{\lambda_i} \tag{2.21}$$

Together with the knowledge of the excitation and signal wavelengths, the direction of the wave vectors is fully specified with one degree of freedom. If one beam is aligned, then all others are predetermined. As shown in Fig. 2.13, the signal beam is directed upwards, and the residual excitation radiation is blocked. The CARS signal near 473 nm is then directed to a spectrometer.

2.3.3 CARS Spectra

In CARS thermometry, the signal needs to be resolved. The many wavelengths present in the signal are attributable to the use of broadband Stokes excitation near 606 nm. The range of wavelengths of the Stokes laser excites various allowable Raman transitions, ΔE_j, in nitrogen. This allows the narrow-line pump laser at 532 nm to scatter from a range of differently excited nitrogen molecules, thus giving a signal with a range of wavelengths. This is in contrast to the example shown in Fig. 2.12, where a specific transition, $Q(2)$ (1,0), was used as a mere demonstration of the CARS principle. Dispersion of the signal results in a CARS spectrum. Theoretical normalised spectra are shown as examples for a range of temperatures in Fig. 2.14. It is clear that the shape of the spectra is temperature sensitive. Higher temperatures give more pronounced features, for example some of the vibrational bands become apparent. These bands are marked on the spectra as the fundamental, 1st hotband and 2nd hotband; these bands originate from the first, second and third vibrational levels respectively. The fundamental band is most intense, due to the high population of the lowest vibrational level. The latter two bands become prominent at higher temperatures, due to the greater number of molecules adopting higher vibrational states.

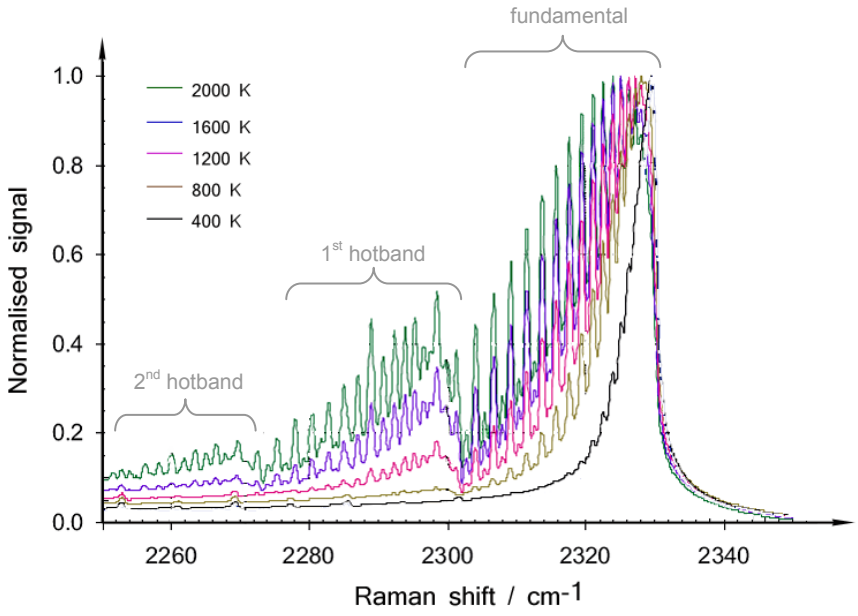

Figure 2.14: Theoretical vibrational N_2 CARS spectra for a range of flame temperatures showing the three vibrational bands.

Figure 2.14 also shows narrow peaks within the vibrational bands, which represent the *Q*-branch transitions for every rotational state. The peaks become prominent at higher temperatures; this is caused by more molecules adopting higher rotational states. One notes for around the *Q*-branch: *Q*(40), the rotational peaks originating from the fundamental band overlap with that of the 1st hotband resulting in spectral interference, due to the close spectral coincidences.

We have seen above that the spectral features are temperature dependent. This allows temperature to be measured from the spectral signature of nitrogen.

The spectral signature is encapsulated within the parameter χ_{CARS}, which denotes the susceptibility for the CARS process. The susceptibility is a function of temperature and the Raman shift, v_j, and is related to the spectrally-resolved CARS signal as shown in Eqn. 2.22 (Druet and Taran 1981). The susceptibility is the key variable that defines the shape of a CARS spectrum.

$$I_{CARS} \propto \left|\chi_{CARS}(T, v_j)\right|^2 \tag{2.22}$$

So far, we have described the use of an excitation source with a range of wavelengths. This technique is termed "broadband CARS", where multiple transitions are excited at once. When this is combined with the use of a pulsed laser, an entire CARS spectrum can be generated rapidly. This allows temperature to be temporarily resolved and is dependent on the pulse duration of the lasers. Pulse times of 10 ns can be routinely accomplished with the use of Nd:YAG lasers. This is far shorter than the timescales involved in turbulent combustion by two orders of magnitude (Veynante and Vervisch 2002). This makes broadband CARS a useful tool for temporarily resolving temperature within turbulent flames, which are inherently fluctuating.

The principles of all the experimental methods used in this work have been outlined. LIF was described and this is used for the HRR and TLAF measurements subject of chapters 3, 5 and 6. CARS was also described, whose implementation is dealt with in chapter 4.

Chapter 3

Investigation of Local Flame Speed Dependence upon Flamefront Curvature

In the previous chapter, the principles of the Heat Release Rate (HRR) technique for generating the data used in this work have been described. In this chapter, the HRR distributions within the investigated turbulent premixed flames are related to local flame speeds. The flame speeds have already been correlated to the curvature of the flamefronts in an experimental study by Ayoola *et al.* (2006), where curvature defines the rate of change of slope of the flamefront. Here, we reanalyse the relationship between flamefront curvature and flame speed, owing to the need to resolve discrepancies within the previously published results. This chapter describes the development of an improved algorithm for the computation of curvature from pixelated contours, which outline flamefronts. The novel method shows correlations between flamefront curvature and local flame speed to be now consistent with results from computational studies in the literature. The chapter is organised as follows: the background behind flamefront curvature and local flame speed is outlined. The particulars of the new method for computing curvature are

detailed. The new method is then validated. Using this method, the data of Ayoola *et al.* (2006) are then reanalysed and presented.

3.1 Background

3.1.1 Motivation

The significance of flamefront curvature arises, because it appears to have a profound effect on the overall reaction rate between fuel and oxygen. On the one hand, curvature leads to strain upon the flamefront (Veynante and Vervisch 2002), which in turn leads to an increased flame surface area and hence a larger global rate of reaction. On the other, curvature also affects the global rate of reaction through influence of the local reaction rate (Najm and Wyckoff 1997; Ju *et al.* 1998; Mantel and Samaniego 1999 a,b). The latter mechanism is not however mediated by the increase in flame surface area. Here, we are interested in investigating the influence of curvature upon the adopted local rate of reaction at the flamefront. This data would serve to confirm correlations between flamefront curvature and local reaction rate to provide further data for validation of computational combustion models (Rutland and Trouvé 1993; Echekki and Chen 1996; Hilbert *et al.* 2004; Chakraborty and Cant 2005). Such studies have shown that there is an increase in the local burning rate for flamefront curvature that is concave to the oncoming reactants, in contrast to flat flamefronts. This has only been shown for flames with a global Lewis number of $Le > 1$. Here, Le is defined as $\alpha/\boldsymbol{D}$, where α is the thermal diffusivity of the fuel/air mixture and $\boldsymbol{D}$ is the binary mass diffusivity of the fuel in nitrogen at inlet conditions (Law 1988,

Rutland and Trouvé 1993); this dimensionless number plays an important role in determining the behaviour of the flame.

A possible reason for the shape of the correlations is the thermodiffusive argument put forth by Williams, (1986). The diffusion of heat at the flamefront from the burnt gases towards the incoming reactants takes place at the same time as the fuel within the reactants diffuses towards the flamefront. When the flamefront is curved this causes the diffusive flux of heat to focus (defocus) at the flamefront regions concave (convex) to the reactants, whilst the diffusive flux of fuel defocuses (focuses) at the concave (convex) regions. For the case of the concave region, the focusing of heat causes a local increase in the temperature of the unburned fuel mixture close to the flamefront. This raises the local rate of reaction at the concave region. However, the defocusing of the fuel diffusion towards the flamefront in concave regions reduces the concentration of fuel close to the flamefront. It is postulated that the two effects compete, and hence the balance between them determines the relationship between local reaction rate and flamefront curvature. Moreover, the balance of these two effects can be skewed by the global Lewis number, *Le.* When the thermal diffusivity is greater than the mass diffusivity (*i.e.* $Le > 1$) the effect of the focusing (or defocusing) of heat is greater than that of fuel diffusion effects, and thus it would be seen that concave regions of the flamefront would exhibit a higher reaction rate than its convex neighbours.

3.1.2 A Previous Investigation

3.1.2.1 Evaluation of Heat Release Rates

Hitherto, there has been one experimental investigation of the relationship between local reaction rate and flamefront curvature for lean premixed turbulent flames (Ayoola *et al*. 2006). Here, their method measures the local reaction rate indirectly. The local reaction rate is correlated to the local heat release rate, whose spatial distributions were measured in flames. The correlation has already been discussed in chapter two. The type of flame is outlined and the laser diagnostic method used in their work is described below.

The quasi one-dimensional flame studied was established within a counterflow burner, as shown in Fig. 3.1. The fuel/air mixture consisted of ethylene set at an equivalence ratio of 0.55, which yielded a flame with a greater than unity global Lewis number. The diluting effect of air entrainment, at the edge of the flame, upon the reactant mixture was eliminated by using a nitrogen coflow arrangement. The turbulent flame was stabilised between the opposing nozzles by using the same bulk gas flow speeds in both directions. Three flow speeds were used in their study, namely 2.4, 2.9 and 3.4 m/s. The lattermost condition resulted in flames burning close to the extinction limit.

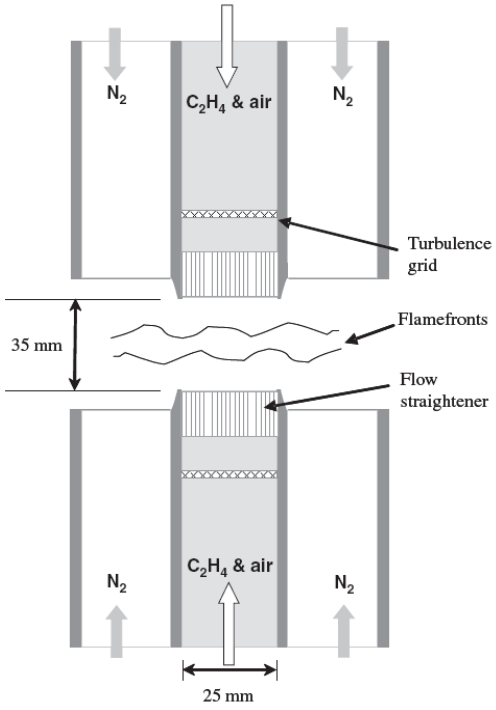

Figure 3.1: Schematic of the counterflow burner cross-section used by Ayoola *et al*. (2006).

Figure 3.2 shows the HRR imaging equipment, which consists of: two Nd:YAG lasers (Continuum Surelite), two dye lasers (Sirah CobraStretch), and two high resolution double exposure Intensified Charge Coupled Device (ICCD) cameras (Lavision Nanostar). The camera for imaging OH LIF was fitted with a UV f/4.5 camera lens (Nikkor) and was equipped with UG 11 and WG 305 filters (Comar). The CH_2O camera was fitted with an f/1.2 camera lens (Nikkor) and GG 375 and SP 550 filters (Comar). For OH LIF, the frequency doubled output from one dye laser was tuned near 283 nm to excite the $Q(6)$ line in the $X^2\Pi \rightarrow A^2\Sigma^+$ (1,0) band. The frequency doubled

output from the second dye laser was tuned to pump the peak of overlapping transitions in the $\tilde{X}A_1 \rightarrow \tilde{A}A_2 4_0^1$ of CH_2O near 353 nm. Further details of the experimental procedure are given by Ayoola *et al.* (2006).

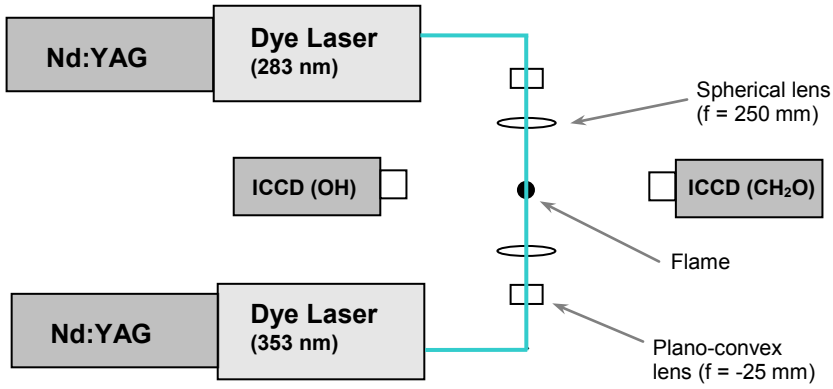

Figure 3.2: Schematic of the laser diagnostic setup for simultaneous PLIF of OH and CH_2O in the HRR technique (adapted from Ayoola *et al*. 2006).

An example image from the HRR method is shown in Fig. 3.3. Here, it is seen that the reactants flow towards each other according to the counterflow configuration. The products flow outward towards the sides. The image shows bands of intense HRR, where the brighter regions correspond to more intense heat release rate.

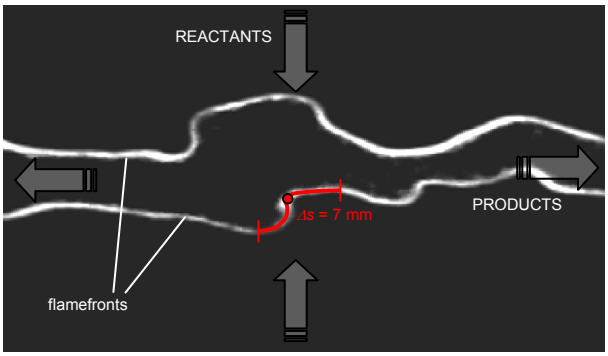

Figure 3.3: Example image of spatially resolved HRR for a flame in the counterflow burner. Brighter regions at the flamefront correspond to higher rates of local heat release rate. The red annotation denotes the lengthscales associated with the original curvature computation method. (adapted from Ayoola *et al*. 2006).

3.1.2.2 Evaluation of Flamefront Curvature

Ayoola *et al.* (2006) computed the curvature, κ, of the flamefront by implementing Eqn. 3.1.

$$\kappa = \frac{\frac{dx}{ds}\frac{d^2y}{ds^2} - \frac{dy}{ds}\frac{d^2x}{ds^2}}{\left[\left(\frac{dx}{ds}\right)^2 + \left(\frac{dy}{ds}\right)^2\right]^{\frac{3}{2}}} \tag{3.1}$$

Here, x and y are the Cartesian coordinates, and s is the curvilinear coordinate along the flamefront. For a derivation of Eqn. 3.1, refer to appendix A.

In the work of Ayoola *et al.*(2006), the curvature was calculated by estimating the gradients of the curve (*i.e. dx/ds* and *dy/ds*) using finite differences over an

arc length, Δs = 7 mm, where s is the curvilinear coordinate along the curve. In contrast to typical length scales of wrinkles, which can be of the order of 3 mm or less, an arc length of 7 mm is too long to enable adequate detection of high curvature small wrinkles. This is shown in Fig. 3.3, where the lengthscale of 7 mm is for a particular segment of flamefront. Here, the 7 mm strand along the flamefront extends far from the strand centre (as represented by the red central dot). Measurement of curvature involves calculation of the second derivatives of x and y in Eqn. 3.1. These were estimated by taking the derivative at both ends of the strand, whose difference was divided by the strand length, Δs. The example in Fig. 3.3 shows that there is almost no change in the first derivative, therefore this would yield zero curvature in this case. This is clearly incorrect, because the curvature to be measured at the central point is actually significantly concave to the reactants. This example thus illustrates that this method of computing curvature leads to significant error.

The curvatures and local heat release rates in the flames they studied were correlated, as shown by the bivariate pdfs in Fig. 3.4. It should be noted that the curvatures are defined as negative for regions of the flamefront that are concave to the reactants and positive for convex.

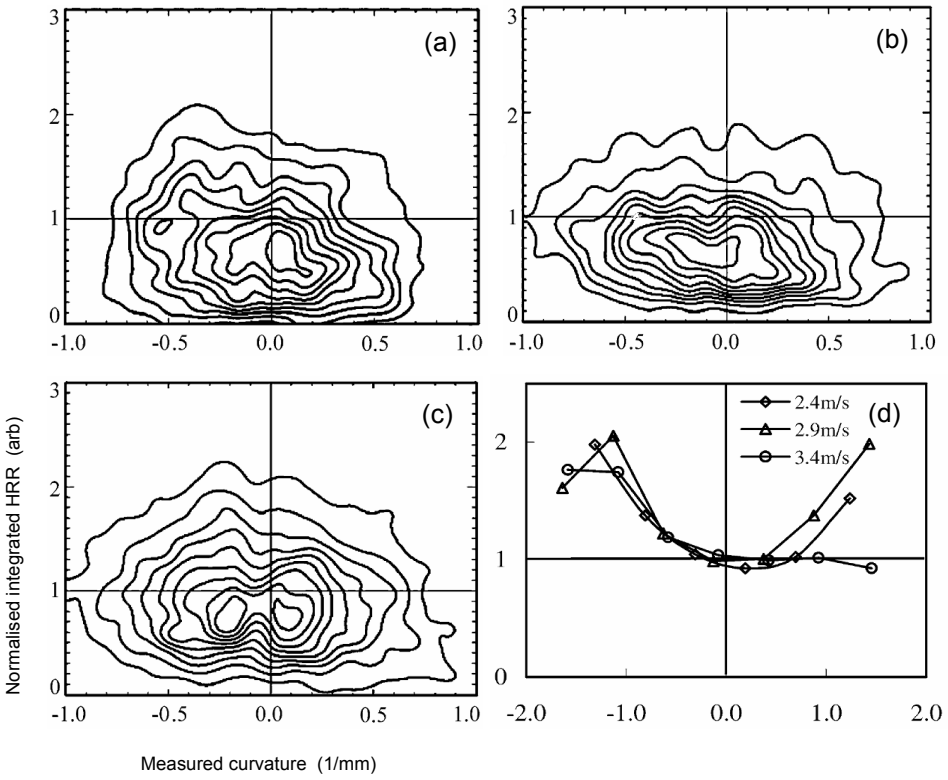

Figure 3.4: Joint pdfs of normalised integrated heat release rate and flamefront curvature for the counterflow flames, with bulk flow speeds of (a) 2.4 m/s, (b) 2.9 m/s and (c) 3.4 m/s. (d) shows the corresponding binned dataset (adapted from Ayoola *et al*. 2006).

The variable on the vertical axes of Fig. 3.4 is the integrated HRR, which is normalised to the value at zero curvature. Integrated HRR was used as a correlate, because it is directly proportional to the local flame speed at the flamefront. The flame speed is a commonly used measure of reaction rate in flames, and is often used in correlations with curvature in the literature (Rutland and Trouvé 1993; Echekki and Chen 1996; Hilbert *et al.* 2004; Chakraborty and Cant 2005). Hence, the use of integrated HRR facilitates

comparisons to other published results. The integrated result is proportional to the flame speed (Warnatz *et al.* 1996), as shown in Eqn. 3.2. This is true because the rate of burning per unit volume, w_{local}, is proportional to the spatially resolved HRR, as discussed in chapter 2.

$$\int_{-\tau/2}^{\tau/2} w_{local}\, dn \;\propto\; S_L \tag{3.2}$$

Here, τ is the flame thickness, and n is the coordinate normal to the flamefront. At each point along the flamefront, the integration of HRR was performed along the local normal. The derivatives (*dx/ds, dy/ds*) calculated for deriving the curvatures were used to guide the direction of integration normal to the flamefront.

Figure 3.4 (a)-(c) are bavariate pdfs that show the correlation of integrated HRR with flamefront curvature. Figure 3.4 (d) shows the binned dataset for all three flames. It is evident from Fig. 3.4 (d) that there is an enhancement of integrated HRR (*i.e.* flame speed) for negative curvatures (*i.e.* concave regions), and this trend agrees with similar flames that have been studied using Direct Numerical Simulation (DNS) (Rutland and Trouvé 1993; Echekki and Chen 1996; Hilbert *et al.* 2004; Chakraborty and Cant 2005). However, Fig. 3.4 (d) also shows clearly that there is almost an equal increase in integrated HRR for positive curvatures in the flames with bulk flow speeds of 2.4 and 2.9 m/s. This is not concurrent with the trends of DNS, which show little increase in burning rate. Furthermore, on inspection, there is an inconsistency in these two trends in relation to that of the corresponding

bavariate pdfs. The pdfs seem to exhibit little increase for positive curvatures, which cannot be accounted for. Finally, erratic behaviour is also seen in the trends of Fig. 3.4 (d) for curvatures less than -1 mm^{-1}. Again, this behaviour is not observed in the results of DNS. In light of these inconsistencies, in addition to the use of an inappropriately long arc length Δs = 7 mm, one cannot trust the results in Fig. 3.4. This is of particular importance, as the study of Ayoola *et al.* (2006) has provided the first experimental dataset on the correlation of flamefront curvature with reaction rate thus far. Therefore, it is important to reanalyse the dataset, in order to seek what the underlying relationship is and compare to DNS results.

3.1.3 Aims

In light of the findings of the above results, the aim of this work is to re-evaluate the flamefront curvature and the associated integrated HRR values in a rigorous manner, in order to check whether the hitherto published results of the correlations between the two variables are valid. This is performed by developing a more systematic method for computing curvature using the method of local polynomial curve fitting, which is explained in the following.

The computational representation of a piecewise continuous curve is inherently discrete and leads to a rounding of the true coordinates of the curve to the nearest pixel in the rectangular grid. The limited spatial resolution has two effects with regards to small natural undulations in the curve, which includes the possibility of the omission of these small undulations and an unpredictable allocation to neighbouring pixels. With these effects in mind,

the unpredictable influence of pixelation can be envisaged as introducing random noise to the representation of the real continuous curve. Unfortunately, any method of evaluating curvature directly from the pixel coordinates would rely on a poor estimation of the spatial second derivatives, which themselves are sensitive to the effects of pixelation noise. As a prescription, the discretised coordinate position's pixelation noise is filtered, in order to obtain an approximate continuous coordinate representation; this is often achieved either by filtering particular spatial frequencies (Gashi 2005) associated with the curve or by applying local curve fitting (Renou 2000).

In this work, polynomial curve fitting was used; this uses two parameters, namely the polynomial degree, and the number of neighbouring pixels on either side of the central pixel under consideration that are used in the curve fitting. The scheme works by locally fitting a polynomial curve of a specified degree, pivoted at the central coordinate with an equal number of curve fitting points on either side. The best fit of the curve to the discretised points is achieved by employing the least-squares method and the output of this fit comprises of polynomial coefficients describing the curve shape, hence resulting in an analytical expression for the locally fitted curve. This can then be differentiated spatially, for the subsequent estimation of curvature at the central pixel. This process of curve fitting is then repeated for every point along the flame contour.

3.2 Experimental Method

A rigorous treatment of the curvature and the local integrated heat release rate is important, in order to correlate the two quantities correctly. Accurate polynomial curve fitting must be applied to the flamefront contour, in order for the measurement of curvature to be representative of the true value. The length and degree of the polynomial segment must be carefully selected. Polynomials of an insufficient length will imprecisely estimate curvature when fitted to the flame contour, because pixelation noise predominates. Conversely, excessively long polynomials result in inaccurate fits that smoothen undulations of the flame contour, and hence consistently underestimate curvature. Tuning of the curve-fitting parameters can be achieved using an analytical test curve, which is then pixelated and fitted with polynomials. The theoretical and the measured curvatures can be obtained, where they are then compared at every point along this test curve. The difference between the theoretical and measured curvatures at every point is then evaluated to compare the errors resulting from different types of polynomial segments. To ensure that the curvature evaluation algorithm will measure curvature of a pixelated flame contour with minimal error over the curvature range of interest, the test curve should possess a similar range of curvatures. Currently, no systematic method of tuning the two parameters for polynomial curve-fitting exists. A simple test case involving circles of various radii has been used, for example by Haq *et al.* (2002). Unfortunately, the circle, which has a fixed theoretical curvature, does not realistically represent the undulating nature of a typically contorted flamefront, which changes both sign and magnitude in curvature.

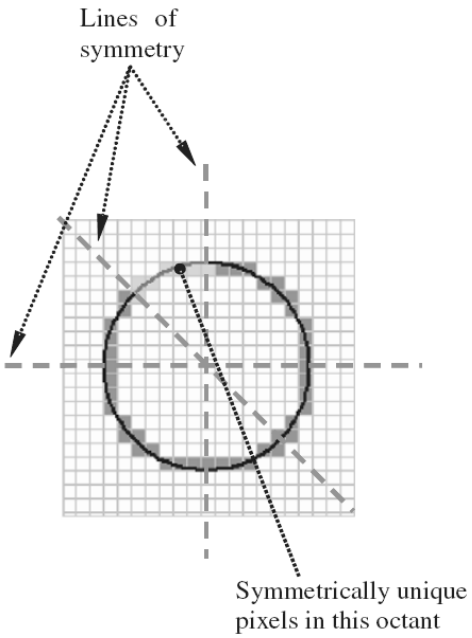

Figure 3.5: Representation of pixelation and lines of symmetry.

A further problem is that the circle has symmetry, where eight octants are pixelated identically, as illustrated in Fig. 3.5. This means that only the pixels of one octant of the circle are 'symmetrically unique' (*i.e.* pixels whose centres are uniquely offset from the underlying theoretical curve, see Fig. 3.5). Each symmetrically unique pixel has a unique value for the curvature measured at its location by use of polynomial fitting, which differs from the theoretical curvature due to the effects of aliasing. In order to compare the effectiveness of different sets of tuning parameters, we must evaluate for each theoretical curvature the sample mean of the absolute offset between the measured and theoretical curvatures over all the symmetrically unique pixels

in the test object (*i.e.* over one octant of the circle). If there are too few symmetrically unique pixels, then the sample mean does not represent a good estimation of the mean that would be found with a much larger number of symmetrically unique pixels. This leads to difficulties when performing polynomial testing at higher curvatures using test circles because small test circles have fewer pixels that are symmetrically unique. The circular test case would hence not necessarily offer an accurate basis upon which to tune the curvature evaluation algorithm for measuring curvature from flame contours.

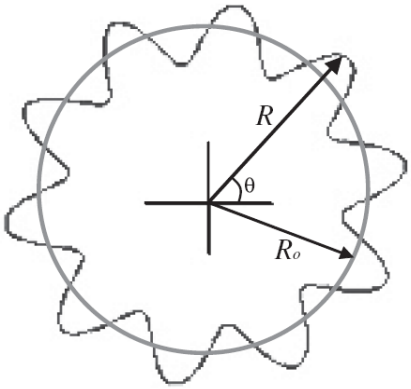

Figure 3.6: An example test rosette for a given set of parameters, where $A = 0.3R_o$ and $B = 10$.

An alternative method for curvature algorithm testing, referred to as the 'rosette test curve' here, was conceived, in order to improve upon circular test curves. This is best expressed in polar coordinates, given by:

$$R = R_o + A\sin(B\theta) \tag{3.3}$$

where: $A \le R_0, \quad B \in Z^+ \quad and \quad 0 \le \theta < 2\pi$

Here, R_o is the mean radius about which R oscillates and A is the amplitude of oscillation, under the constraint that B only adopts positive integers. A plot of an example test rosette is shown in Fig. 3.6. This test curve formulation yields a continuous curve with a cyclically repetitive pattern. The utility of this curve is based upon its periodic elements being repeated in different orientations relative to the rectangular grid of pixels, consequently yielding slightly dissimilar pixelated shapes of the elements. This random distorting effect of pixelation upon the measured curvature for the test curve means that all of the pixels are symmetrically unique; this is paramount for reliably tuning the curve-fitting parameters. The rosette test curve has the advantage of a variation of theoretical curvature along the contour and an alternation of curvature sign, which more realistically represents the undulating nature of a flame contour than the circular test curve. Polynomial testing involves computing the theoretical and measured curvatures at each point on the rosette curve. The absolute value of the difference between the theoretical and measured curvatures is then calculated for each point. The data are then binned in terms of theoretical curvature, and for each bin (of width $\Delta\kappa_i$) the arithmetic mean of the absolute offset between measured and theoretical curvature is determined, denoted by δ_i. The polynomial order and length chosen results from the smallest value of the mean offset, $\overline{\delta}$, over the range of curvatures (κ_{nbins} - κ_1) present in the flame under study, given by the minimisation with respect to the order and length of the polynomial:

$$\min_{order,length}\left\{\bar{\delta}=\frac{1}{\kappa_{n_{bins}}-\kappa_1}\sum_{i=1}^{n_{bins}}\delta_i\cdot\Delta\kappa_i\right\} \tag{3.4}$$

A range of rosette shapes was used as a basis for polynomial testing; this was performed by setting the three parameters A, B and R_o in the rosette formulation, so that the maximum absolute curvature along the rosette was fixed to 1.5 mm^{-1} for all the test curves used here. This value was chosen to roughly match the highest curvatures that were encountered in the flame contours studied. Furthermore, the curvilinear rate of change of curvature ($d\kappa/ds$) was computed. In general, this parameter is also important in characterising the shape of a contour and the ability of curvature to be resolved properly from its constituent pixels. In order to investigate the effect of this shape-defining parameter on the choice of suitable polynomial, a range of maximum absolute values of $d\kappa/ds$, that are present at the extremely contorted points on the test curve, were used in this investigation ranging from 2 to 6 mm^{-2}.

3.3 Results and Discussion

In this section, the results from the tuning of the rosette curve parameters are presented in conjunction with the optimal choice of polynomial type relevant to this study. The effects of sub-optimal polynomial types upon the correlation of flamefront curvature with local flame speed are shown, along with the nature of the correlation for the optimal choice. Likely reasons

behind the discrepancies are discussed and the physical bases for the underlying correlation are explained.

3.3.1 Polynomial Testing Results

Figure 3.7 shows three graphs of the arithmetic mean of the absolute deviation from theoretical curvature against theoretical curvature and demonstrates how these relationships predominantly depend upon polynomial length. Each data point in Fig. 3.7 represents the mean value of absolute deviation within a curvature bin, whose width is 0.25 mm^{-1}.

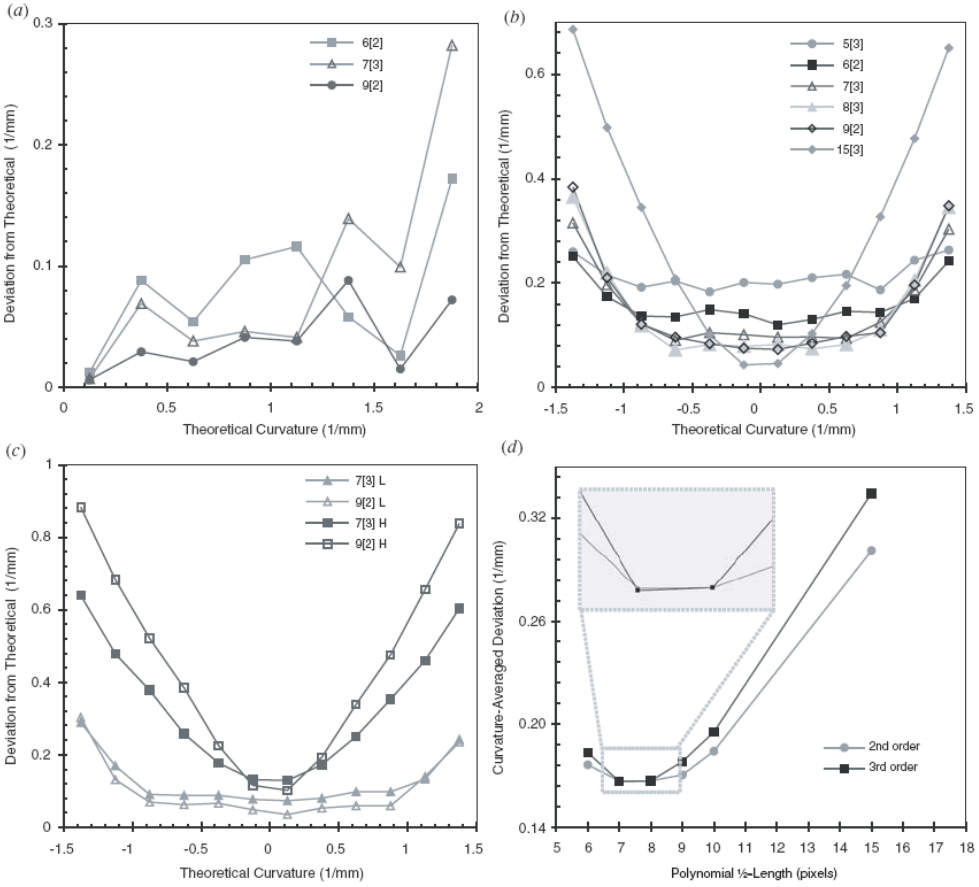

Figure 3.7: Bin-averaged absolute deviations from the theoretical curvature for (a) the circle test and (b)–(c) the rosette test. Note: 7[3] denotes a third-order polynomial of half-length 7 pixels. L and H denote the low and high maximum curvilinear rates of change of curvature of 2 and 6 mm^{-2}, respectively. (d) Curvature-averaged absolute deviations from the theoretical curvature for the rosette test.

Figure 3.7 (a) shows that the curvatures computed by applying a second-order locally fitted polynomial of half-length 9 pixels (denoted as 9[2]) to a series of test circles yields the smallest deviation almost consistently out of all the possible polynomial types that were studied. It should be noted that the three

plots shown are only a small selection of the large number of polynomial types studied; this is to preserve graphical clarity. Application of 6[2] polynomials to the test circles yields a low overall deviation compared to other possible choices, however it is seemingly outperformed by polynomial 9[2]. Figure 3.7 (a) suggests that a common underlying trend between absolute deviation and theoretical curvature exists for all polynomial types, such that deviation increases with higher curvature. This is expected because the fitting of polynomials to smaller circles leads to poorer fits to the circle's pixels; this results in spatial averaging, which causes underestimations of the true curvature. Furthermore, the trends for the three polynomials in Fig. 3.7 (a) become more erratic with increasing curvature. There is a decrease in consistency between the three trends for curvatures greater than about 1 mm^{-1}, which is due to the higher level of uncertainty present in the measured curvatures associated with smaller circles. As discussed above, larger uncertainties exist in the averaged deviations for smaller circles, because fewer values are used in the computation of the average; this is the case as smaller circles have fewer symmetrically unique pixels upon which to form an unbiased average.

Figure 3.7 (b) shows the results from applying five polynomial types to a test rosette that was set with a maximum absolute curvature of 1.5 mm^{-1} and a maximum absolute curvilinear rate of change of curvature of 3 mm^{-2} along its profile, whose values are a realistic range present within the flame contours studied here. Figure 3.7 (b) shows similar underlying trends to that of the results from the circle tests, in that deviation from true curvature increases with higher absolute curvature due to the increase in spatial averaging. There

is a little scatter in the data in the curves of Fig. 3.7 (b) unlike for the circle test results in Fig. 3.7 (a). The smoother plots result from a smaller uncertainty in the average measured curvatures from the test rosette. This is the case because the test rosette used in this example was set with a large radius, R_o, which generated a large number of repeating segments; this results in the segments lying in many different locations relative to the rectangular matrix of pixels. Consequently, each point in Fig. 3.7 (b) represents an average over data obtained from a large number of symmetrically unique pixels.

Upon measuring curvatures on the rosette for a given theoretical curvature, the average deviation (within a bin) between measured and theoretical curvature can be estimated from a significantly larger number of periodically repeated points upon the rosette when R_o is large, in contrast to the small number of repeated points using circle testing with high curvature small circles. A rosette with a larger radius, R_o, results in a larger circumference, which can accommodate many more repetitions of the periodic segments of the rosette; this results in larger statistical confidence within the bin averaged curvatures. A set of similar polynomial types exists that each yields very similar deviations from the theoretical curvature, as shown in Fig. 3.7 (b) for that rosette test curve; these include polynomials 7[3], 8[3] and 9[2]. However, polynomials of appreciably different lengths, such as 5[3] and 15[3] in this case, yield significantly larger overall deviations. For the case of too short a polynomial, large deviations exist across all values of theoretical curvature, as demonstrated in case 5[3] by its flat profile. This is caused by the fitting of polynomials with too few points, thus resulting in a larger scatter

in the measured curvatures, and hence larger absolute deviation. Overly long polynomials do not suffer from pixelation noise, yet exhibit larger deviations at higher curvatures, because the fitting of long polynomials causes spatial filtering that results in high theoretical curvatures being systematically underestimated.

Although it has been seen that there is a group of polynomials with a similar length and degree that each yields very similar levels of small deviation from true curvature in Fig. 3.7 (b), this is not the case in general. This has been tested through the use of rosette test curves of different shapes obtained by varying the maximum rates of change of curvature, $(d\kappa/ds)_{max}$. Figure 3.7 (c) shows the variation of deviation with curvature for the application of two polynomial types to two test rosettes of different maximum values of $d\kappa/ds$ of 2 mm^{-2} and 6 mm^{-2}. These two rosettes both had the same maximum curvature of 1.5 mm^{-1}, but with different shapes of the rosette, as determined by $(d\kappa/ds)_{max}$. It was found that two polynomial types, 7[3] and 9[2], which give reasonably small deviations for a rosette with a maximum $d\kappa/ds$ of 3 mm^{-2} (as for Fig. 3.7 (b)), do not necessarily yield the same results when applied to curves with different shapes. This is demonstrated in Fig. 3.7 (c), where polynomial 7[3] leads to less overall deviation than 9[2] for nearly all curvatures throughout the rosette with a higher maximum rate of change of curvature. Conversely, 9[2] yields slightly less overall deviation than 7[3] for the rosette with lower maximum rate of change of curvature for all curvatures of interest in this study (*i.e.* $-1.5 < \kappa < 1.5$ mm^{-1}). Figure 3.7 (c) suggests that increasing the maximum value of $(d\kappa/ds)_{max}$ increases the minimum deviation that occurs at zero curvature, and there is an accompanying increase in the

sensitivity of deviation to curvature as shown by larger gradients in these plots. It is seen that there is an increase in sensitivity to polynomial choice with an increase in $(d\kappa/ds)_{max}$, as reflected by the larger differences between the profiles for the polynomials 7[3] and 9[2]. In light of these findings, it would thus always be wise to perform preliminary computations to estimate the range of curvatures and of rates of change of curvatures in the contours under study by using an initial guess for a polynomial type and length. This heuristic would then allow the test rosette to be adapted to the appropriate shape, in order to refine the choice of final polynomial length and degree to be used. In this case, the polynomial 7[3] has been chosen for the purpose of calculating curvature within the flame contours, as it has shown to possess the lowest curvature-averaged deviation, as calculated by Eqn. 3.8. This result is shown in the enlargement of Fig. 3.7 (d), which shows that 7[3] is the best choice in this case. This result highlights that the choice of 9[2] from the circle test is not suitable, hence demonstrating the utility of the rosette test curve method.

3.3.2 Application to Flame Data

3.3.2.1 Curvature Distributions

Figure 3.8 shows flamefront curvature histograms for the flame with the lowest fuel mixture flow rate of a bulk speed of 2.4 m s^{-1}. The histograms depict differences between the measured-curvature distributions of the flame arising from the use of three polynomials: 5[3], 7[3] and 15[3]. Polynomial 7[3] is a benchmark, as it was shown to yield accurate measurements of

curvature from the rosette, as shown in Fig. 3.7 (d). The effects of the other polynomials upon the measured-curvature distribution are also shown.

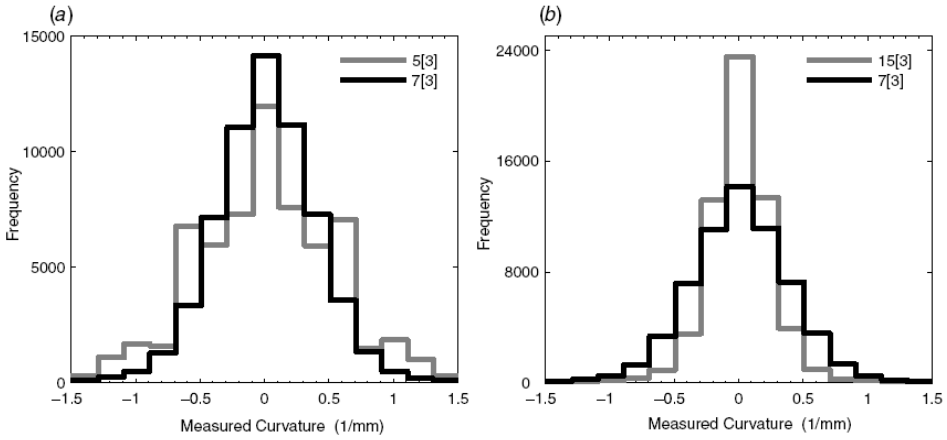

Figure 3.8: Curvature distributions of the flame with a flow rate of 2.4 m s^{-1} for three polynomial types.

The shape of the distributions for all polynomials is symmetrical, and each one is centred at zero curvature; this is consistent with the almost planar time-averaged profiles of the flamefront in the counterflow burner. Yet, appreciable differences exist between distributions using the benchmark and the other polynomials. Use of polynomial 5[3] to compute the curvature distribution, as shown by the grey line histogram in Fig. 3.8 (a), leads to a larger spread of curvatures with a 36% increase in the standard deviation relative to the benchmark. The increased spread is attributable to the effects of pixelation noise. The pixelation noise is also considered to cause the greater amount of noise in the distribution, as shown by the peaks at curvatures of −0.6 and 0.6 mm^{-1}. The use of a larger polynomial, such as 15[3], to measure

flamefront curvature leads to a narrower distribution (35% smaller standard deviation) as represented by the grey line histogram in Fig. 3.8 (b). This is due to the systematic underestimation of curvatures by using a long polynomial. These PDF plots thus demonstrate the importance of selecting a suitable polynomial segment length in the evaluation of flamefront curvature.

3.3.2.2 HRR Correlations

Uncertainties in the estimation of curvature have implications for the accuracy of the correlation of integrated HRR with flamefront curvature – details of how to compute integrated HRR are given in section 3.1.2.2. Figure 3.9 shows four graphs of such a correlation: (a), (b) and (c) show plots for the different polynomial types that were investigated for the curvature evaluation algorithm testing. Graph (d) shows the same correlated variables for the suitable polynomial choice (*e.g.* 7[3]) for the three flames investigated. It should be noted that each data-point in these plots represents the bin-average integrated HRR. Each bin average was determined based on at least 200 individual evaluations of curvature and heat release rate. This avoids the random scatter in the correlation plots that would result from a lack of sufficient data in each bin. The positions along the curvature axis of each point, representing the average HRR within a bin, are based on the centroid of the scattered data within a bin along the curvature axis. It is clear from Fig. 3.9 (a)–(c) that other polynomials such as 8[3] or 9[2] could, for example, have been chosen since they lead to similar correlations. Polynomials 7[3], 8[3] and 9[2] lead to very similar trends with a significant increase in burning rate for negative curvatures.

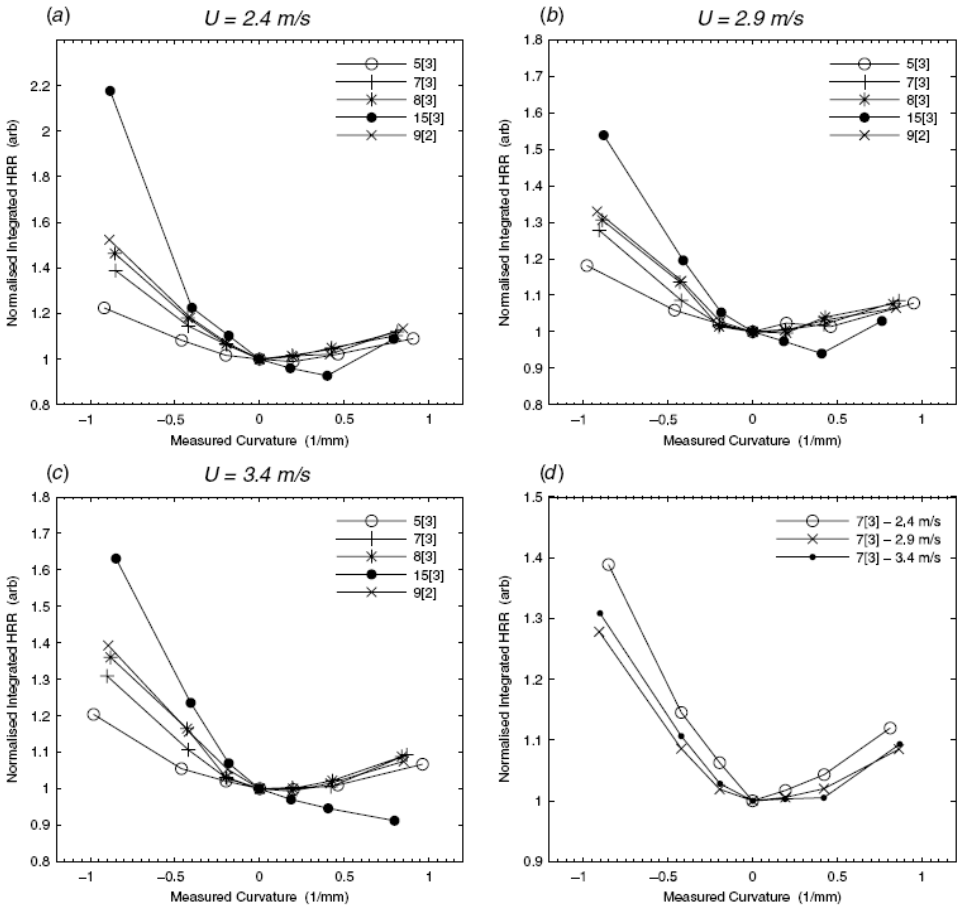

Figure 3.9 Correlations of integrated HRR with flamefront curvature. Plots (a), (b) and (c) show comparisons between five polynomials for the three flames characterised by flow speeds of 2.4, 2.9 and 3.4 m s^{-1}, respectively. Plot (d) shows the correlations for the best choice of polynomial.

It is apparent from Fig. 3.7 (b) that an inadequately long polynomial, such as 5[3], would yield a correlation within Fig. 3.9 with lower gradients. This is due to short polynomials being more sensitive to pixelation noise, and leads to a larger spread in the curvature distribution. Conversely, for longer

polynomials, the HRR correlation is generally steeper due to the tendency to systematically underestimate curvature. It should be noted that for polynomial 15[3], the positive curvature parts of the plots are irregular across Fig. 3.9 (a)–(c) and do not show an artificially steep gradient that would be consistent with the left half of the plots. Specifically, it is seen in Fig. 3.9 (a) and (b) that the correlation for 15[3] reaches a trough, for instance, which is offset from zero curvature. This behaviour could be attributed to an inaccuracy in the integrated HRR values, due to the direction of integration across the flamefront not being perpendicular to the true flamefront orientation. The direction of integration is governed by the estimates made for the gradients, *dx/ds* and *dy/ds*, whose accuracies are determined by the length and degree of the polynomial. As an example, Fig. 3.10 portrays a schematic of the least-square best fit of a long polynomial that is centred at a point of inflection, as denoted by the superimposed pivot point on the HRR image of a flamefront. Cross-sections 1 and 2 are examples of paths of integration across the flamefront, which are always aligned to the local normal of the polynomial. The accompanying dashed lines, which represent the flamefront's orthogonal, portray the potential for disparities between them and the direction of the integration paths. A possible reason for the unpredicted lowering of the right half of the 15[3] plots of Fig. 3.9 (a)–(c) is based on the following argument. If a polynomial that is pivoted at the flamefront's point of inflection is too long, the least square best fit to the neighbouring pixels does not provide an appropriate path for integration across the flamefront, as shown by integration path 1 in Fig. 3.10. This will always lead to overestimation of the true integrated HRR values across the flamefront. However, for regions of the flamefront with a higher magnitude curvature, the path lengths for integration

are perpendicular to the flame contour, as would be found from a polynomial fitted around position 2 in Fig. 3.10. Consequently, this effect raises the integrated HRR values at zero curvature, relative to the higher magnitude curvatures. Once the plot for the overly long polynomial is normalised by this larger integrated HRR value at zero curvature, the curve is shifted downward relative to the correlations based on more appropriate polynomials, thus contributing to the lowering of the right-hand section of the plot.

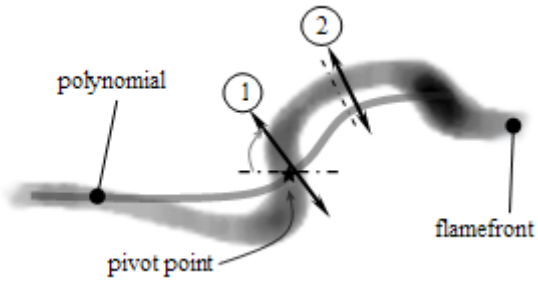

Figure 3.10: Schematic of the fitting of an overly long polynomial to an HRR-based image of a flamefront with the associated HRR-integration paths 1 and 2.

3.3.2.3 Interpretation of Results

Figure 3.9 (d) displays the correlations of local integrated HRR with flamefront curvature for a choice of polynomial 7[3] for all three flames with bulk flow speeds of 2.4, 2.9 and 3.4 m s^{-1}. It is seen that for the three flames there is a significant increase in burning rate, which is proportional to integrated HRR, with increasing magnitude of negative curvature and a less strong increase in burning rate with increasing positive curvature. This trend,

however, is not so clear from previous results (Ayoola *et al*. 2006), as shown by the bivariate correlations of integrated HRR with curvature in Fig. 3.4 (d).

Using the improved method of computing curvature of the flame contours in this work, our results concur with the correlations obtained from numerical simulation by Chakraborty and Cant, (2005) for lean methane/air Le = 1.2 flames. In these theoretical studies, a bivariate PDF was also found to exhibit both a strong increase in the flame speed (*i.e.* S_r) with decreasing negative curvature and a smaller increase in S_r with increasing positive curvature. Rutland and Trouvé, (1993) predicted similar behaviour for a lean methane/air Le = 1.2 flame, for negative curvatures, although correlations from their numerical simulations showed no noticeable increase in burning rate for positive curvatures.

However, there are limitations to the interpretations of Fig. 3.9 (d), because of the correlation of burning rate with flamefront curvature that is measured only in two dimensions. The real flame surface requires two components of curvature to fully characterise its topological profile in three dimensions. This fact implies that quantification of the relative enhancements of burning for the negative curvatures should not be trusted entirely. It would be expected that the correlation of true curvature with the burning rate would exhibit a stronger enhancement of burning for negative curvatures, when compared with the correlations of Fig. 3.9 (d). This is exemplified by the correlations of Chakraborty and Cant, (2005), where they use mean curvature (κ_m) as a measure of flame surface contortion, that show gradients for the negative curvatures in their correlation to be double that of Fig. 3.9 (d). A more

uniform correlation would be expected for burning rate with a two-dimensional curvature (κ), because for each of the measured curvatures herein there would have been an associated curvature in the direction perpendicular to the laser sheet. For example, a strong curving of the flame surface could exist out of the measuring plane, yet would appear to be flat in the HRR images of the flamefront, which results in an enhancement for zero curvatures in the correlations of Fig. 3.9. This would result in larger burning rates for zero curvatures relative to that for negative curvatures, hence a levelling of the correlation.

3.4 Conclusions

An improved method for the computation of curvature and its application to turbulent premixed flame correlations has been developed and tested in this study. It has been shown that use of a circle as a test curve for tuning the parameters of the curvature evaluation algorithm does not reliably yield the best choice of polynomial type. The rosette test curve method, whose development is reported here, was shown to perform more effectively, and to consistently allow the selection of an appropriate polynomial for smoothing the pixelated flame contour. A problem of the circle as a test curve is that its symmetry causes only one octant to possess pixels that are symmetrically unique. This leads to problems when investigating high curvatures, since for the corresponding small circles there will be very few unique pixels. Furthermore, employing the rosette test curve allowed for the setting of the maximum curvilinear rate of change of curvature $(d\kappa/ds)_{max}$ that occurs along the contour, which is however undefined for circle test curves. This extra

degree of freedom enabled the effect of $(d\kappa/ds)_{max}$ upon the choice of suitable polynomial to be studied. It was found that curves with larger $(d\kappa/ds)_{max}$ exhibit larger sensitivity of curvature measurement accuracy to the choice of polynomial. For the irregularly distorted flame contours investigated, a group of polynomial types was found to yield very similar results for the rosette testing performed. Furthermore, application of this group of polynomials yielded very similar correlations of burning rate with flamefront curvature, thus supporting the fidelity of the rosette testing results. Further to the predictable effects of polynomial length upon the distribution of measured curvatures, where shorter polynomials yield wider distributions and longer polynomials tend to smoothen the undulating flame contour, longer polynomials also seemed to lead to distortions to the true underlying relationship between local integrated HRR and flamefront curvature. This distortion is suspected to be due to systematic errors present in the values of integrated HRR due to the use of overly long polynomials, which can lead to a systematic overestimation of HRR due to inaccurate identification of the direction normal to the flamefront. Finally, qualitative differences of the correlations of integrated HRR and flamefront curvature were identified between our results and that of Ayoola *et al*. (2006). It was shown by using our improved method of computing curvature that an identifiable trend exists between all three flames studied, which was not present in the results of Ayoola *et al*. (2006). Furthermore, qualitative agreements were found between the experimental correlations reported here and the behaviour that would be expected based on the thermodiffusive argument, in addition to the DNS results within the literature.

Chapter 4

CARS Temperature Measurements in an Acoustically-Forced Premixed Turbulent Flame

In the previous chapter, the study of a turbulent premixed lean ethylene/air flame was presented. In this chapter, we present the study of a similar flame but on a different burner. The flame here was stabilised on a bluff body burner, in which the fuel mixture was acoustically forced with sinusoidal wave forms. This burner acts as a test-bed for the study of flame instability phenomena, which represent a problem in gas turbine combustion. Extensive experimental investigations have been done on this flame, in an aid to validate associated CFD models. One study was previously performed using two-line OH Planar Laser Induced Fluorescence (PLIF) to measure temperature (Ayoola *et al.* 2009) and comparisons with theory showed huge discrepancies. It is speculated that regions of the flame with low OH signal from PLIF resulted in measurement bias. Hence, it was decided here to try an alternative technique on the flame using Coherent anti-Stokes Raman Scattering (CARS) from vibrationally excited nitrogen molecules. The use of CARS circumvents the problem of probing regions of the flame with low species concentrations

such as OH. Nitrogen CARS is suitable in the case of an ethylene/air flame because of the excess levels of nitrogen present due to the use of air as the oxidant. The application of nitrogen CARS has shown that the results from the previous OH PLIF measurements were systematically biased and the reasons for this are explored. The chapter is organised as follows: the background motivates the need for taking accurate temperature measurements in the acoustically-forced flame. The details of how CARS was implemented to measure temperature are then outlined. The temperatures are scrutinised and compared to results from previous studies using alternative techniques.

4.1 Background

4.1.1 Motivation

Lean premixed combustion is becoming the preferred option for reducing emissions such as NO_X, and increasing fuel efficiency. However, this combustion regime can suffer from spontaneous fluctuations of the flame, and this effect is referred to as thermoacoustic oscillation. This is an undesired phenomenon and thus there are major research activities ongoing internationally in efforts to generate tools with which combustion instability can be understood, predicted and prevented. These efforts are usually based on computational fluid dynamical (CFD) models. Temperature is a key determinant in the onset and maintenance of thermoacoustic instability, since the heat release from the flame drives the oscillation and is highly temperature dependent (Dowling 2000a). Temperature is thus a key variable in CFD models, and comparison to experimental data allows validation of assumptions within the models. Although we use simple model systems in

this research, the work can be seen in the larger context of lean premixed prevapourised (LPP) gas turbine combustion. Phenomena as observed here on a laboratory scale add insight into the unsteady combustion in general. For example, large fluctuating temperatures as observed here from the model burner could be the cause of structural damage to real world combustors. It is therefore necessary to investigate the basic mechanics of this phenomenon, for its control and prevention.

The mechanism behind the flame instability is shown in Fig. 4.1, which portrays positive feedback between unsteady combustion, sound waves and pressure induced fluctuations in the fuel/air flow rate (Dowling 2000b). This condition can arise through small fluctuations in the fuel and air lines of the burner system, leading to a fluctuating equivalence ratio. This in turn leads to unsteady combustion and hence heat release rate.

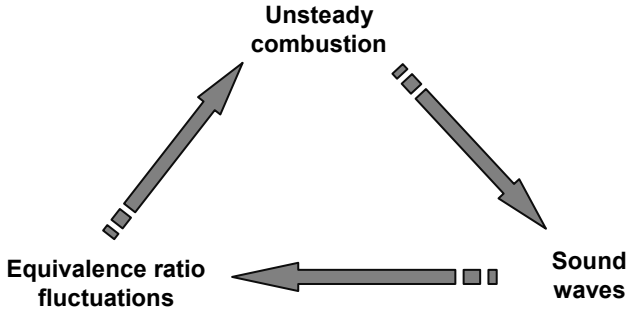

Figure 4.1: Instability cycle for lean premixed combustion.

This mechanism promotes self-excited oscillation of the lean flame with an amplitude that grows in time. The amplitude of the temperature and pressure oscillations can become sufficiently large that structural damage of the combustor ensues. For an instability to occur the Rayleigh criterion must be satisfied (Lieuwen *et al.* 1998), given by Eqn. 4.1.

$$\iint_{VT} p'(x,t) \cdot Q'(x,t)\, dtdV \geq \iint_{VT} \sum_{i} L_i(x,t)\, dtdV \tag{4.1}$$

Here, x is the spatial position within the combustor and t is time. V is the combustor volume, and T is the oscillation period. P' and Q' are the pressure and heat release rate fluctuations respectively. L_i are the energy losses caused by the damping mechanisms, such as viscous dissipation and acoustic dispersion through the combustor walls.

The left term of Eqn. 4.1 denotes the energy input into the system, and the right term denotes the losses caused by the dissipative processes. When the inequality is satisfied, unsteady combustion ensues. The establishment of an instability, is governed by the phase difference between the pressure and heat release fluctuations. In practice, it is not necessary that the heat release and pressure are exactly in phase to drive oscillations, although the driving will be largest when this happens. Some driving will occur even if heat release fluctuations lead or lag pressure oscillations.

The above criterion states the condition for the onset of instability. However, once the positive feedback cycle has been established, a limit cycle ensues

where the left term of Eqn. 4.1 balances with the right term. Once dynamic equilibrium has been established, oscillations of the flame may adopt large amplitudes, which determines its survival. The tolerance of the flame to large amplitudes depends on the frequency of small scale extinction events, which determines whether there is global extinction. At this point, and for a low equivalence ratio, the flame is said to undergo Lean Blow Out (LBO) (Zilwa *et al.* 2000). Appreciable oscillation and the associated blow out becomes more likely at leaner flame conditions, because the burning rate of leaner flames is more sensitive to changes in equivalence ratio (Lieuwen *et al.* 1999). Weaker flames are thus more easily disturbed than flames at stoichiometric conditions. The consequence of LBO is the possibility of spontaneous extinction of the flame, causing the potential for catastrophic failure in the context of aircraft engines. Furthermore, thermoacoustic instability can cause structural damage to the engine through unsteady combustion and the associated fluctuating temperatures and pressures.

4.1.2 Model Burner

As part of the ongoing effort towards understanding and controlling such combustion instability in LPP combustors, a number of experiments have been performed on a model burner. Its purpose is to mimic the behaviour of a large-scale industrial LPP combustor, which exhibits spontaneous flame pulsation. The model burner is designed with both ease of optical access and geometrical simplicity in mind, in order to facilitate experimental and numerical studies respectively. The burner mimics LPP combustor pulsation by acoustically-forcing the fuel/air mixture sinusoidally using loudspeakers to

force the gaseous flow. The model burner provides a basis for studying flame instability with a large effort across many research groups at the University of Cambridge. Specifically, it provides an experimental test-bed for validation and development of CFD models of the flame at various conditions, such as amplitude and frequency of acoustic-forcing, and overall flowrate. Such studies include velocity field measurements using Particle Imaging Velocimetry (PIV) (Hartung *et al.* 2008; Hartung *et al.* 2009), two-line OH-PLIF thermometry (Ayoola *et al.* 2009), and characterisation of the burner dynamics (Balachandran *et al.* 2005). However, with ongoing development of CFD models on the flame, there is continuing demand for an up-to-date database of experimental variables such as temperature, species compositions, reaction rates and flow-field velocities.

4.1.3 Previous Studies

One motivation for the present work was the non-perfect data arising from experimental limitations in a previous study to measure temperature by OH PLIF (Ayoola *et al.* 2009). Phase-averaged temperatures in the acoustically-forced burner were qualitative, as demonstrated by the 20 % precision (Ayoola 2005) and a suspected systematic error. These problems are discussed in detail in section 4.1.3.2 below. It should also be noted that the temperature measurements presented in this work and in previous studies were performed at fixed phase-angles over the acoustic-cycle. This allowed mean temperatures to be determined for a particular phase-angle, which is referred to here as the 'phase-averaged temperature'. In light of all the relevant experimental data available for CFD validation, models can then be

used as a tool for ultimately designing combustors that do not exhibit thermoacoustic instability. With regard to the acoustically-forced bluff body model burner, there is still scope for improvement of CFD models by way of validation with experimental data, owing to the fact that there are still significant limitations to CFD. Improvement is especially important with regard to temperature data, since temperature is a key parameter in combustion, as already described previously. For example, validation allows the effects of incorrect temperature boundary conditions to be discriminated against effects from other assumptions in CFD. These are treated in turn for the model burner here, whose flame was simulated using Unsteady Reynolds Averaged Navier Stokes (URANS) CFD-code by Armitage *et al.* (2006).

4.1.3.1 URANS-Modelling Limitations

Thus far, the only modelling performed on the model burner is URANS (Armitage *et al.* 2006). This is low-order CFD, which only simulates the large-scale fluctuations in the flow field and implements sub-grid models that invoke assumptions about the combustion process. An example assumption in the implementation of URANS by Armitage *et al.* (2006) was the boundary condition for temperature. They assumed adiabatic wall conditions for the 3 mm thick quartz enclosure that surrounded the flame (see Fig. 4.4 for the setup). This condition is unrealistic in light of the appreciable heat loss that would occur at the surface of the enclosure. This is confirmed by Balachandran *et al.* (2005), who measured the rate of heat release in the flame, where the heat release is seen to be significantly less at the flamefront located adjacent to the boundary in contrast to that of the URANS model.

Adiabatic conditions in the model would result in higher temperatures at this flamefront leading to faster reaction rates. To overcome the simulation of incorrect burning rate, an alternative wall-function within the Reynolds stress model of URANS could be developed. This could then be validated by comparing the resulting temperatures from the modified URANS code with experimental ones.

Another manifestation of the imperfect boundary conditions is the slower rate of propagation of the vortex in the reactants that rolls-up the flamefront during the acoustic cycle. This is seen by comparing the temperature maps of URANS with that of the OH PLIF data of Ayoola *et al.* (2009) for the same flame conditions, and this effect is demonstrated later in section 4.3.1.2. The effect could be due to the adiabatic wall condition, which raises the overall temperature of the burned gases and increases their viscosity. This would hence retard the rate of vortex propagation through the more viscous burned gases. However, there is another possible contribution to the difference in the rates of propagation. The URANS model assumed that the velocity profile was spatially uniform at the inlet. In reality, the profile would be more parabolic, due to the frictional drag that is exerted on the incoming flow by the inlet channel walls. Such a profile would thus consist of faster flowing gas at the profile centre, and may promote a quicker rate of vortex propagation in contrast to that predicted by URANS, as proposed by Ayoola *et al*. (2009). Again, upon validation of a modified URANS model, as described above, the effect of unnaturally high temperature due to the boundary condition could be separated from the effect of an imperfectly assumed inlet velocity condition.

In order to validate URANS models, experimentally determined temperatures are needed. These can then be compared to the temperatures simulated by the model at the same flame conditions. Such a temperature database has already been generated by Ayoola *et al.* (2009), who used two-line OH PLIF. However, there were experimental limitations to the technique, which rendered the data to be somewhat qualitative. These technique and its limitations are considered in the following section.

4.1.3.2 Previous Temperature Measurements

The two-line OH PLIF thermometry of Ayoola *et al.* (2009) involved the recording of two Laser Induced Fluorescence (LIF) images of OH taken in rapid succession (*i.e.* pseudo-instantaneously), excited by two lasers at different wavelengths. The wavelengths correspond to the $P_1(1.5)$ and $Q_1(5.5)$ transitions in the vibrational band (1,0) of $X^2\Pi \rightarrow A^2\Sigma^+$ in OH. For a single measurement, the two LIF images of OH were used to compute the temperature using the two-line equation, whose form is similar to the two-line atomic fluorescence equation described in chapter 2. Example images of temperature, and OH fluorescence excited at $P_1(1.5)$, are shown in Fig. 4.2.

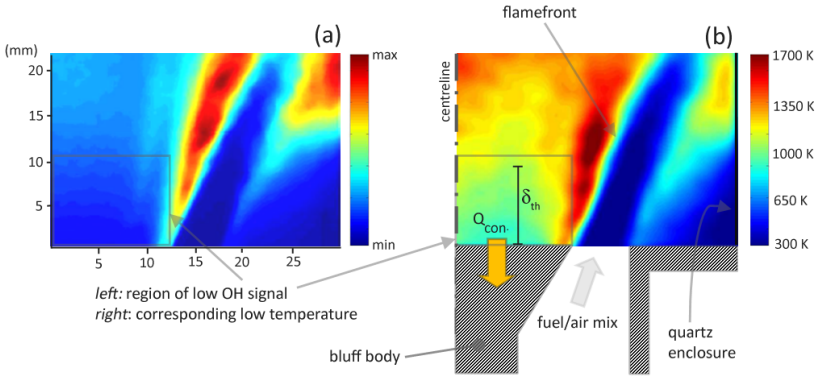

Figure 4.2: Cross-sectional images of phase-averaged-: (a) OH-PLIF at one excitation wavelength $P_1(1.5)$, and (b) two-line OH-PLIF temperature.

Here, the images are phase-averaged values at a point in the acoustic cycle. The LIF images were generated by directing an expanded laser beam in the form of a sheet through the centre of the flame; this corresponds to cross-sectional images. Figure 4.2 (a) shows OH PLIF normalised by its peak value. The corresponding temperature map is shown for the same region in the flame in Fig. 4.2 (b). This region is demarcated by the centreline (axis of the burner) on the left and the wall of the quartz enclosure on the right. The base of the region is bounded by two metal sections, one of which is the bluff body to the left. The fuel/air mixture flowed between the sections, where two flamefronts were stabilised on the lips of the sections.

At a fuel equivalence ratio of 0.55, the adiabatic flame temperature is 1706 K (Morley 1997). It would be expected that the region of burned gas between the centreline and the left flamefront in Fig. 4.2 (b) would be close to the adiabatic temperature, owing to the proximity to the flamefront. However,

Fig. 4.2 (b) clearly shows a large cool region above the bluff body with a minimum temperature of about 900 K. It is plausible that the cool region could be due to thermal conduction of heat to the metal bluff body, as denoted by $Q_{con.}$ However, the amount of conduction seems excessive owing to the extent of the cool region prevailing in the burned gases. This is allied with the finding that the thermal boundary layer thickness, δ_{th}, as estimated using correlations, is approximately 10 mm as denoted in Fig. 4.2 (b) (see Appendix B for details). The thickness is defined as the distance over which the temperature rises to 99 % of the core temperature of the burned gases. If one assumes the actual core temperature to be close to 1700 K (~adiabatic temperature), then it is evident that the extent of the cool region in Fig. 4.2 (b) seems excessive. The value of δ_{th} suggests that the extent of the region of cooling in reality could be significantly less, and so is the corresponding rate of thermal conduction to the bluff body. Furthermore, the local temperature gradient over the distance δ_{th} is near zero, as seen in Fig. 4.2 (b), which is inconsistent with the idea of significant thermal conduction to the bluff body.

In light of the above, the cool region in the burned gases seems artificial, and could therefore be caused by systematic error in the two-line OH LIF temperature measurement. One likely source of error would be the subtraction of either too much or too little background from the raw OH LIF images. This imperfect background correction would affect the two-line temperature map, and more strongly in the regions corresponding to low OH fluorescence intensity, as represented by the boxed region in the flame of Fig. 4.2. To illustrate this qualitatively, an error from incorrect background can be added to a theoretical OH signal to investigate how it affects the two-line

temperature. The two-line temperature subject to an error in the background is plotted versus the error in the background, relative to the $P_1(1.5)$ OH signal in Fig. 4.3. Here, the blue plot clearly deviates from a theoretically constant temperature of 1700 K (black plot), with for example a 6 % error in the $P_1(1.5)$ signal to yield a lower temperature of 900 K (*i.e.* a 47 % error in temperature). For the temperature to decrease with an increase in relative error, a condition is required that relates the background error in the $Q_1(5.5)$ OH signal (δ_Q) to that of the $P_1(1.5)$ signal (δ_P). In this case, $\delta_Q < r.\delta_P$, where r is the fluorescence ratio in the two-line equation that corresponds to the temperature of 1700 K.

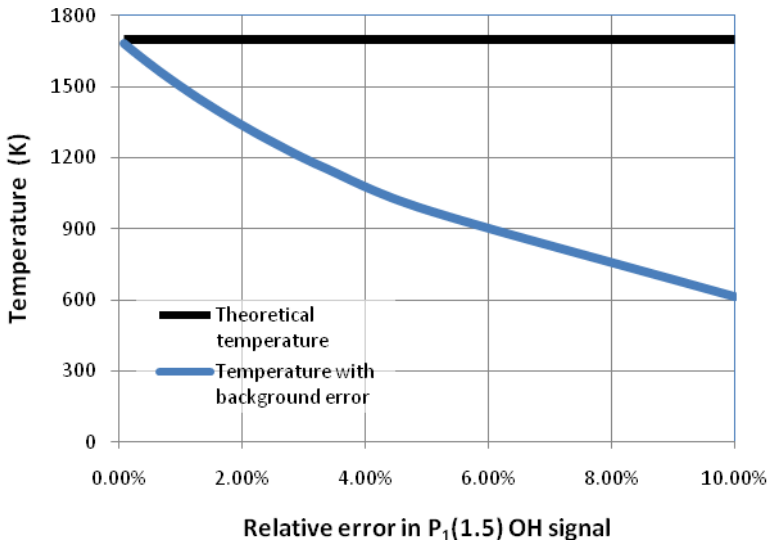

Figure 4.3: Plot illustrating how an example error in the background correction of an OH-PLIF signal can affect the computed two-line temperature. The relative error is the error left from incorrect background correction divided by the correct signal.

Under these conditions, it is clear that temperature drops with an increase in relative error. In the case of the burned gases in the flame shown in Fig. 4.2, low OH signal raises the relative error for a fixed error in background and thus creates an artificial decrease in temperature.

4.1.4 Aims

It is seen that the implementation of two-line OH PLIF to the acoustically-forced bluff body burner may not yield reliable temperatures in the burned gases, especially above the bluff body where OH signals are low. Planar OH LIF may not deliver quantitative results, but is better suited to provide an instant image of the flame shape and behaviour with time. An alternative technique to measure temperature with improved accuracy is therefore needed if the results are to be used to validate URANS models of the model burner. Coherent anti-Stokes Raman Scattering (CARS) is such an alternative but it is a point measurement technique. Although CARS cannot therefore provide information on the instantaneous flame shape, it is more accurate. Accuracy is greatly improved for the application of CARS in vibrationally excited nitrogen molecules. This is because of the abundance of nitrogen in lean fuel/air flames, where the concentration of nitrogen is high and approximately uniform throughout the flame. This overcomes the problem of potential susceptibility to error in temperature incurring from non-perfect background correction, as was the case in two-line OH PLIF when OH signals were low. This is the major motivation for the use of vibrational nitrogen CARS for the model burner, in order to acquire quantitative temperatures for the goal of validating URANS models. The use of vibrational CARS is also preferable to

pure rotational CARS because of the increased temperature sensitivity at typical flame temperatures (Seeger and Leipertz 1996). Furthermore, vibrational nitrogen CARS offers a better accuracy of about 1 % at ~2000 K (Hall and Eckbreth 1981; Hartung *et al.* 2006), when compared to that of two-line OH PLIF which offers an accuracy of about 5-10 % under optimal conditions (*i.e.* in the absence of the problem of low OH concentrations) (Seitzman *et al.* 1994; Palmer and Hanson 1996).

4.2 Experimental Method

This section describes the vibrational nitrogen CARS setup used to record temperatures in the model burner in an effort to reanalyse the dataset of Ayoola *et al*. (2009). Our method works in principle by taking point measurements within the cross-section of the flame. The cross-section is the same as previous studies on this burner. Phase-averaged temperatures were recorded by triggering the laser to a phase-angle and averaging the measurements over a number of cycles. This process was repeated over numerous points within the same cross-section to allow an interpolated map of temperature to be generated, which allows for a direct comparison to previously obtained phase-averaged temperature maps from the OH technique. Details of the burner and the CARS technique are given below.

4.2.1 Model Burner

The acoustically-forced bluff body burner that was used in this study is depicted by its central cross-section in Fig. 4.4. The 10 kW burner was

supplied by a lean mixture of air and ethylene at a fuel-air equivalence ratio of 0.55. The flow was acoustically forced by passing sinusoidal sound waves through the mixture, using a signal generator (TTi TGA 1242) and an 80 W preamplifier. This caused the volumetric flow rate to vary periodically, and hence induced oscillations within the flame.

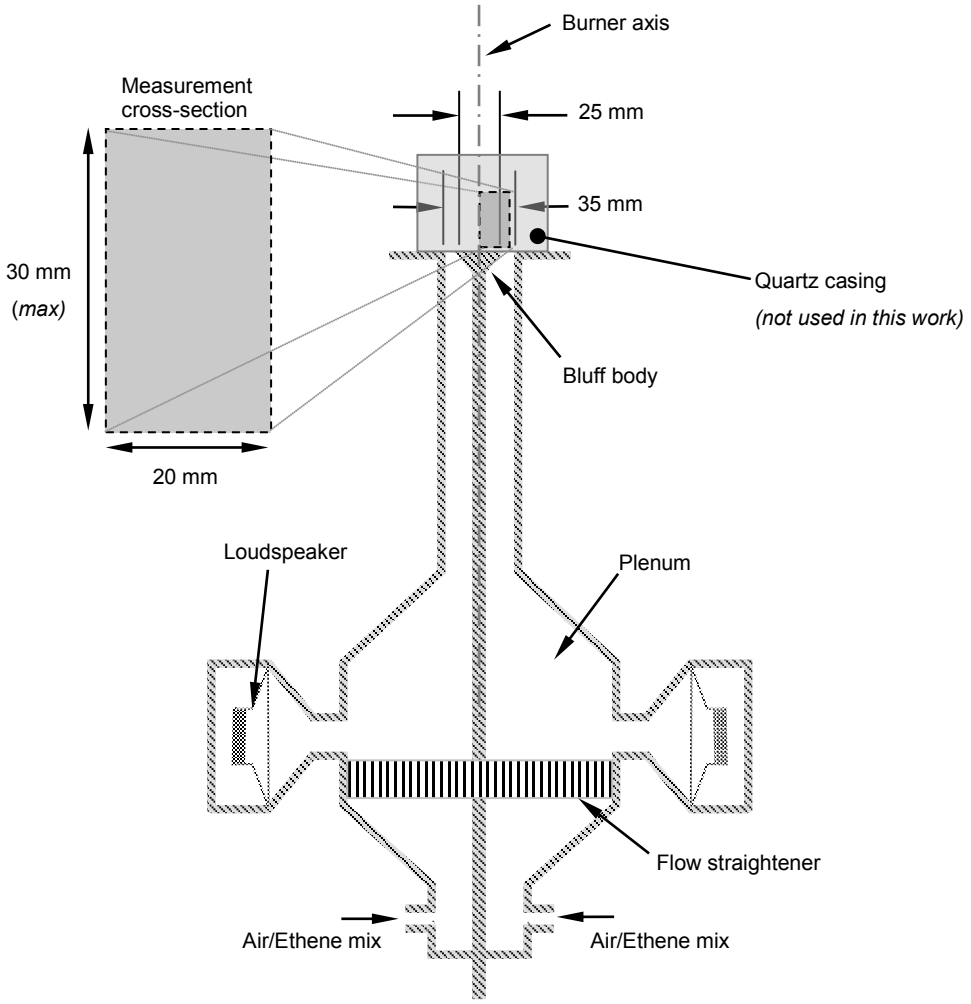

Figure 4.4: Schematic of the acoustically-forced bluff body burner cross-section.

The flow conditions described in the paragraph below originate from the work of Balachandran, (2005); Ayoola *et al.* (2006) and Ayoola *et al.* (2009). A limited number of flow conditions could only be investigated in this work, owing to time constraints. This stems from the long time needed to record a sufficient number of temperatures, in order to generate interpolated temperature maps using CARS. Therefore, the parameters of the flow conditions were carefully selected, in order to acquire sufficient information about the evolution of the flame and its structure. One such parameter is the frequency of acoustic forcing, which was fixed at 160 Hz, corresponding to one of the axial resonant frequencies of the burner's plenum. This frequency is of interest, as it yields a large amplitude of oscillation in the flow for a given voltage applied to the speakers, owing to the resonant condition (Balachandran *et al.* 2005). The amplitude of oscillation was set to a ratio of $A = 0.65$ (expressed as half peak-to-peak amplitude in burner outlet gas velocity to time-averaged flow velocity). The time-averaged flow velocity corresponds to a Reynolds number, which is based on the cross-sectional area equivalent diameter of the burner exit, of Re = 17000. This rate of flow resulted in a turbulent flame that was stabilised on the central bluff body. The bluff body created a blockage ratio of 50% and was chosen based on a scaled model of an RB211 Rolls-Royce combustor (Armitage *et al.* 2004). For the selected flow conditions described above, three phase angles within the acoustic cycle were chosen for the generation of temperature maps. Only three were chosen, due to the large number of measurements needed for each phase angle. Nevertheless, a choice of three allows the evolution of the flame to be observed within the temperature maps. The specific phase angles, which were based on the burner exit velocity fluctuation throughout the cycle, are 90^{o},

150^{o} and 210^{o}. These were chosen, because the flame structure changes the most over these three phases, as observed in the results from Ayoola *et al.* (2009). The CARS point measurements were taken in the measurement cross-section shown in Fig. 4.4. The cross-section represents the maximum extent of point measurements with a height of 30 mm and a width of 20 mm. The left edge lies on the burner axis and the bottom edge is 3 mm above the bluff body surface.

It should be noted that all the above conditions of the burner reproduce that of Ayoola *et al.* (2009). However, the quartz casing at the top of the burner, as shown in Fig. 4.4, was absent in this work. The casing was part of the original model burner, but needed to be removed so that CARS measurements could be made. The curvature of the quartz casing presented a problem with regards to beam alignment. Very tight beam alignment is required, so that a CARS signal could be generated. The removal of the casing potentially presents a problem in the subsequent interpretation of temperatures from CARS. Since the casing acts to prevent air entrainment from the surrounding atmosphere, the removal would cause the incoming fuel/air mixture to be diluted. Leaner fuel/air mixtures generate lower temperatures upon burning, and this would not make possible the valid comparison of CARS temperatures to that of URANS.

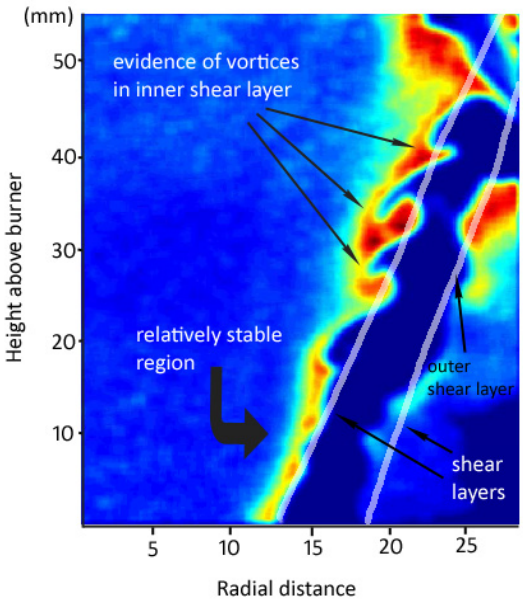

Figure 4.5: Instantaneous image of OH LIF excited at $Q_1(5.5)$ revealing the development of the shear layers along the flamefronts for a non acoustically-forced flame (adapted from Ayoola 2005).

However, the amount of air entrainment would depend on position in the flame. This would be caused by the development of vortices at the shear layer between the atmosphere and the incoming fuel/air mixture. With increasing height from the burner there is greater vorticity at the shear layer, and this induces more mixing between the surrounding air with the fuel/air mixture. This would cause greater dilution of the mixture further up the flamefront. Figure 4.5 illustrates the effect of increasing vorticity with height for both the inner and outer shear layers for a non acoustically-forced flame in the presence of the quartz casing (Ayoola 2005). This is demonstrated indirectly by the increase in wrinkling of the flamefronts with height. This is because

the vortices act to contort the flamefront. Closer to the burner, Fig. 4.5 shows that the shear layers are more stable. This implies that the amount of air entrainment is less, and so the fuel equivalence ratio local to the flamefront here is closer to 0.55. With the aid of turbulent mixing, the burned gases close to this region would therefore exhibit temperatures closer to the adiabatic limit corresponding to an equivalence ratio of 0.55. Although this cannot be proven *a priori*, subsequent temperature measurements would confirm this if values are close to the adiabatic limit. Any air entrainment would lower the temperature noticeably, since the adiabatic temperature drops more steeply with a decrease in equivalence ratio at lean conditions (Turns 2000). Measured temperatures close to the bluff body in the burned gases would therefore lend themselves to a more valid comparison to URANS results.

4.2.2 CARS Setup

Figure 4.6 shows the setup for the generation of the CARS signal in the flame, in order to measure temperature. The figure caption describes the various components within the setup. A number of these optical components from the previous setup employed in the research group were exchanged and optimised by the author, in order to maximise the transmission of laser power to the measurement volume. However, the major improvement concerns the replacement of the main laser source. This comprised a frequency-doubled 10Hz-pulsed Nd:YAG laser, which replaced an older model from the 1980s. The advantages of the new laser (Continuum Surelite) were twofold, namely: the spatial profile of the beam was improved from being bimodal to Gaussian TEM_{00}, and the temporal resolution of the new laser was improved through

the use of a more reliable Q-switch. Using the new Nd:YAG laser and the frequency doubling, green light at 532 nm was emitted and this was used to pump a dye laser that emitted a red beam centred at 606 nm with a full width at half maximum (FWHM) of 6 nm. To achieve this, the dye composition was optimised to yield maximum power near 606 nm. The resulting dye composition was 1.11×10^{-4} M Rhodamine 640 in ethanol.

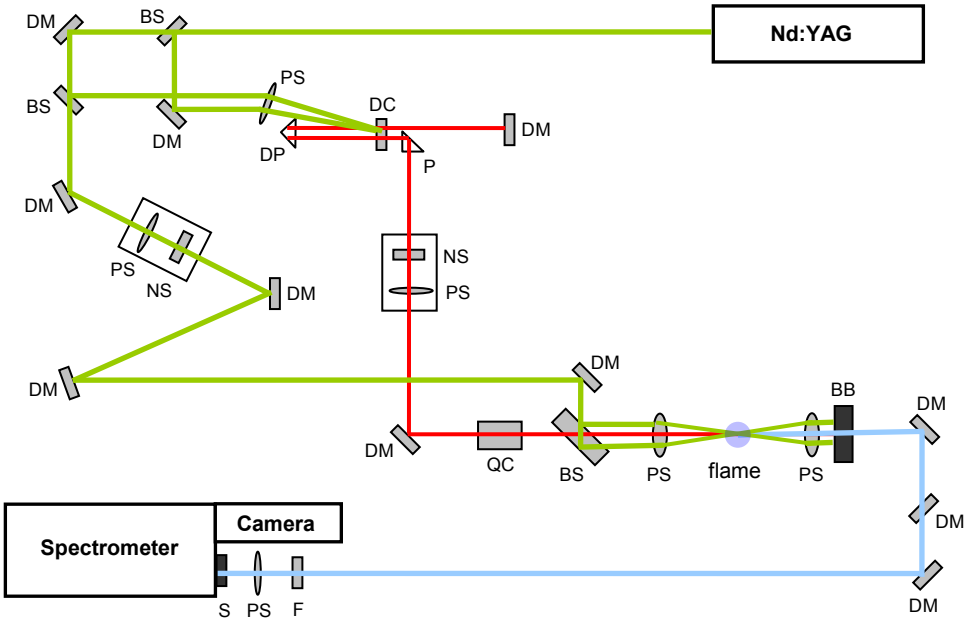

Figure 4.6: The CARS optical setup used here. Description of the components: DM - dichroic mirror; BS – beam splitter; PS - positive spherical lens; NS – negative spherical lens; DP - prism with dichroic coating; P - prism; BB - beam block; QC - quartz cylinder to adjust height of beam; F - filter; S - slit; DC - dye cell.

The output of the Nd:YAG laser was split using beam splitters (BSs), where approximately 7% of the incident beam was directed into the dye laser cavity

for both the oscillator and amplifier parts of the dye laser. The remaining green beam was expanded by using a Galilean telescope and allowed the collimation of the beam to be finely tuned through adjustment of the distance between the PS and NS lenses. After expansion, the beam was reflected to and from several dichroic mirrors (DMs), in order to create a time delay that compensated for the extra time photons spent inside the dye laser cavity, thus ensuring that the pump (532 nm) and Stokes (606 nm) beams arrived simultaneously at the measurement point during the 10 ns laser pulse. The dye laser output emitted broadband light, whose wavelength was spectrally centred at 606 nm with a FWHM of 6 nm. The output was generated by pumping both the oscillator and amplifier sections, which used a common dye cell. The Stokes beam was then expanded similarly to the pump beam, as described above, in order to match the diameters of all beams that reach the measurement volume. Both the quartz cylinder (QC) and beam splitter (BS) provide sufficient degrees of freedom to position and orient the pump and Stokes beams, in order to satisfy the folded BOXCARS phase-matching criterion (see chapter 2 for general methodology). The three beams were then focussed through a PS lens with a focal length of 290 mm, such that the beams overlap as much as possible at the measurement volume resulting in the generation of the CARS signal beam near 473 nm. Signal generation is only possible if the pump and Stokes beams are oriented according to the phase-matching condition shown in chapter 2. The angle of inclination of the Stokes beam to the horizontal is related to the angle of separation between the two pump beams, given by Eqn. 4.2.

$$\cos\theta = \frac{4k_p^2 \cos^2\alpha - k_{as}^2 + k_s^2}{4k_p k_s \cos\alpha} \tag{4.2}$$

Here, $k_i = 2\pi/\lambda_i$ for λ_p = 532 nm, λ_s = 606 nm and λ_{as} = 473 nm. h and α can be calculated with reference to Fig. 4.7.

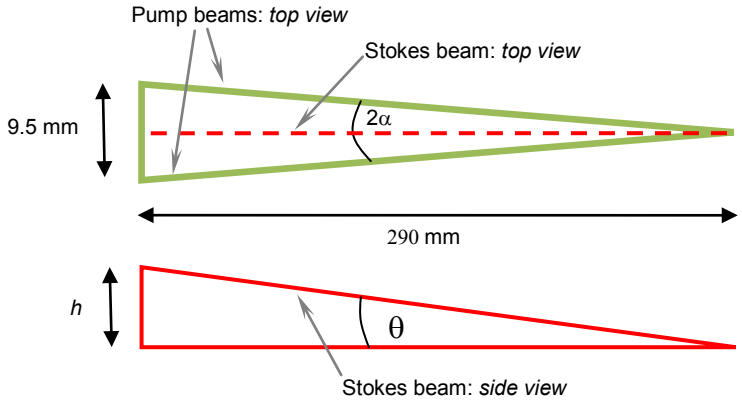

Figure 4.7: Top and side elevation of the beam arrangement for the folded BOXCARS scheme.

Once positioning and orienting of the beams had been achieved optimally using the PS lens, quartz cylinder and beam splitter, all the beams were recollimated using another 290 mm PS lens. The paths of the resulting pump and Stokes beams were blocked using a beam block (BB) allowing only the CARS beam to pass. The CARS beam then passed through a dichroic mirror (DM) to filter-out the residual 532 nm light, whereupon the beam was spectrally resolved. The filtered beam was resolved by directing it to a large spectrometer (SPEX) of length 1.2 m and theoretical resolution 0.004 nm at a

detection wavelength of 473 nm. The spectrum was detected and recorded on a laser-triggered 14-bit back illuminated EMCCD camera (Andor iXon DV887ECS-BV). This camera replaced an older 1980s CCD version with a quantum efficiency of 65 %. The new camera offered a far higher quantum efficiency of 95 %, thus allowing the weak CARS signals to be detected with less noise. The 512 by 512 pixel chip (16 μm pixel size) on the new camera was capable of being cooled using an in-built Peltier system with the possibility of further cooling by passing water around the chip. In this work, the chip was cooled to no more than –30 ^{o}C and operated without water cooling. This reduced the quantity of dark noise to negligible levels whilst not inducing condensation on the chip, which can damage the camera circuitry.

4.2.3 Spectral Evaluation

Once the CARS signal was spectrally resolved, single shot spectra were recorded on a computer. To enable proper spectral evaluation, background levels and non-resonant spectra in room-temperature propane were also recorded. These additional data are needed to compensate for background and dye laser contributions that distort the underlying CARS spectra from which temperature can be measured. The two are treated in turn. Firstly, the background originates from visible flame emission, contribution from the camera electronics, and stray light external to the spectrometer. Each CARS spectrum was corrected for background. Acquisition of background spectra involved recording whilst the Stokes beam was blocked. One hundred such spectra were recorded to yield an averaged background spectrum that was subtracted from each subsequently acquired CARS spectrum. Secondly, each

CARS spectrum must be divided by a non-resonant spectrum. This corrects for the non-uniform dye laser profile and any irregularities in the detection system, such as defective pixels on the camera chip. The non-resonant spectrum was generated by recording a CARS spectrum in propane at room temperature. Propane does not possess any resonant transitions in the wavelength region of the dye laser emission, and instead relies on the weak non-resonant processes that naturally occur simultaneously with resonant CARS processes (Eckbreth 1996). The intensity of the propane spectrum depends only on the laser beam intensity, and therefore mimics the spectral profile of the dye laser. The propane spectrum was compensated for background intensity in exactly the same manner as for the nitrogen spectrum. The compensated experimental CARS spectrum can be computed using Eqn. 4.3, where the N_2 and propane background, and propane spectrum were taken as averaged values over 100 repetitions.

$$compensated\ CARS\ spectrum = \frac{resonant\ CARS\ spectrum - N_2\ background}{propane\ spectrum - propane\ background} \qquad (4.3)$$

The correction of the experimental CARS spectra by use of the above relation is a first step to inferring temperature from the data. After correction, a computer program named CARSFIT (Clark *et al*. 1990) was used to generate a library of theoretical spectra at a range of temperatures: 300 – 2000 K in steps of 10 K. Due to the functional limitations of the CARSFIT software, a program was compiled in this work to manage the least-squares fitting of each experimental spectrum to theoretical spectra within the library. The best

match within the library of theoretical spectra allowed for the identification of the measured temperature to within 5 K.

4.2.4 Spatial Resolution

Using the setup, as described above, the spatial resolution was estimated in order to ensure that thermal lengthscales could be determined with sufficient accuracy. The measurement was conducted by using a hypodermic needle that was connected to a propane source. Propane flowed from the tip of the needle (diameter of 0.5 mm), whose tip intersected orthogonally to the horizontal plane of the pump beams. The needle was then translated along the beam direction and the CARS spectra were recorded for each needle position. The length of the measurement volume was estimated from recording the peak intensity of the CARS spectra and then noting the position from where the peak intensity subsided to half the maximum value along the translation path. This yielded a length of approximately 5 mm. The diameter of the measurement volume was also estimated by considering the overlap of the beams yielding a value of approximately 100 μm. Taking the above values as upper estimates, the measurement volume is therefore of the order of 0.05 mm^3.

4.3 Results and Discussion

Figure 4.8 shows a match between a theoretical and an example single-shot experimental CARS spectrum measured at a typical flame temperature of 1600 K in the bluff body burner. The least-squares fit shows a good

agreement, as shown by the good overlap of the spectra and the square of the residual; here the residual is defined as the difference between the theoretical and experimental spectra. It should be noted that the experimental spectrum in Fig. 4.8 is derived from a single shot.

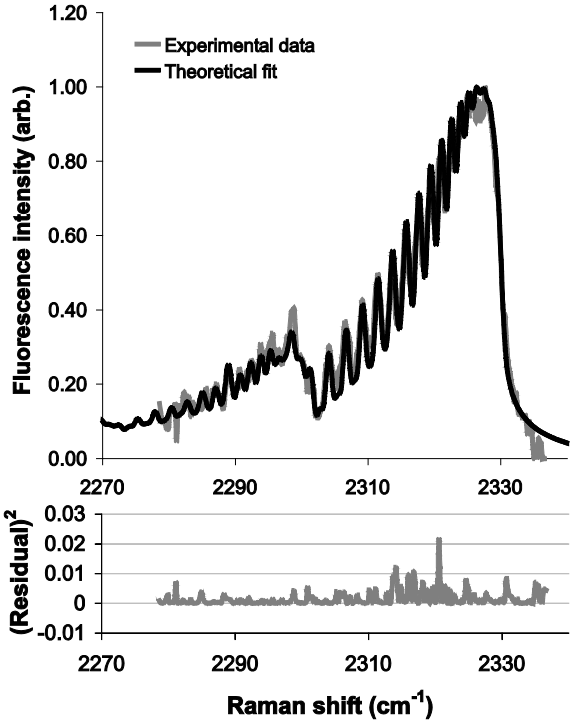

Figure 4.8: Example match for a single-shot experimental spectrum with a theoretical one at a temperature of 1700 K in the bluff body burner.

Although there is a good fit, the match is less than perfect as shown by the non-zero magnitudes in the plot of the square of the residual. This is caused by the dye laser spectral profile being recorded as an average, instead of

simultaneously capturing the instantaneous dye laser- and CARS-spectra. Simultaneous capture would otherwise allow all CARS spectra to be normalised by their corresponding dye laser spectrum, thus eliminating the effect of non-perfect referencing. Nevertheless, good fits were obtained and this was reflected in the spread of temperatures measured in a test flame. The test flame was steady, flat and laminar, whose reactants composed of methane and air at an equivalence ratio of one. The average temperature of the test flame was measured to be 2180 K with an FWHM spread of 92 K (4.2 %). This served as a quick check of the validity of the CARS setup used here, whose temperature and precision were in close agreement with previous studies (Snelling *et al.* 1987; Hartung *et al.* 2006). Furthermore, it is possible that non-perfect referencing could introduce systematic error. This was checked by making a fit to an ensemble-averaged CARS spectrum over 100 single shot spectra and comparing the resulting temperature to the average temperature derived from the fitting of single shot spectra. In the case of the ensemble-averaged spectrum, the dye laser profile is also averaged, therefore the fitting in this case is equivalent to perfect referencing. By comparing the two methods to obtain the mean temperature, the effect of non-perfect referencing on accuracy can be investigated. Here it was found that it introduced an error of up to 0.5 % at temperatures between 1400 and 1700 K.

4.3.1 The Acoustic Cycle

4.3.1.1 Dynamics of the Acoustically-Forced Flame

Before taking a look at the temperatures in the acoustically-forced flame derived from the fitting of CARS spectra, a closer look at the dynamics of the flame is required to assist in the interpretation of the results. Figure 4.9 shows the phase-averaged velocity flowfield and heat release rate (HRR) of the central cross-section of the flame for the three phase angles studied here at the conditions described in the figure caption. These data are from URANS simulations as reported in Armitage *et al.* (2006). The cross-section is split into two panes, where the line of symmetry is the centreline at a radial position of zero. The left pane shows the velocity vector field and the progress variable (based on the fuel mass fraction) contour at a value of 0.5. The contour allows one to delineate the position of the flamefront. The right pane depicts the HRR, whose profile corresponds to the shape of the progress variable contour. Here, the shape of the HRR profile and progress variable contour represent the time-averaged position of the flamefront, and is termed the flamebrush. The images correspond to the flame conditions where the inlet velocity varies with time as shown by the plot in Fig. 4.9. The three phase angles are also marked on the time trace for 90^{o}, 150^{o} and 210^{o}.

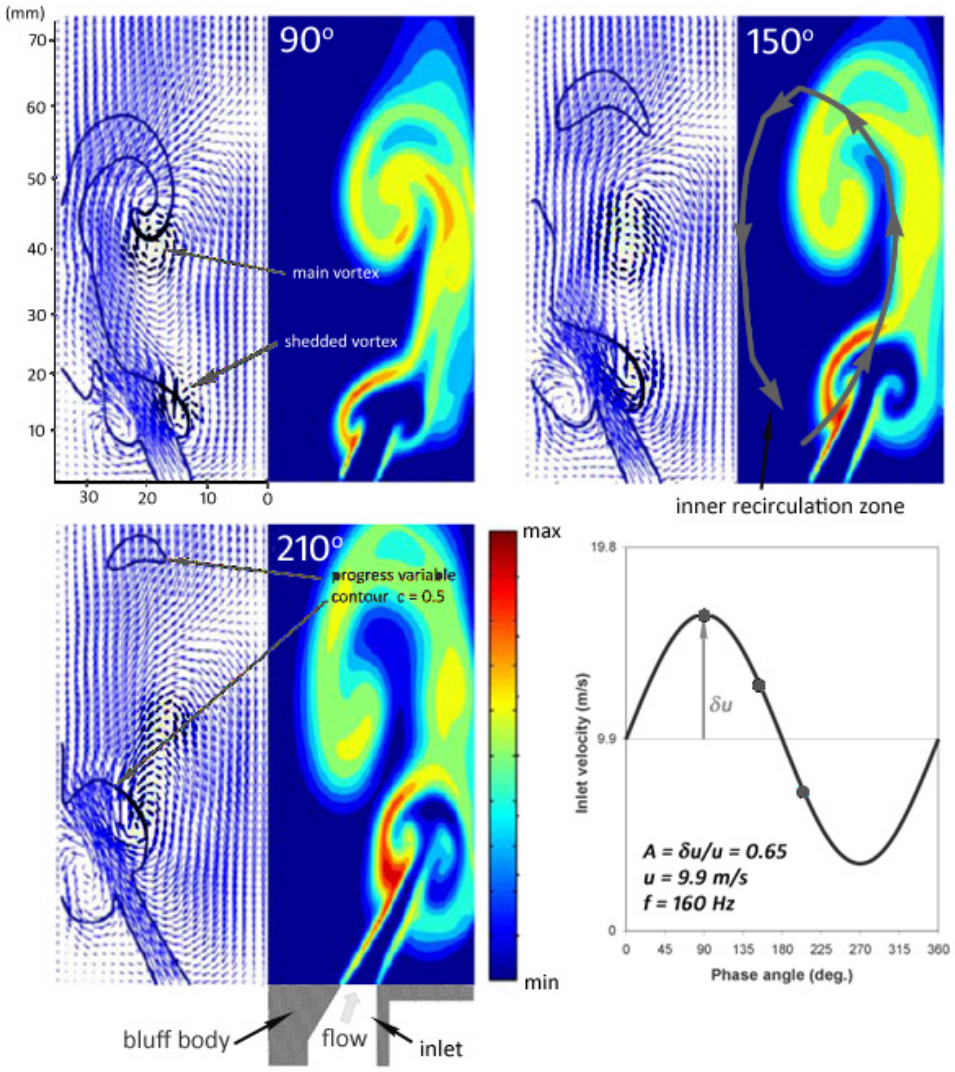

Figure 4.9: Depiction of phase-averaged flowfield and heat release rate (HRR) in the central cross-section of the acoustically-forced flame at a forcing frequency of 160 Hz, amplitude ratio of 65 % and a mean flow velocity of 9.9 m/s for three phase angles (adapted from Armitage *et al.* 2006).

It is seen in the velocity flowfield that there exist two vortices, as shown by the darkened vectors in Fig. 4.9. The top one is the main vortex, which remains in a relatively stationary position over the course of the acoustic cycle, and this forms the inner recirculation zone. The main vortex twists the upper reaches of the flamebrush down toward the burner, as shown by the rotated progress variable contour at a height of about 50 mm for the phase angle 90^{o}. Another vortex sheds from the inlet at the beginning of the cycle and propagates upward toward the main vortex, where coalescence of the two occurs. The shedded vortex rotates in the same direction as the main vortex and twists the flamebrush down toward the burner, as shown in Fig. 4.9. The upward flow of reactants at the inlet results in two flamefronts, one of which is stabilised on the lip of the bluff body and separates the cold unburned gases from the region of hot burned gases in the inner recirculation zone. The corresponding flamebrush is inclined and approximately straight for a certain height until it is twisted down toward the bluff body. This flamebrush distortion is caused by the propagation of the shedded vortex which emerges from the inlet. The propagation is synchronous with the sinusoidal perturbation of the reactant flow, such that during an increase in the volumetric flowrate in the cycle a new vortex propagates upward and curls the flamebrush.

4.3.1.2 Comparison of Temperatures

Figure 4.10 shows maps of phase-averaged temperature on the cross-section of the axi-symmetric flame that was subjected to acoustic-forcing. The maps correspond to the right half of the flame in Fig. 4.9. The temperatures from the CARS technique, along with temperature maps derived from OH PLIF (Ayoola *et al*. 2009) and URANS (Armitage *et al*. 2006), are shown for the three phase angles 90^{o}, 150^{o} and 210^{o}. The left edges of the maps in Fig. 4.10 coincide with the burner's central axis. The bottom edge of the maps is taken to be 3 mm above the burner surface, whose length comprises of two sections: a 12.5 mm radius bluff body and a 5 mm gap from which the reactants flowed.

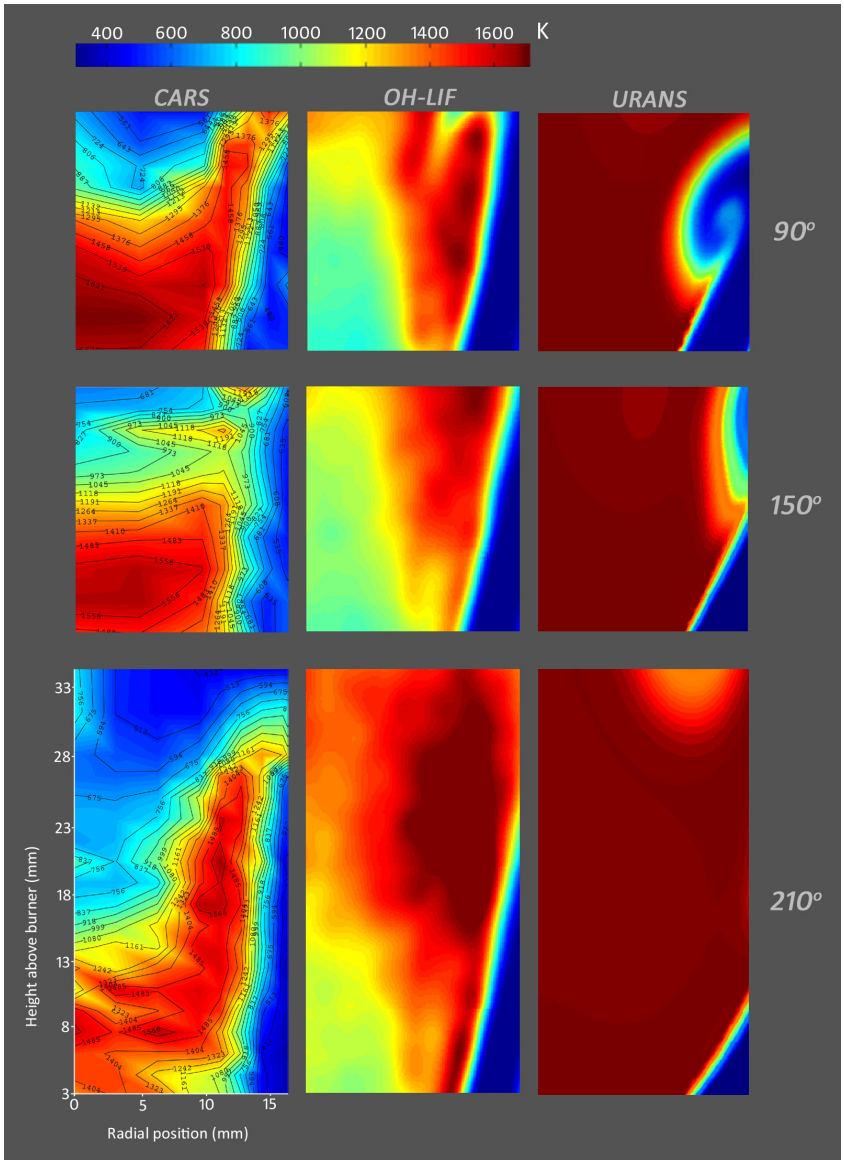

Figure 4.10: Phase-averaged temperature maps for the central cross-section of the flame at three phase angles. The figure consists of results from: *left column*: CARS, *middle column*: OH PLIF (Ayoola *et al*. 2009), and *right column*: URANS (Armitage *et al*. 2006).

By comparing the temperature maps from the three techniques in Fig. 4.10, it is clear that the steep temperature rise from right to left within each image is attributable to the presence of the flamebrush. The temperatures of the hot regions to the left of the flamebrush are in good agreement with the corresponding regions shown by URANS. However, the CARS results show that in general there is a gradual reduction in temperature of the order of 200 K in the hot region through the cycle from 90^o to 210^o. This difference in behaviour through the cycle is likely to be caused by heat loss to the surroundings that is not present in the adiabatic case of URANS. Towards the beginning of the cycle at 90^o, for the experimental results, the shedded vortex convects a lot of heat from the highly twisted flamebrush to the burned gases close to the bluff body. However later in the cycle, as the shedded vortex propagates upward and merges with the main vortex, the flowfield adopts a character more similar to the case where there is only the main vortex present. This means that in the later stages of the cycle more of the gases from the upper reaches of the flame are convected down toward the bluff body by the main vortex in the inner recirculation zone. Since the gases from further above are cooler due to greater levels of air entrainment at greater heights, more cooling of the burned gases close to the bluff body occurs. It is also seen that there is a small region of significantly cooler gas local to the lip of the bluff body at a height of ~ 3 mm at a phase angle of 210^o in the CARS results. This is likely to be due to local flame extinction at various instances in the recording of the phase-averaged temperature. Flame extinction would allow cooler unburned gases to escape into the region of burned gases at this point in the flame. This behaviour would be consistent with the general lowering of

the burned gas temperature, where the flamefront becomes more difficult to stabilise, consequently leading to spasmodic flame extinction.

Further to the variation in overall temperature amongst the three phase angles, the difference in temperature between the hot regions of CARS and URANS is attributable to the adiabatic modelling assumptions of the latter. The hotter temperatures in the URANS case would result in more viscous burned gases (Linneken 1977). This contribution would account for the slowing of the propagation rate of the shedded vortex up the flamefront, as demonstrated by the relative heights of the vortical structures for the same phases between CARS and URANS, as proposed earlier in section 4.1.3.1. URANS also shows a marked difference in the gradient of the flamebrush in contrast to both CARS and OH PLIF. This effect could be due to the incorrect modelling of the flow pattern in the inner recirculation zone, and its effect on the position of the flamefront. The difference in gradients between experimental and modelling results can also be clearly seen in Armitage *et al.* (2006).

It is seen that there are positive temperature gradients in the vertical direction close to the bluff body burner surface for the three phase angles in Fig. 4.10. This is seen more clearly in Fig. 4.11 in which the plot shows the variation of CARS temperature with height on the axis of the burner. It is seen that there exists a positive temperature gradient close to the bluff body surface up to about 5 mm. The positive temperature gradient indicates the conduction of heat into the bluff body. This does not exist in the URANS case, as the model has an adiabatic boundary condition at the bluff body surface.

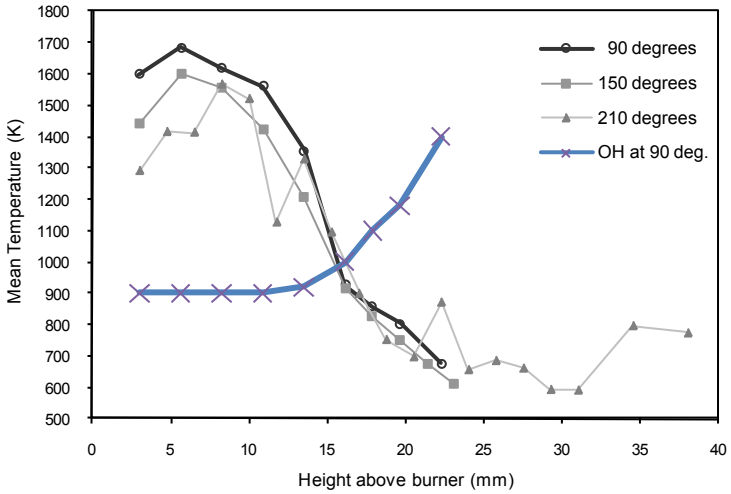

Figure 4.11: Phase-averaged temperatures along the centreline of the burner (*i.e.* radial position = 0 mm) from CARS and OH PLIF.

Comparison of temperature profiles between the different methods reveal that OH PLIF does not also correctly predict temperature gradients close to the bluff body surface, as shown in Fig. 4.11 for the phase angle 90°. Interestingly, the height change over which the temperature rises to its peak along the centreline is approximately 5 mm in the CARS results. This is to within the 10 mm estimate for the thermal boundary layer, δ_{th}, that was stated in section 4.1.3.2.

As discussed in section 4.1.3.2, the temperatures of the burned gases close to the bluff body as measured using OH PLIF seemed underestimated. The application of CARS clearly demonstrates this, where there is a maximum discrepancy of 800 K between the results for the phase angle 90°, as seen in

Fig. 4.11. The magnitude of the temperatures in the region together with the thickness of the thermal boundary layer make it clear that indeed conduction does occur, but not to the extent as portrayed by the large cool region in the OH PLIF results. Furthermore, the maximum temperature of the region of hot gases measured using CARS (*i.e.* 1691 K), as seen at the phase angle 90^{o}, also approaches the adiabatic flame temperature of 1706 K (Morley 1997) for the equivalence ratio of 0.55. This suggests that the amount of air entrainment into the flame at this stage in the cycle is negligible. Therefore, the removal of the quartz casing and consequent exposure of the flame to the surrounding atmosphere has been shown not to have a significant effect on the dynamics of the flame, especially at the earlier stages of the acoustic cycle.

The remaining regions of the flame to be considered are the apparently cooler ones as measured using CARS for heights above the burner in excess of 15 mm, as shown in Fig. 4.10. These regions exhibit a marked decrease in temperature from the hotter region of burned gases closer to the bluff body. This behaviour is unexpected and clearly deviates from the results of OH PLIF and URANS. The reason for the deviation is thought to be caused by the presence of the fluctuating flamefront in these regions. This is illustrated in Fig. 4.12 for the phase angle 150^{o}, where the tip of the flamebrush that has been rotated 180^{o} by the shedded vortex lies in the top half of the region of measured temperatures.

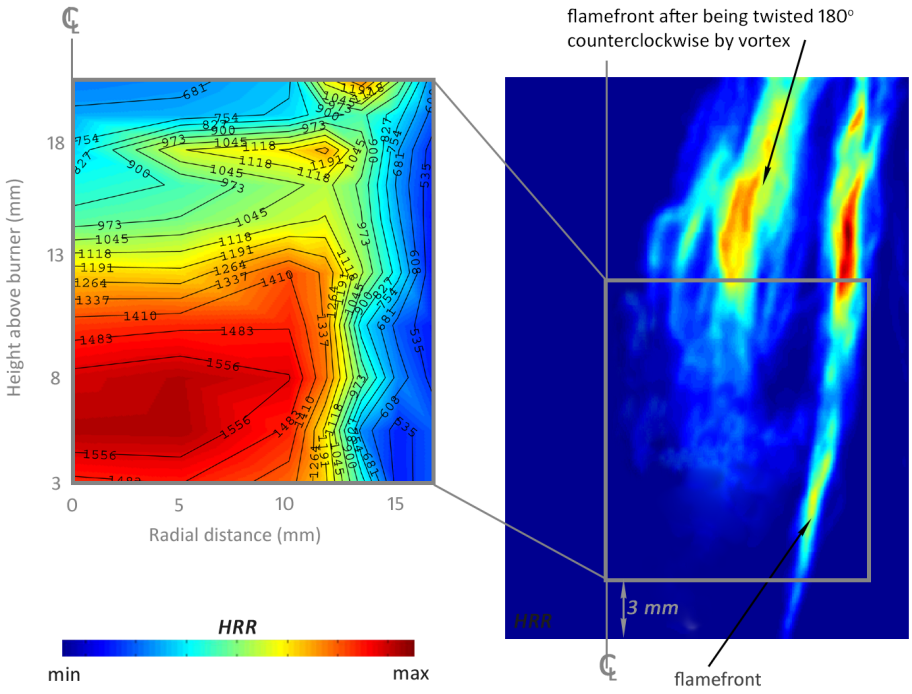

Figure 4.12: Comparison of HRR derived from Balachandran *et al.* (2005) to CARS temperature at a phase angle of 150° at the same flame conditions.

The implication of the fluctuation of the flamefront position in the upper regions of the burned gases is that it lowers the measured temperatures. This is the case since the spatial resolution is finite (length: 5 mm and diameter: 100 μm) and when the flamefront crosses the measurement volume a fraction of the unburned reactants is captured. This lowers the overall temperature of the measurement volume. However the contribution to the lowering of temperature is not proportional to the fraction of the unburned gases in the measurement volume. In fact, the measured temperature is very sensitive to

tiny quantities of cool gas in the measurement volume when using CARS. This point is elucidated further in section 4.3.2.

4.3.2 Validity of Temperatures

An important aspect of the CARS results in Fig. 4.11 is the standard deviation of temperature across all of the single measurements that constitute a phase-averaged value. The standard deviation serves to help one discriminate reliable temperatures. Figure 4.13 shows an example map of standard deviation for phase angle 90^{o}, which also shows the corresponding phase-averaged temperature map.

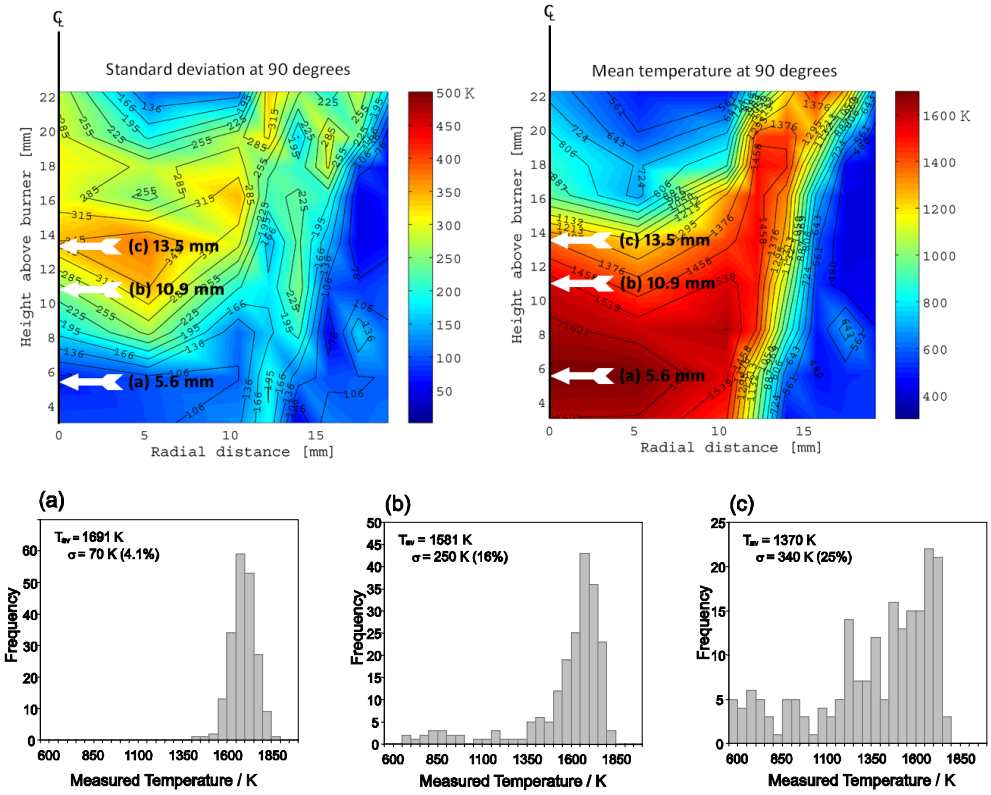

Figure 4.13: Standard deviation and phase-averaged temperature shown for a phase angle of 90° along with sample temperature histograms.

Here, it is seen that regions of relatively high standard deviation correspond to lower temperatures in contrast to the region of burned gases close to the bluff body with standard deviations to within ~100 K. The large values of standard deviation are thought to stem from the flickering of the flamefront from measurement shot-to-shot over the phase-average, as discussed earlier in relation to Fig. 4.12. Owing to the combination of a large temperature gradient present at the flamefront and the instability in its position, any series of temperature measurements taken close to the flamefront would show a

larger distribution of temperature. These measured temperatures do not necessarily represent accurately the phase-averaged temperature using the non-linear CARS technique.

CARS results show a much cooler region in the top left of the images, which is far from agreement with URANS and OH PLIF. The relatively cool region is considered to be an artefact due to the lack of spatial resolution in the CARS experiments. When the volume is too large it poses a problem when zones with temperature gradients are probed. This is particularly the case for probed position (c) in Fig. 4.13, whereupon the flamebrush curls round to this position. Figure 4.13 also shows histograms of temperature derived from instantaneous CARS spectra for points (a), (b) and (c) within the maps of Fig. 4.13, where it is clear that point (c) is not Gaussian unlike (a). The combination of low spatial resolution and the non-linear nature of CARS leads to a distorted histogram. This results from the combination of spectra from the pockets of cool and hot gases within the measurement volume, which yields a 'mixed' spectrum. Due to the squared relationship between CARS signal intensity and nitrogen density, cold spectral contributions significantly outweigh the weaker hot spectra. This leads to biasing towards cooler temperatures, and hence towards a larger spread in the distribution of temperatures and a negative skew from what would otherwise be a Gaussian distribution (Chen and Bilger 2002; Guo *et al*. 2003).

To resolve the problem of spatial resolution, attempts to correct for the biasing inherent in mixed CARS spectra have been investigated before (Boquillon *et al*. 1988; Shepherd *et al.* 1990; Thumann *et al.* 1995;

Parameswaran and Snelling 1996; Seeger *et al.* 2006). This involves taking the difference between the measured and true-averaged temperature within the CARS measurement volume. Figure 4.14 shows three plots of temperature of measurement volume versus proportion of hot and cold gas, at T_{max} and T_{min} respectively. For each pair of plots, the dashed and solid lines represent respectively the averaged- and CARS measured temperature.

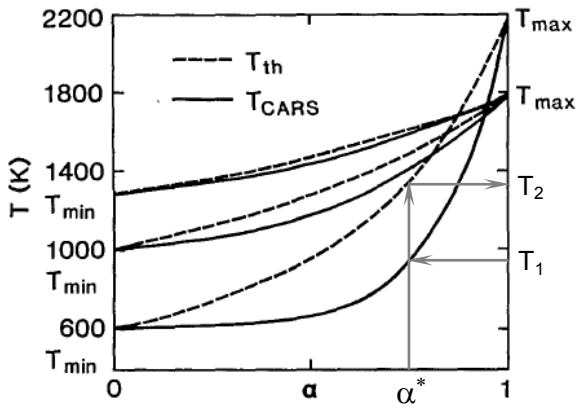

Figure 4.14: Thermodynamic temperature, T_{th}, and CARS temperature, T_{CARS}, versus α, the fraction of hot gas in the probe volume, for three pairs of high- and low-temperature values (adapted from Boquillon *et al.* 1988).

The averaged-temperature is computed from considering that the gases contained in the measurement volume are a homogeneous mixture of the hot and cold gases; this is known as the thermodynamic temperature, T_{th} (Boquillon *et al*. 1988). CARS measured temperatures are derived from the fitting of theoretical spectra for homogeneous samples to mixed spectra of varying proportions of hot gas, α; this yields the curve as shown by the solid lines. The mixed spectra can be derived theoretically by considering the signal contributions from the two pockets of hot and cold gas, at T_{min} and T_{max}, to the

overall signal. By fitting theoretical spectra for homogeneous samples to the theoretically derived mixed spectra for different compositions α, the solid-lined curves are generated, as shown in Fig. 4.14. This allows the correction to be made for the biasing present in the measured temperature towards the cold pockets in the measurement volume. The correction is made by inferring the temperature T_1 from the fit to an experimentally obtained mixed spectrum, then reading the corresponding hot gas proportion, α^*, on Fig. 4.14, thus allowing the real averaged-temperature to be read as T_2.

However, this method is not free from problems, which is attributable to the limited range of α values that can be used in correcting temperature. Due to the flat part of the curve for the CARS temperature (solid curve in Fig. 4.14), the precision in the corrected temperature, T_2 is significantly reduced by the very large sensitivity of the change of α to any imprecision in the measured temperature from the mixed spectra, T_1. The flatness of the curve for low values of α becomes more prominent with a lowering of the cold pocket temperature, $T_{min,}$ thus limiting the range over which temperatures can be corrected for α in excess of 0.5. Furthermore, the technique above relies on the division of the measurement volume into two distinct temperatures, T_{min} and T_{max}, which assumes that the flamefront sharply demarcates the two proportions in the measurement volume, usually at room and the adiabatic flame temperature. However, in reality a series of temperatures would exist within the measurement volume for turbulent flames. This further complicates the correction for biasing originating from the non-linearity of the CARS technique. Therefore, in light of the two aspects of this method, it was deemed

impractical to apply correction, and hence improve the resolution of the measured temperature at the flamefront.

4.4 Conclusion

In this study, broadband vibrational nitrogen CARS was employed to provide more accurate temperature measurements in the cross-section of an axisymmetrical turbulent bluff body premixed flame. The flame was acoustically-forced and emanated from a burner, whose design is a model of a real LPP combustor. CARS spectra were recorded at several points within the cross-section, where the phase-average temperature was measured. At each of the three phase angles throughout the acoustic cycle, phase-averaged temperature maps were generated by interpolating the grid of pointwise temperatures in the cross-section. It was found qualitatively that there were significant differences between our results and that of OH PLIF by Ayoola *et al.* (2009). The CARS results for the burned gas regions in the flame were discriminated against for reliable temperatures by comparing the corresponding maps with maps of standard deviation. The standard deviation of the phase-averaged temperatures served to reflect the level of accuracy of the results. The primary source of inaccuracy was due to the large bias towards cooler gases present in the measurement volume, which is an inherent limitation of CARS. Despite this drawback, it was shown that the inner region of the flame above the bluff body comprised of a relatively homogeneous composition from shot-to-shot with phase-averaged temperatures of a standard deviation at a minimum of ~4 % at 1691 K for phase angle 90^{o}. At this phase angle, this region was up to 47 % hotter using CARS in contrast to

the results of OH PLIF. This result is to be expected as this region would contain hot burned gases from the recirculation induced by the vortices emanating from the burner inlet. However, it was conceived initially that the cool regions in the results of OH PLIF are caused by the conduction of heat to the metallic bluff body, yet the proportion of heat conducted away has been shown to be implausible. The results here show that the gases in the central region are at a temperature closer to the adiabatic limit. It has also been confirmed that conduction of heat does occur, owing to the presence of a temperature gradient close to the bluff body surface. At a phase angle of 90^{o}, there are regions near the bluff body that exhibit temperatures close to the adiabatic limit of 1706 K for an equivalence ratio of 0.55. At this earlier stage in the acoustic cycle, it suggests that entrainment of air from the surrounding atmosphere into the incoming reactants is negligible in the absence of the quartz casing that had been used in previous studies of the same flame. The quartz casing in our experiments had to be removed so that CARS measurements were possible. This implies that the temperatures close to the bluff body, in the proximity of the peak temperature, are independent of the absence of the quartz casing, since the level of air entrainment is unaffected by its presence. Therefore, the CARS results for these regions, for at least the case of 90^{o}, are deemed sufficiently accurate and hence suitable for the purpose of validating newer and more advanced versions of URANS CFD code for the model burner.

Chapter 5

Thermometry of Low Pressure Sooting Flames Using Diode Laser Excited TLAF

In the previous two chapters, methods were developed to reanalyse previous combustion datasets. In this chapter, the development of a technique is presented for the measurement of accurate temperature in low pressure laminar sooting flames. Thus far, few experimental attempts have managed to measure temperature with sufficient accuracy in these environments. Here, we present for the first time the application of blue diode lasers in conjunction with indium Two Line Atomic Fluorescence (TLAF) to achieve this goal. The results presented here are deemed of quantitative utility and are being used in a model flame to study the chemical kinetics of soot formation. The chapter is organised as follows: the background behind the need to measure temperature accurately in sooting environments is outlined. A review of previous demonstrations of indium TLAF thermometry is given. The experimental setup is then described. Temperature profiles are presented, and the accuracy and precision are estimated.

5.1 Background

5.1.1 Motivation

This chapter reports on the development of a thermometric technique, which addresses the challenge of accurately measuring temperature in low pressure sooting flames. Temperature is a crucial variable to understanding and modelling the behaviour of such flames. The desire for more accurate temperatures is required for improved knowledge of the kinetics involved in soot formation (Haynes and Wagner 1981; Richter *et al*. 2000). Better determination of soot formation is important, because soot is a key element of many combustion systems. For example, soot plays an important role in radiative heat transfer in furnaces and boilers, where radiation from soot is typically the dominant heat transfer mode (Al Omari 2001). Furthermore, soot is used as a commercial product with applications including ink, tyres and plastics. Improvements can be made to the material properties of such applications by better predicting and controlling the structure and size distribution of soot particles (Haynes and Wagner 1981). Controlling such properties offers the possibility of decreasing the toxicity of undesired soot emission from combustion processes, for example. Toxicity is thought to stem from the size of the particles, and their tendency to adsorb polycyclic aromatic hydrocarbons (PAHs), both of which pose a carcinogenic health risk (Dockery *et al*. 1993; Allen *et al*. 1996; Durant *et al.* 1996).

In view of the above potential for improvements to be made to rich premixed combustion, an understanding of the mechanisms involved in soot formation is necessary. Numerous interdependent parameters are of fundamental

importance to soot; however, temperature remains one of the most significant in controlling the chemical reactions and physical processes that lead to soot formation (Haynes and Wagner 1981). Soot formation is a complex phenomenon, and so far computational models have been needed to predict soot compositions. These models are based on simple laminar test flames under carefully controlled conditions. The laminar flames are employed, so that they can be easily tested against reliable experimental data. Comparison to data for such flames is required, because of the need to validate the accuracy of the computational models. Experiments in sooting flames are best conducted under low pressure. This results in a thickened flamefront, which is advantageous in two ways. Theoretically, the shallower thermal gradients facilitate modelling of the flame, due to the reduced stiffness of the equations involved. Stiffness in this context is the difficulty to solve the governing differential equations using numerical methods, leading to numerical instability unless very small spatial step sizes are taken. Experimentally, thickened flamefronts also allow temperature to be spatially resolved more easily, owing to the shallower thermal gradients. Reliable measurements of temperature can thus be made, and is crucial here because the reaction rate is strongly governed by temperature. The use of good experimental data as input to numerical models is therefore important. With low thermal gradients, these test flames are therefore suited to the investigation of flame chemistry and to validate models.

5.1.2 Low Pressure Burner Study

One example where low pressure is particularly beneficial is the study of incipient soot formation in rich premixed flames. This process occurs close to the flamefront and involves the synthesis of precursors that lead to the formation of soot particles. Similar to the flamefront, the region of incipient soot formation further downstream is also enlarged and therefore easier to spatially resolve at low pressure. Although many studies on soot have been performed at higher pressures of 1 bar and above (Desgroux *et al.* 2008), little has been investigated at low pressure where the early stages of soot formation can be more easily resolved. This is largely a result of insufficient sensitivity of the laser techniques been available hitherto to detect quantities such as soot volume fraction and particle sizes in the relatively soot-free regions of the incipient zone. This is especially true for low pressure, where species concentrations are also correspondingly lower. Therefore to date, there is little experimentally derived knowledge and understanding of detailed mechanisms of incipient soot formation (Desgroux *et al.* 2008). In a recent study at the University of Lille, the combustion of methane has been investigated using Laser Induced Incandescence (LII) combined with Cavity Ring Down Spectroscopy (CRDS) on a low pressure burner. This combination allows sensitive detection of soot volume fraction, as reported by Desgroux *et al.* (2008). In their study, methane was chosen as a fuel owing to its widespread and important role in domestic and industrial combustion. In this work, it is intended to complement the dataset of Desgroux *et al.* (2008) with accurate temperature measurements using the same low pressure burner and conditions, as part of a concerted effort toward understanding incipient soot formation in methane oxidation. The data would serve as input to numerical

models under development at the University of Lille, in order to further insight into incipient soot formation. It is noteworthy that the temperatures to be used as input to the models should be measured as accurately as possible. This is because the composition of sooting flames is sensitively dependent on temperature. For example, a 5 % deviation in temperature results in an approximate 50 % change in soot volume fraction for an atmospheric laminar premixed ethylene/air flame with an equivalence ratio of 2.16 (Böhm *et al.* 1988; Blanquart and Pitsch 2009). This highlights the point that accurate and precise thermometry is necessary in sooting flames. However, sooting flames still present a challenge in thermometry and there is a continued demand for new thermometric methods that can measure temperature accurately in such environments; this is discussed in the following section.

5.1.3 Challenges of Sooting Thermometry

Laser-based techniques have provided instantaneous, non-intrusive, temporally and spatially resolved measurements of many parameters of interest, such as temperature. Experimentally determined temperature in flames containing soot, using laser-based techniques, has thus far proven to be problematic (Hartlieb *et al.* 2000). Parasitic absorption, scatter, and other interferences due to the presence of soot and PAHs prevent reliable temperatures from being measured using many common laser techniques. These issues restrict the application of such diagnostics to idealised clean flames, thus excluding many flames of practical interest. It is therefore apparent that there is a need for alternative thermometric techniques to complement those already in common use. The alternative diagnostic of

TLAF is presented as one of the current best methods of measuring temperature in sooting environments. In the following, a brief review is given of the limitations of standard thermometric approaches in light of the challenges of sooting flames (see chapter 1 for description of principles), then the hitherto demonstrations of TLAF in sooting flames are critically reviewed.

5.1.3.1 Review of Thermometric Techniques

Rayleigh scattering (with typical cross sections of $\sim 10^{-27}$ cm^2/sr) is a conventional technique for the measurement of temperature in combustion. It results from elastic scattering of light from all molecules and provides a measure of the total number density, permitting temperature to be deduced through the ideal gas law (Banwell and McCash 1994). This technique offers excellent temporal and spatial resolution capabilities but is limited by the requirement for constant Rayleigh cross-sections in unburned and burned gases. Such flames have been investigated (Wang *et al.* 2005; Wang and Barlow 2008), whereby the composition was chosen to ensure a constant Rayleigh cross-section throughout the flames. A further limitation of Rayleigh scattering measurements is the need for very clean and particle-free conditions, as the elastic nature of the process is highly susceptible to interference from Mie scattering (Eckbreth 1996). This restricted the locations where temperature could be measured to the tip of the non-premixed flame in the work of (Wang *et al.* 2005; Wang and Barlow 2008). To overcome the problem of Mie scattering and parasitic reflections, Filtered Rayleigh scattering can be used. Here, a notch filter is used in the signal collection to absorb the spectral line that results from Mie scattering (Hoffman *et al.* 1996).

The filter is narrow, so that the remaining broadened Rayleigh signal can be used to infer temperature. Although the Filtered technique overcomes the problem of Mie scattering, it doesn't circumvent the need for knowing Rayleigh cross-sections.

To prevent the problem of Mie scattering, Raman-based thermometry can be used. For example, spontaneous Raman spectroscopy involves inelastic scattering of molecules in the sample, which are either scattered to a lower or higher energy level referred to as anti-Stokes and Stokes scattering respectively. This results in a spectrum from which the temperature can be derived. However, Raman spectroscopy suffers from low signal strength, and especially in low pressure environments where the number density is correspondingly lower. Typical vibrational Raman cross-sections are about 100 times smaller than that of Rayleigh scattering (cross sections of $\sim 10^{-29}$ cm^2/sr). The signal strength also varies with $\sim 1/\lambda^4$, and thus low wavelengths are preferred. Higher signal strengths, and hence low wavelengths towards the UV range, are needed especially at low pressure conditions. Interference from the many fluorescence emitters at the UV range present a problem, and polarisation discrimination needs to be used. This filters the Raman signal from the other emissions, however it reduces the signal strength. Such interference still results in accuracies of ~6 % in low pressure flames (Hartlieb *et al.* 2000).

The alternative Raman-based technique, Coherent anti-Stokes Raman Scattering (CARS), involves the overlap of three laser beams of different wavelength, in which a species (*e.g.* nitrogen) is excited resulting in emission

of a coherent beam. This beam is the signal and can be easily discriminated against background, and therefore is better suited to luminous and particle-laden flows. Although CARS is a powerful technique, it suffers from characteristic limitations. For example, in low pressure environments, CARS is not viable due to the sensitivity of the signal to pressure and hence the number density of molecules. This is because the CARS signal is quadratically dependent on the number density, and hence the signal decreases sharply with pressure. Another characteristic problem of CARS is the accompanying signal that occurs as a result of non-resonant processes. This results in a background contribution to the CARS spectra and if large enough can reduce the sensitivity of the temperature measurements. In rich sooting flames there exist a sizeable proportion of large hydrocarbon intermediates, in which each possesses a strong non-resonant contribution. Furthermore, if nitrogen is used as the probe molecule its fractional concentration can be low enough in some sooting flames to allow the non-resonant contributions dominate the CARS spectra. In the flames studied here, the nitrogen concentration is lower than what would otherwise be if air were used as the oxidant. The nitrogen concentration had to be reduced, in order to maintain stability of the laminar flame (Desgroux *et al.* 2008). However, non-resonant background can be reduced using polarisation suppression. This method unfortunately reduces the signal strength by a factor of 16 (Eckbreth 1996), and in combination with low pressure conditions would lead to a very weak signal. In addition to the above, the experimental complexity, and the expense of the equipment needed restricts the generic application of CARS.

Alternatively, the best set of techniques are the numerous laser-induced fluorescence (LIF) strategies that exist for thermometry. LIF-based techniques can either use naturally occurring- or seeded-species. The fluorescence is typically quite strong (with typical cross sections of ~10^{-16} cm^2/sr), making LIF better suited to two-dimensional imaging than other techniques. The frequency shift associated with the fluorescence process is also advantageous for reducing interference, especially in comparison to Rayleigh scattering. The use of species naturally present in the flame for LIF thermometry is limited because of relatively low concentrations of many potential species (*e.g*. OH, CN, and CH) and the narrow regions within the flame in which many of the species exist (Warnatz *et al*. 1996). Of the naturally occurring species within a flame, the OH radical is one of the most commonly used for LIF (Cattolica 1981; Seitzman *et al.* 1994; Qin *et al.* 2005). In non-premixed flames, OH only exists over a small range of temperatures and mixture fractions, and so is not well suited for general measurements (Nygren *et al.* 2001). Furthermore, with relevance to this study, in fuel-rich premixed flames the OH concentration is low so that it is poorly suited to thermometric measurements in the presence of soot (Eckbreth 1996). It is accepted that the detectivity limit of OH concentration is ~10^{14} cm^{-3}, in order to perform OH LIF thermometry (Eckbreth 1996; Davis *et al*. 2000; Hartlieb *et al.* 2000). For premixed methane/air flames, equivalence ratios exceeding 1.2 possess OH concentrations less than the limit of 10^{14} cm^{-3} (Kychakoff *et al.* 1984; Musick *et al.* 1996), thus rendering OH LIF unsuitable for rich methane flames as investigated in this work with equivalence ratios more than 2.05. Required knowledge of quenching cross-sections is also a drawback of OH LIF, and

restricts the accuracy of temperature measurements to the order of 5 % (Hartlieb *et al.* 2000).

5.1.3.2 The Two-Line Fluorescence Approach

An improvement to the LIF approach is to employ the two-line method, which often involves exciting a species within the flame from two closely spaced energy levels to a common upper level. The spacing of the lower levels is selected by maximising the sensitivity of the measurement, which is derived from the sensitivity of the relative population of the lower levels to temperature. The technique is performed by irradiating the species with two different wavelengths, and the ratio of resulting fluorescence intensities is used to compute the temperature of the flame (Zizak *et al.* 1984). The underlying advantage of the two-line approach results from the independence of the temperature measurement from electronic quenching if excitation from the lower levels is to a common upper state. One such example is the use of NO (Tamura *et al.* 1998; Atakan and Hartlieb 2000; Bessler and Schulz 2004; Kronemayer *et al.* 2007) as a temperature marker, which yields reliable temperatures under certain conditions. Two-line NO LIF is susceptible to background interferences due to the wavelengths of the fluorescence (around 226 nm) and the associated overlap with O_2, PAH and LII emission (Hayashida *et al.* 2005). The latter two pose a significant problem in sooting flames where PAHs are in higher concentrations and laser induced incandescence (LII) is more likely to occur in the presence of soot. Systematic deviations of 12% have been found in temperature measurements by Bessler *et al.* (2001) attributable to background interference in sooting flames. Fuel-

rich flames are also more challenging to measure temperature using NO-LIF due to the increased consumption of NO in reburn reactions, thus leading to a loss in signal for sooting flames (Atakan and Hartlieb 2000).

For the investigation of low pressure sooting flames in this study NO LIF is unfavourable, and a metrologically more robust thermometric technique was developed instead. The technique here used seeded indium in conjunction with the TLAF scheme. Indium TLAF offers the advantage of evading spectral coincidences, as the emission wavelength is located around 451 nm in the blue range, which is spectrally far away from other background emission naturally present in flames. Such emission occurs due to the presence of naturally occuring excited radicals: C_2 and CH, with emission at 473 and 432 nm respectively. The use of indium also circumvents the problem of NO consumption from reburn reactions within fuel-rich flames. In spite of indium's finite level of reactivity with oxygen that is present within fuel/air flames to form InOH (Th and Alkemade 1972), the consumption of indium through the flame diminishes with an increase in equivalence ratio, thus leading to increased signal levels for richer flames.

Despite the advantages of using indium TLAF for sooting flames, there have only been three relevant studies of sooting flames using indium TLAF in the recent literature (Engström *et al.* 2000; Nygren *et al.* 2001; Medwell *et al.* 2009). However, the resulting temperatures have been qualitative, and have not demonstrated potential for applications that require high accuracy. Accuracy is needed to study soot formation sensitive to temperature. The three studies have shown that they all have a precision ranging from 5-10 %.

This would be a limitation if these TLAF setups were to be used for measuring temperature in turbulent flames. However, precision is unimportant when one considers the suitability of these setups for steady laminar sooting flames used here. This is because in steady flames measurements can be repeated to obtain an average, and hence a more reliable estimate of temperature. Accuracy here is more important, to yield quantitative data on the process of soot formation. The three techniques all require calibration using another thermometric method. This places a limit on the accuracy of indium TLAF, as governed by the method of calibration. For example, Medwell *et al.* (2009) implements indium TLAF in the non-linear regime (abbreviated as NTLAF) using high laser irradiances. A thermocouple is used for the calibration to determine the unknown parameters in the NTLAF equation. Owing to the tendency of thermocouples to accumulate soot, the calibration could only be taken in the non-sooting regions of the rich sooting flames. However, the parameters of the NTLAF equation are quenching dependent. The quenching coefficients are composition dependent, and hence vary throughout the flame. It is therefore unclear from the work of Medwell *et al.* (2009) whether their calibration remains valid for measurements taken in very sooting regions of such flames. However, the work of Engström *et al.* (2000) and Nygren *et al.* (2001) is based on linear TLAF of indium, which is independent of quenching effects. Although the calibration problem associated with NTLAF is eliminated, there is less signal and hence the precision is reduced. As mentioned above, precision is not crucial for the laminar flame study here. Accuracy is of concern, and the work of Engström *et al.* (2000) and Nygren *et al.* (2001) suffered from a potential source of systematic error. They implemented indium TLAF by measuring fluorescence

consecutively for each signal at 410 and 451 nm. This involved recording the signal firstly at 410 nm over 50 repetitions, and then the same was done for the 451 nm signal. This results in a lack of correspondence between the 410 and 451 signals recorded. This is a problem for TLAF, as it is a ratiometric technique and implicitly relies on the temporal correspondence of the signals at the two wavelengths. This is always true in turbulent flames where there are fluctuations in temperature and seeding. However, changes in seeding can occur in laminar flames if the seeding is not carefully controlled. As they admit, there were large times between the signal collections for there to be possible drifts in the seeding concentration. The ratio of the averaged signals can then be subject to systematic error.

5.1.4 Aims

The aim of this work is to employ a novel thermometric method that allows accurate temperatures to be recorded in sooting flames. The technique is applied to laminar low pressure sooting flames to demonstrate and provide useful data for quantitative studies of flame chemistry at the University of Lille. Our method is more cost-effective than previous implementations, which used bulky Nd:YAG and dye laser systems. Here, we use extended cavity diode lasers (ECDLs) to scan across the absorption lines in seeded indium in the flame near 410 and 451 nm (Hult *et al.* 2005). This method allows for calibration-free temperature measurements. Instead of the consecutive recording of fluorescence performed by Engström *et al.* (2000) and Nygren *et al.* (2001), we alternate between the detection of 410 and 451 nm fluorescence by using a beam chopper. This eliminates potential problems

with systematic error through drifts in seeding. For quantitative studies of flame chemistry, we report temperatures in a laminar sooting flame with estimates of systematic error.

5.2 Experimental Method

5.2.1 The Burner

Temperature measurements were performed in a laminar flat flame with a reactant mixture of CH_4, O_2 and N_2, stabilised on a McKenna burner, as shown in Fig. 5.1. The burner was water-cooled and had a diameter of 63 mm over which small holes were uniformly distributed. The volumetric flowrate of the premixed gases to the burner was fixed at 4.85 standard dm^3/min. The gas flowrates were regulated by mass flow controllers (TYLAN FC260). A nitrogen co-flow was also used to ensure that the flame remained stable during the experiments. The set of flame conditions studied is summarised in Table 5.1, and is consistent with the parameters used in the quantitative studies by the research group of P. Desgroux at the University of Lille. The flame was enclosed in a sealed burner chamber, as shown in Fig. 5.1. The internal pressure of the chamber was maintained below atmospheric pressure with the use of a vacuum pump and motorised regulation valve that maintained the pressure constant to within ±0.5 Torr (66.6 Pa). This control was essential with regards to the large sensitivity of soot formation with pressure, as discussed later in section 5.3.2. The burner comprised of two quartz windows at opposite sides, through which the laser beams passed. Perpendicular to the direction of laser beam propagation, there was another window, which was used to collect the signal. It was possible to translate the

burner head vertically relative to the chamber using a screw gauge. This allowed the measurement volume to be accurately positioned in relation to the burner surface.

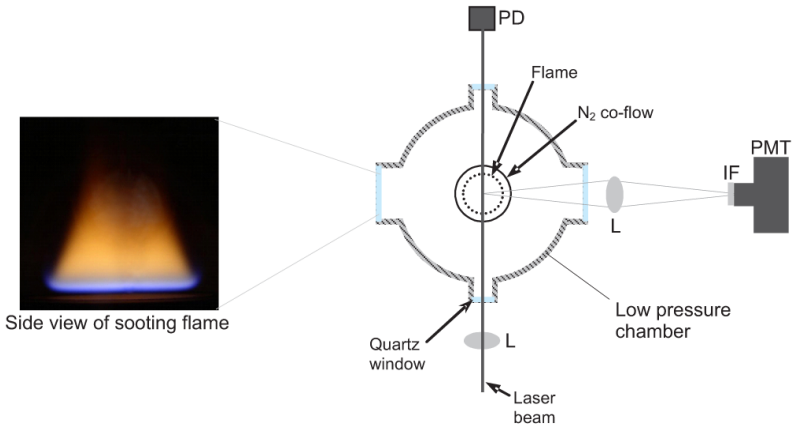

Figure 5.1: Photograph of the flame and schematic of the top view of the low pressure burner setup. Components comprise: photodiode (PD), lenses (L), photomultiplier tube (PMT) complete with interference filter (IF). The overall setup is shown in Fig. 5.2.

	ϕ	P / kPa	Mole Fractions		
			CH_4	O_2	N_2
Flame A	2.05	26.7	0.434	0.425	0.14
Flame B	2.32	26.7	0.46	0.40	0.14
Flame C	2.32	21.3	0.46	0.40	0.14
Flame D	2.32	18.7	0.46	0.40	0.14

Table 5.1: List of parameters for the four flame types studied.

The flames were seeded by passing nitrogen through a nebuliser containing an aqueous solution of indium chloride ($InCl_3$) of concentration 0.03 M. The entrained $InCl_3$ particles in the premixed gases were volatised on the approach to the flamefront, where neutral indium atoms are formed from the sublimation of the particles (Th and Alkemade 1972). This allowed the neutral indium atoms to be electronically excited upon irradiation with the laser beams used in the TLAF technique employed here. The flowrate of nitrogen through the nebuliser and the concentration of the solution were adjusted to give a level of indium seeding that was low enough to yield negligible fractional absorption of the incident laser beam (< 3 %); this potential source of error is discussed further in section 5.3.3. In order to check whether the introduction of indium would perturb the flame, the level of seeding was varied and the temperature measured using the TLAF technique (see section 5.2.2 below). It was found that there was no difference in measured temperature upon an increase from 0.03 to 0.06 M nebuliser solution after accounting for laser beam absorption through the flame. This confirms that the presence of indium had little effect on the flame chemistry at these concentrations. The same check was also performed for different flowrates of gas passing through the nebuliser. A larger flowrate results in increased levels of water vapour being introduced into the flame. It was found that the flowrate of nitrogen through the nebuliser used in these experiments introduced a 2 % mole fraction of water into the premixed gases. At these seeding conditions, it was found that there was insignificant perturbation to the flame.

5.2.2 The Laser System

The setup for the diode laser induced fluorescence temperature measurements is shown in Fig. 5.2. The schematic shows the two ECDLs, whose continuous outputs are modulated by a rotary chopper. The laser beams are then monitored by two photodiodes, one of which uses an etalon to monitor the spectral quality of the laser output. The main beam is then focussed onto the center of the flame, whose fluoresence is focussed onto a PMT. Details of each aspect of the setup are given below.

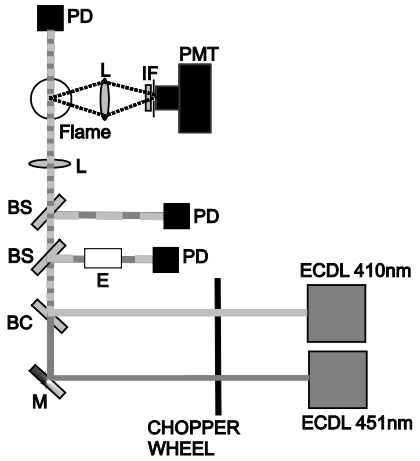

Figure 5.2: Components of the setup comprise: photodiodes (PD), lenses (L), photomultiplier tube (PMT) complete with interference filter (IF), beam samplers (BS), beam combiners (BC), mirror (M), etalon (E) and the two ECDLs.

The two ECDLs shown in Fig. 5.2 were operated in scanning mode where the input powers were ramped. For ECDLs, the power is linearly related to the output wavelength. The green trace in Fig. 5.3 shows the variation of output

power, and hence wavelength, as a function of time. A rotary chopper was employed to modulate the laser beams, whose output gave alternate bursts of light from each laser at a rate of 10 Hz. The power tuning (and hence wavelength tuning) of the lasers was synchronised with the chopping, so that spectra from the two lasers could be acquired interchangeably. An example of the raw data is shown in Fig. 5.3 in which the traces are averages over 50 wavelength scans.

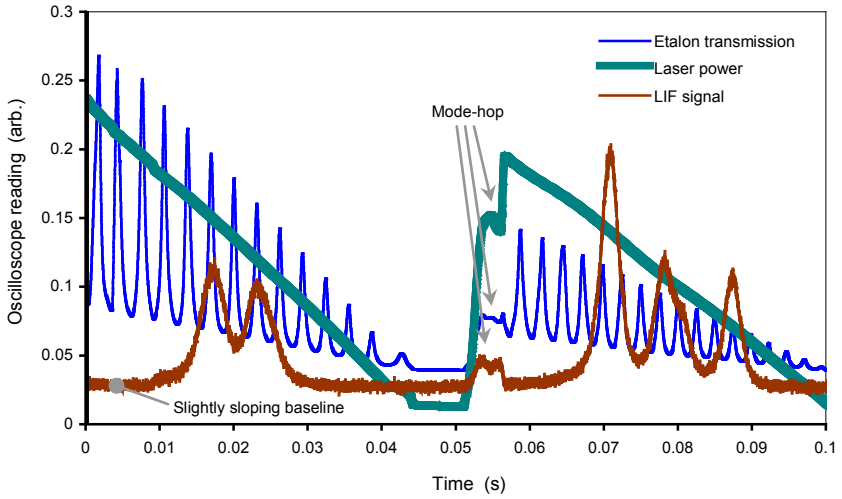

Figure 5.3: Raw data showing an average of 50 traces from the oscilloscope. The signals in the left-half of the figure were generated by the 451 nm laser. As it reaches the end of its wavelength scan, it is blocked by the chopper. Then the 410 nm laser is transmitted instead, generating the signals seen in the right-half of the figure.

The wavelength scans of the two lasers were monitored using a solid quartz etalon (free spectral range of 3.1 GHz) and a photodiode. The resulting etalon trace seen in Fig. 5.3 allowed the identification of mode-hops during the wavelength scan. An example mode-hop is shown in the raw data trace. Mode-hopping is an undesired phenomenon and occurs when the standing

wave nodes in the laser cavity changes abruptly. The presence of mode-hops would be easily shown by any discontinuities in the etalon trace. In the example here, it can be seen in all three traces. Fine adjustments to the piezo settings of the mounts in the ECDLs were made to obtain the widest mode-hop free window within the scans, such that the resulting indium spectra would be free of discontinuities. Furthermore, the spacing of the peaks in the etalon trace allows the time axis to be scaled to wavelength; this can be done with the knowledge of the FSR, and is necessary for the integration of the spectra in the wavelength domain for computing temperature. The green trace in Fig. 5.3 shows the variation of the laser beam power as monitored by another photodiode, which was referenced using a calibrated laser power meter. The referencing was performed by placing a black-body thermopile meter in front of the focussing lens after an experiment and then relating the voltage recorded by the photodiode with the power reading from the meter.

The main beams were overlapped and focussed to a diameter of 100 μm onto the burner's central axis. The focal region was imaged orthogonally with an *f*-number of 6 through an interference filter (λ_c= 451.1 nm; $\Delta\lambda$ = 3 nm) onto a 500 μm pinhole with a magnification of one. Using 2*f* imaging, this yielded a vertical spatial resolution of 100 μm. The resulting fluorescence was captured by a PMT and was recorded onto an oscilloscope with the corresponding red trace shown in Fig. 5.3. To improve the signal-to-noise ratio of the recorded spectra, the spectra were time-averaged over 50 scans. This approach is only possible in our case of measuring temperature in a steady laminar flame. In order to compute temperature from the averaged spectra, the background was subtracted from all traces. The corrected fluorescence traces were then

divided by the corrected laser power. The resulting normalised experimental spectra were then fitted to theoretical spectra that gave the best fit. The theoretical spectra were derived from the summation of the constituent Voigt profiles of the hyperfine lines. These theoretical spectra were integrated with respect to the horizontal wavelength scale, which had been calibrated using the etalon trace. The integration is a necessary step as the result is used in the TLAF formula (see derivation in chapter 2) shown by the denominator of Eqn. 5.1:

$$T = \frac{\Delta E / k}{\ln\left(\frac{\int_0^\infty F_a / I_{02}\, d\nu}{\int_0^\infty F_b / I_{12}\, d\nu}\right) + 3\ln\left(\frac{\lambda_{21}}{\lambda_{20}}\right) + \ln\left(\frac{A_{21}}{A_{20}}\right)} \tag{5.1}$$

An in-depth description of the scanning technique has already been given by Hult *et al.* (2005), however, the technique used here has been developed further to reduce inaccuracy caused by slow drifts in the seeded indium concentration of the nebuliser. This effect can lead to biasing in temperatures, where the level of seeding slowly increases with time. This is attributable to a gradual increase in the concentration of the nebuliser contents owing to the evaporation of water from the solution inside. During one series, the drift in concentration occurs before recording the other series, thus introducing biasing. The biasing results from a lack of correspondence between the intensity of the 410 and 451 spectra. In this work, the problem was overcome by using an optical chopper, which allowed for the alternate recording of the

410 and 451 spectra, which reduces the time for significant drift to occur between the two corresponding spectra. This involves recording a 410 nm spectrum, then that for 451 nm. This is repeated at the scanning rate of 10 Hz. For one measurement 50 scans were made, where each scan consists of a 410 and 451 spectrum. Over the 50 scans, the 410 and 451 nm spectra were averaged; the averaged spectra were then used to calculate the temperature.

In addition to these improvements to the experimental procedure necessary to obtain temperature data of quantitative utility, there are also particular issues related to the implementation of TLAF in sooting flames. A calibration-free TLAF approach has previously been described in which a single photomultiplier is used to detect at 451 nm (Hult *et al*. 2005). This eliminates the influence on the signal ratio of separate filter transmission curves and detector sensitivities. The calibration of relative detector sensitivities usually introduces the largest source of systematic error (Hult *et al*. 2005). Since it involves resonance fluorescence for the 451 nm transition, we speculated that this approach may not work well in sooting flames due to the effects of Mie scattering from the soot particles. It can be seen in Fig. 5.3, however, that the Mie scattering (slightly sloping baseline) is weak compared to the signal intensity. It was therefore possible to perform the measurements reported here using a single-detector, thus simplifying the experimental setup and permitting accurate temperature data to be obtained without the need for calibration. Potential error from Mie scattering from soot is discussed in section 5.3.3.

5.3 Results and Discussion

In this section, example spectra are shown for the low pressure conditions of the flames studied here alongside example spectra from previous studies at atmospheric pressure. The temperatures that were calculated from the low pressure spectra, corresponding to the conditions of the burner described above, are presented for flames at three different pressures and two fuel equivalence ratios. The physical basis for the results are also discussed.

5.3.1 Indium Spectra

Figure 5.4 exhibits two sample fluorescence spectra for indium that were excited near 410 nm at two different pressures at a temperature of 1600 K. The plots show an overlay of the theoretical spectrum on the experimental result, showing a good agreement between the two. This is highlighted by the small residual values in the subplots (*i.e.* difference between theoretical and experimental data). The Voigt profile had been used, which takes into account simultaneously the effect of Doppler- and pressure-broadening. Both effects are significant in most circumstances, especially at atmospheric pressure, therefore warranting the use of the Voigt profile. The quality of the spectral fits at both low- and atmospheric-pressures, shown by Fig. 5.4, confirms the suitability of the Voigt profile in the theoretical fit.

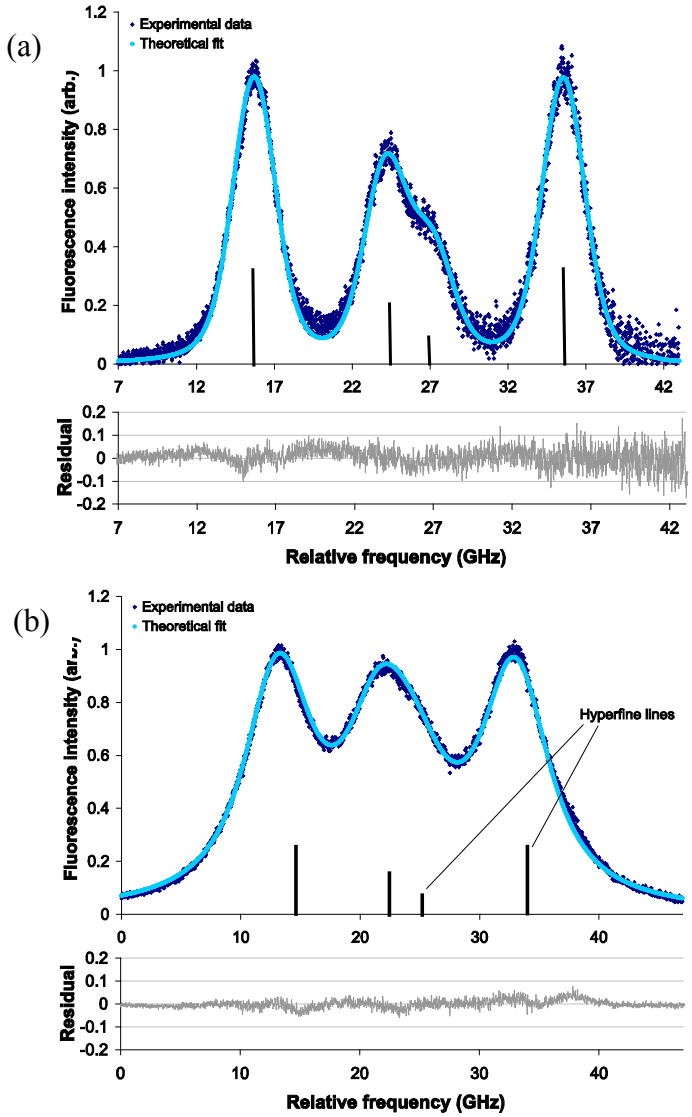

Figure 5.4: Example spectra shown for the 410 nm transition in indium for (a) a flame at 26.7 kPa and (b) 1 atm for a temperature of 1600 K.

It can be seen for the low pressure case that there are prominent peaks. These are due to the underlying hyperfine components, as shown in Fig. 5.4. The middle two peaks are seen to overlap, however they become indistinguishable at higher pressure. This is demonstrated by comparing Figs. 5.4 (a) with (b). Raising the pressure also increases the overlap between all the other hyperfine components, leading to a highly broadened composite spectrum, as shown in Fig. 5.4 (b). It is also seen that the overall Full Width at Half Maximum (FWHM) of the entire spectrum increases with pressure, where in Fig. 5.4 the FWHM is 28 GHz at 101.3 kPa (atmospheric pressure) and 22 GHz at 26.7 kPa (low pressure).

5.3.2 Temperature Profiles

From the indium spectra the temperature can be computed. Temperature was measured along the vertical central axis of the steady, laminar flame at several points. Figure 5.5 shows the height scan for flames A and B (see Table 5.1) at two different equivalence ratios under identical pressures. The smoothness of the temperature profiles demonstrate the excellent precision that is made possible by the use of a rotary chopper and averaging over 50 spectra (see section 5.3.3 for an account of precision). Nevertheless, the smoothness of the profile does not indicate levels of accuracy within the temperature values. An account of potential sources of systematic error is also treated in section 5.3.3.

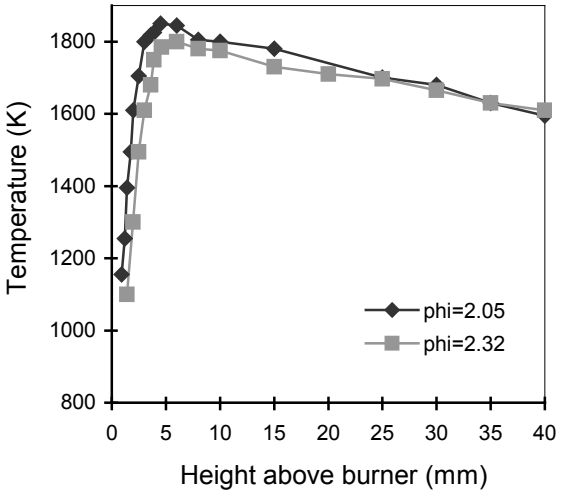

Figure 5.5: Temperature profiles for flames A and B at different values of equivalence ratio at a fixed pressure of 26.7 kPa.

The profiles above clearly show a consistent drop in temperature with height in the burned gases. There is an approximate drop of 200 K over a height change of 30 mm in the burned gases for both cases. This is markedly different to the case of stoichiometric premixed laminar flames where there can be very little change in temperature over 30 mm, and even a slight increase in temperature in the burnt gases after the reaction zone (Chen and Mansour 1996) due to the oxidation of CO. The temperature decrease in our flames is attributable to low pressure and the sooting conditions. Low pressure increases the thermal diffusivity, α, according to: $\alpha \propto 1/P$, and hence increases the rate of thermal diffusion to the surroundings. This increases the rate of heat loss in the burned gases, and hence the temperature decreases at a faster rate with height from the burner. The presence of soot in the burned gases also contributes to the increased cooling of the gases, owing

to the thermal radiation from the soot particles to the surroundings. With the trends in the temperature of the burned gases and the abovementioned thermal effects, the results seem to be qualitatively accurate. Furthermore, the temperatures of the above flames are plausible with respect to the adiabatic flame temperature of the two flames of 2400 K and 2150 K at equivalence ratios of 2.05 and 2.32 respectively (Kee *et al*. 1985). These values are in excess of the peak temperatures in each of the height profiles. Again, this is expected, due to the appreciable heat loss caused by the low pressure and sooting conditions.

It is also clear that the temperatures for the richer flame are lower, as shown by the vertical offset of the profile relative to the leaner flame in Fig. 5.5. This is expected due to the larger deviation of the richer flame from stoichiometry. A larger soot loading in richer flames further contributes to the cooling of the flame. Additionally, a horizontal offset exists between the two temperature profiles in Fig. 5.5. This is due to the richer flame adopting a position that is higher relative to the burner's surface. It is believed that this is caused by the lower flame speed of the richer flame in conjunction with the diverging flow pattern of the unburned gases. The divergent flow pattern is caused by the expansion of the unburned gases upon entering the low pressure combustion chamber. Since the flow pattern is divergent, the local gas speed decreases with an increase in height. The increase in height of the flamefront is therefore due to the adoption of a new equilibrium between the lower flame speed and the corresponding lower unburned gas speed. The offset can also be confirmed by the acquisition of OH LIF data within the same flames. This is shown by the OH LIF profiles of the flame in Fig. 5.6. The data were

generated by using a tuneable dye laser by I.S. Burns during the same experimental campaign. The 1 mm offset of the OH profiles are consistent with that of the temperature profiles in Fig. 5.5. This provides further evidence in support of the validity of the temperature profiles.

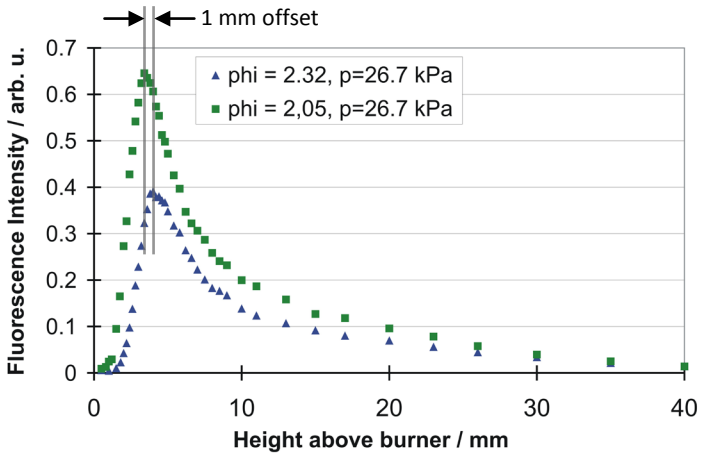

Figure 5.6: Profiles of OH LIF in flames A and B of Fig. 5.5. (adapted from I.S. Burns)

Temperature measurements were also made in the richer flame (ϕ = 2.32) at three different pressures; the profiles are shown in Fig. 5.7.

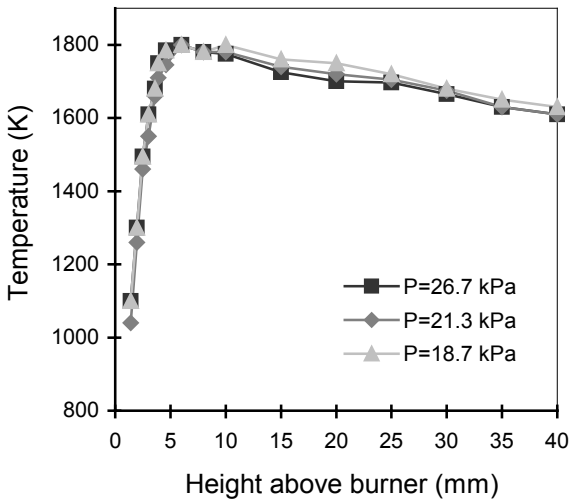

Figure 5.7: Temperature profiles for flames B, C and D at different values of pressure at a fixed equivalence ratio of 2.32.

For the pressures investigated, it appears that there is hardly any change in the temperature profiles. This apparent independence of temperature is surprising in spite of the variation in soot concentration for the range of pressures studied. The soot concentration had been investigated previously using Laser Induced Incandescence (LII) calibrated with Cavity Ring-Down Spectroscopy (CRDS) (Desgroux *et al.* 2008). They observed that an increase in pressure from 21.3 to 26.7 kPa induces an order of magnitude increase in soot volume fraction. In spite of this massive increase, there is no observable change in temperature between the two pressures. This suggests that the surprisingly strong dependence of soot volume fraction on pressure does not appear to be

mediated by an effect of pressure on the flame temperature at the conditions studied here.

5.3.3 Potential Sources of Error

Thus far, we have demonstrated the use of indium TLAF in low pressure sooting flames and have shown qualitatively that the fidelity of the measured temperatures is superior in light of the expected trends and smoothness of the temperature profiles. However, a treatment of the accuracy for the laminar flames investigated here is necessary to determine whether indium TLAF can provide useful data for quantitative studies (*e.g.* validation of flame-chemistry models, as in this study of a low pressure burner). Two main sources of systematic error have been identified. One of which is the black-body thermopile powermeter used to calibrate the laser power recorded on the photodiodes. The powermeter could introduce a percentage error in temperature of up to 1.7 % at 1850 K. This error is conservative and is based on the full range of zero-error of the meter based on the smallest division of the reading; see appendix C for details. The other main error source is the potential for misalignment of the two laser beams. The worse case scenario is where the beams would be misaligned in the vertical direction, in which the temperature gradient is greatest. It was estimated that this could introduce an error of up to ~1 % with a misalignment of 20 μm; see appendix C. This potential for systematic error is greatest at the steep flank of the temperature gradient, however for the burned gases it dramatically drops to about ~0.1 %, where the error from the powermeter would then dominate.

Other sources of systematic error were considered and discovered to be of minor importance, for example, Mie scattering from the soot particles. This occurs as a result of detecting resonance fluorescence at 451 nm, where there is a susceptibility to detecting scattered radiation from the 451 nm laser. An upper estimate for the systematic error in these experiments due to scattering is ~ 0.3 %. This is based on the most fuel-rich flame at a measurement point with the greatest soot volume fraction, x_{soot} = 1 ppbv (Desgroux *et al.* 2008). This corresponds to flame B at a pressure of 26.7 kPa, ϕ = 2.32, a measurement point of 40 mm above the burner with a temperature of 1630 K; see appendix C for details. Furthermore, potential error can originate from absorption of the laser beam. As the beam propagates through the seeded flame, the beam power is increasingly attenuated. This would introduce error when normalising the signal by the laser power recorded by the photodiode placed upstream of the measurement volume. To overcome this problem, a photodiode was placed after the flame, as shown in Fig. 5.2, so that the level of beam attenuation could be quantified. Due to the axisymmetry of the flame, the absorbance of the beam at the measurement volume is half of the value across the entire flame. This allows the signal to be normalised by the correct incident laser power at the measurement volume. However, in our experiments the difference between the temperatures with and without this correction is small at ~ 0.2 % at 1800 K with a peak absorption of up to 3 %. With this level of attenuation at 3 %, it is therefore possible to neglect the correction for absorption. This is beneficial when measuring temperature in flames that are not axisymmetric or are fluctuating in time, where the laser power at the measurement volume cannot be deduced. On top of the estimates of systematic error been made thus far, a typical standard error exists at ~ 0.2

%. This uncertainty in the sample-average temperatures over 50 samples is based on a precision of 1.4 % (standard deviation).

5.4 Conclusions

In this study for the first time, temperature measurements with excellent accuracy and precision have been conducted within low pressure sooting flames without recourse to calibration. This was performed by employing extended cavity diode lasers in combination with two-line atomic fluorescence of indium. The indium was seeded into the flames, and the wavelength output of the ECDLs was scanned in time. The resulting spectra were integrated to compute time-averaged temperature at points within the laminar sooting flame. This method of measuring temperature using ECDLs has been exploited recently in stoichiometric flames, however it has not been applied to the difficult problem of sooting flame thermometry. Furthermore, the method was refined in the way the data was collected to overcome the problem of seeding-drift, which can introduce bias. It had also been demonstrated that the use of one photomultiplier detector could be used successfully without being susceptible to soot induced Mie scattering. This offered the opportunity to improve the accuracy of the temperatures without the need to calibrate against another temperature standard. The accuracy achieved was better than ~ 2 % with a precision of 1.4 %, which is a significant achievement for sooting thermometry. Both the high precision and accuracy of the technique allowed for the deduction that the temperature in the flames studied here is independent of the pressure at a fixed equivalence ratio. In light of the improved measurement potential of this setup, as

demonstrated by the fidelity of the data in the demonstration here, this thermometric technique promises to contribute to the understanding of soot kinetics. This will lead to better insight into soot formation and destruction within the flame, leading to improved knowledge of soot particle size distributions. This would hence lead to improved control of emission from sooting combustion in a wide range of current applications.

Chapter 6

High Repetition Rate Thermometry Using Diode Laser Excited TLAF

This chapter describes the first demonstration of diode lasers for Laser Induced Fluorescence (LIF) measurements of temperature in flames at kHz repetition rates. The technique has potential for quasi-continuous temperature measurements to be performed in turbulent flames, and which is of great value for the validation of computational codes such as Large Eddy Simulations (LES). Thus far, there have been few demonstrations of quasi-continuous temporally and spatially resolved temperature measurements in flames. Here, we employ diode lasers to excite Two-Line Atomic Fluorescence (TLAF) in indium seeded to flames at trace level concentrations. The lasers are locked to specific excitation wavelengths and the light is modulated by a chopper wheel at kHz rates. This chapter is organised as follows. Firstly, the need is outlined for high repetition rate temperature measurements in flames. Then, a review of previous attempts of high speed thermometry is given. The principles and the experimental setup of the technique developed here are then described. The results are then presented to

demonstrate the reproducibility and precision of measurements and their capability to resolve dynamic features in flames.

6.1 Background

6.1.1 Motivation

The motivation for this work is based on the importance of improving the current understanding of dynamic combustion phenomena. Key variables, such as flame temperature, strongly govern combustion stability, pollutant formation *etc*. and form essential input for predictive computational codes. Such codes of practical importance in combustion include LES, which directly simulates the large eddies by integrating the governing conservation equations. However, small scale turbulence is modelled using "subgrid scale models". This means that the integral length scales are resolved, whilst the Batchelor and Kolmogorov scales are modelled (Veynante and Vervisch 2002). Such sub-models need to be validated, and this can either be done by testing with data from Direct Numerical Simulations (DNS) *a priori* or by comparing the output of the LES with experimental data *a posteriori* (Böhm *et al.* 2008). The usual first choice is to use DNS to validate sub-models, however this is not possible at high turbulence intensity, because of the high computational cost involved using DNS under these conditions. The alternative is to validate LES with experimental data, and this is an approach commonly used for the study of highly turbulent flames such as gas turbine, and direct injection internal combustion engines (Mastorakos *et al.* 2009). Under such conditions, transient phenomena such as flame extinction and reignition occur frequently; these effects are highly sensitive to the history of

the flowfield (Lyons 2007; Böhm *et al.* 2009; Mastorakos *et al.* 2009). Owing to the short duration of these events (time scales typically below 5 ms), it is important to be able to temporally resolve them, so that LES can be validated properly (Böhm *et al.* 2008). This requires high speed measurements, capable of acquisition rates in the kHz range. Such measurements are made possible by advancements in laser and camera technology, for example, diode-pumped solid state lasers and improved CMOS cameras. They have been used for the study of temporal evolution of mixture fractions by LIF (Dreizler *et al.* 2000; Gordon *et al.* 2009), flowfield vorticity and strain using Particle Imaging Velocimetry (PIV) (Upatnieks *et al.* 2002; Hult *et al.* 2004; Böhm *et al.* 2009), and temperature measurements *via.* Rayleigh scattering (Wang *et al.* 2005; Wang and Barlow 2008). All of these contribute to creating comprehensive experimental databases for flames where highly transient phenomena occur. In this study, we focus on temperature as a variable in combustion. Temperature is one of the few parameters, which continues to be difficult to resolve on spatial and temporal scales characteristic of unstable combustion phenomena. Temperature is difficult to measure with good spatial and temporal resolution, yet it is critical in the assessment of flame dynamics. For example according to Lyons, (2007), measurement of strain rate is insufficient to characterise extinction for unsteady flow conditions, thus temperature data would also serve to complement other variables measured at kHz rates. The next section reviews what techniques exist to perform high speed thermometry.

6.1.2 Review of Fast Thermometry

Recently, high speed temperature measurements have been implemented at kHz rates with efforts focussed on Tunable Diode Laser Absorption Spectroscopy (TDLAS) (Meyer *et al.* 2005; Zhou *et al.* 2005). Owing to the path integrated nature of TDLAS, it cannot provide spatially resolved measurements. This therefore renders it impractical for turbulent flames where spatial resolution is a prerequisite for such thermometry. On the other hand, numerous point- and planar-measurement techniques have been implemented previously to spatially resolve combustion temperature (Eckbreth 1996; Kohse-Hoinghaus *et al.* 2005); however, the majority of these techniques have been limited to measurements at a single instance in time (*i.e.* a rapid measurement at a slow repetition rate). Although some of these techniques are capable of favourable spatial and temporal resolution, they are generally restricted to a repetition rate not much faster than 10 Hz. A recent notable exception is the report of high repetition rate thermometry using Rayleigh scattering (Wang *et al*. 2005; Wang and Barlow 2008). This technique offers excellent temporal and spatial resolution capabilities but is limited by the requirement for constant Rayleigh cross-sections in unburned and burned gases, if recourse to simultaneous Raman based composition measurements is not necessary. Rayleigh scattering is also applicable only in clean and soot-free flames, and requires expensive high power lasers.

Nevertheless, attempts to spatially resolve temperature at high speed were done more than 20 years ago. Of these, measurements at up to 250 Hz were demonstrated in heated air using LIF of O_2 (Lee *et al.* 1987), and LIF of OH in flames (Kychakoff *et al.* 1987). Clearly these example demonstrations were

a first step toward quasi-continuous thermometry but were not sufficiently fast for turbulent flames where typical Batchelor timescales correspond to 2 – 20 kHz (Wang *et al.* 2005). Quicker measurements were also performed at 3 kHz by Chang *et al.* (1990) by rapid wavelength scanning of an Ar^+ ion pumped dye laser for OH LIF. The precision of the temperatures was 14 % at 1130 K and the technique is dependent on knowledge of quenching coefficients, which are not always known with sufficient accuracy. A simple, yet highly accurate, alternative for measuring flame temperature at a point (Joklik and Daily 1982), or across a plane (Engström *et al.* 2000), is by use of TLAF (Zizak *et al.* 1984). TLAF is attractive since it offers independence from quenching, when the two transitions probed have a common upper state (Daily 1997). So far, most TLAF measurements have been performed at low repetition rates of the order of 10 Hz. One exception to this is an early demonstration by Dec and Keller, (1986) who used continuous-wave dye lasers pumped by high powered Ar^+ ion lasers for indium excitation at up to 10 kHz repetition rates. Such lasers can deliver sufficient power at rates approaching 10 kHz to yield temperature measurements of 3 % precision at 2000 K (Dec and Keller, 1986), however they are very bulky and expensive systems compared to diode lasers. Large laser powers of 40 mW were used to excite indium near 451 nm, which is up to 80 times larger than that obtained from diode lasers used in this work (Chrystie *et al.* 2009). Despite the large powers used by Dec and Keller, an appreciable uncertainty persists, reaching 3 % at 2000 K for measurement rates of 10 kHz. This could be due to the fact that the dye laser implemented by Dec and Keller, (1986) was multimode and would contribute to the imprecision by random mode shifting of the output in frequency space. Although Dec and Keller, (1986) have demonstrated good

temporal resolution capability at up to 10 kHz, which is in excess of typical Batchelor timescales (Wang *et al.* 2005), spatial resolution could be improved. Their spatial resolution was defined by an 800 μm slit, which is in excess of typical Batchelor lengthscales of 200 – 500 μm (Wang *et al.* 2005). Furthermore, their technique required calibration against a reference temperature measurement, and this limits the accuracy of the measurements to the method used for calibration.

6.1.3 Aims

The purpose of the work here is to develop a thermometric technique that permits accurate temperatures to be recorded at kHz acquisition rates. The technique is applied to a test flame, which is stabilised on an acoustically-excited Bunsen burner. The flame allows the reproducibility of the technique to be demonstrated, in addition to the capability of resolving dynamic flame features. Our technique is more cost-effective than previous implementations, which used bulky dye laser systems. Here, we use ECDLs and lock wavelengths to indium transitions near 410 and 451 nm. We demonstrate that ECDL-excited TLAF can be used to yield highly accurate and precise temperature data at repetition rates reaching up to 20 kHz. The technique's good spatial resolution (defined by a 150 μm long cylinder and an elliptical cross-section of 55 μm height and 95 μm width) and the low cost compared to alternative technologies offer potential for widespread use. We attribute the good performance of the technique to the high spectral purity of the ECDLs used (line of width less than 8 MHz) and the stable output intensity of the devices, which we achieve through a simple method of locking the laser line

to a reference wavelength (Burns 2006). This eliminates problems caused by laser mode noise on temperature measurements, which affected previous measurements (Dec and Keller 1986). Furthermore, our technique eliminates calibration errors, since it does not require a calibration against a reference temperature measurement. In addition to the merits of the proposed technique, its limitations are also carefully considered.

6.2 Principles of Fast TLAF

In the following sections an overview of the principles of fast TLAF is given. This provides the basis for the experimental setup in this work, which is described in section 6.3.

6.2.1 ECDL Output

In chapter 5, we described the technique of scanning TLAF. This involved relatively slow scanning across indium excitation spectra. This technique of generating spectra for the purpose of computing temperature is inherently slow, and was limited to 10 Hz in our case due to the use of ECDLs with mechanically moving parts. However, to generate quasi-continuous temperature data that corresponds to kHz rates, the scanning approach is not a viable option. The solution is to lock the wavelength output of the two ECDLs and modulate their output with the aid of a rotary chopper. This results in a sequence of alternating laser power output from both ECDLs, as denoted by the red trace in Fig. 6.1.

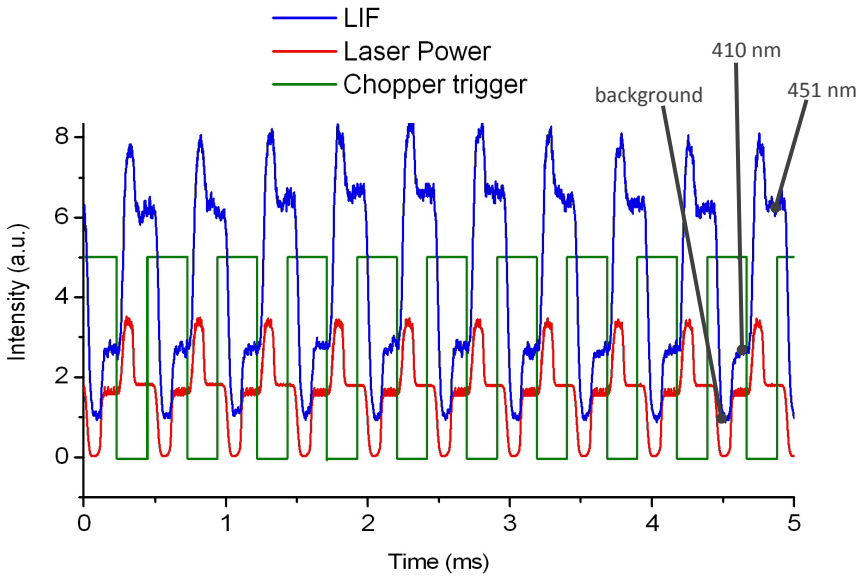

Figure 6.1: Example trace of fluorescence and laser power measured at 2 kHz, as recorded on an oscilloscope.

This results in alternating fluorescence, as shown by the blue trace, which originates from the modulated laser beams. The intensity of the alternating fluorescence levels depends on the wavelengths chosen for locking the ECDLs. Ideally, the output should be locked at a wavelength that will deliver the maximum fluorescence intensity from the seeded species to obtain an optimal signal to noise level. As for the work described in chapter 5, indium was used as the seeded species for the fast TLAF here. The corresponding locking positions for good fluorescence levels are illustrated on the indium spectra shown in Figs. 6.2 (a) and (b).

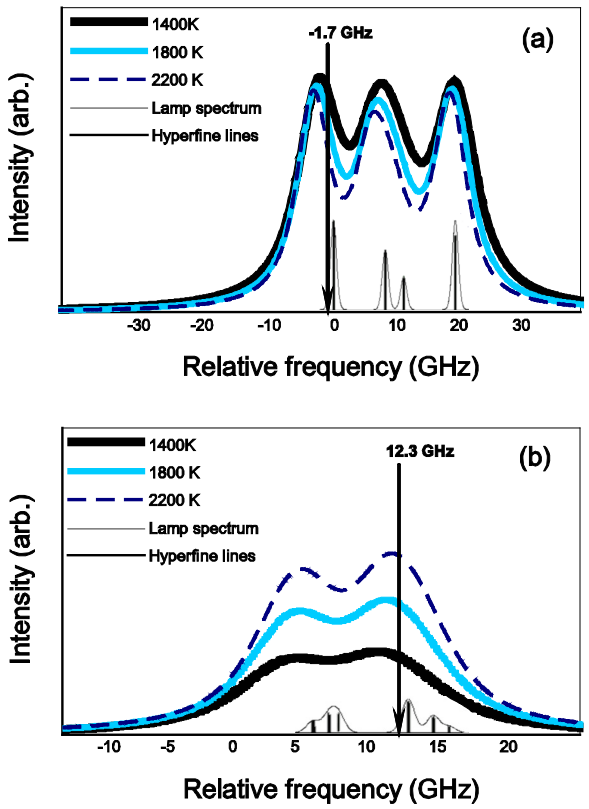

Figure 6.2: Coloured lines represent indium spectra for excitation near 410 nm (a) and 451 nm (b) at various temperatures. Verticals denote locking positions of -1.7 GHz for (a), and 12.3 GHz for (b) on a relative frequency scale. The underlying peaks represent hollow cathode lamp spectra.

As Fig. 6.2 shows, the ECDLs are locked at wavelengths that correspond to the intense parts of the indium spectra. However, the fine positioning of the locking location is determined by practical constraints. We aim to lock the laser line to a position on the steep flank of one of the hyperfine lines of the reference hollow cathode lamp – details of this method are given later in section 6.3. Figure 6.2 also illustrates the sensitivity of the TLAF technique to

the flame temperature, as shown by the three distinct heights of the indium spectra at 451 nm. This sensitivity originates from the close energy spacing of the two lower energy levels $5^2P_{1/2}$ and $5^2P_{3/2}$ in indium, where the more energetic of the two (*i.e.* $5^2P_{3/2}$) becomes more populated with an increase in temperature. The increase in the number of indium atoms of the state $5^2P_{3/2}$ equates to more indium atoms being available for excitation at 451 nm, hence resulting in more intense fluorescence at 451 nm excitation.

6.2.2 Spectral Calibration

Once the wavelength locking positions are chosen, a spectral calibration needs to be performed before temperature can be computed from the ratio of the signals. Previously, when scanning TLAF was implemented, as described in chapter 5, the ratio of the integrated spectra *f(T)* from the TLAF equation, was used to compute temperature. However, in the case of fast TLAF the ratio of the fluorescences, *R(T),* at the two locked wavelengths are the only available data. It is therefore necessary to relate this ratio to the ratio of integrated spectra, *f(T),* in order to compute the temperature. This can be done by modelling the indium spectra for both 410 and 451 nm. Modelling involves taking into account the pressure and Doppler broadening of the indium lines, in addition to the pressure-induced shift of their centrelines. By modelling the indium spectra, the ratio of the normalised fluorescence level to the integrated value at the locked wavelength can be calculated. The modelled ratios for both wavelengths are expressed in Eqn. set 6.1.

$$a(T,\nu_{451}) = \frac{(F_a/I_{12})|_{\nu_{451}}}{\int_0^\infty (F_a/I_{12})\,d\nu} \qquad b(T,\nu_{410}) = \frac{(F_b/I_{02})|_{\nu_{410}}}{\int_0^\infty (F_b/I_{02})\,d\nu} \tag{6.1}$$

Here, F_a and F_b are the signals that result from excitation at 451 and 410 nm respectively. The energy levels 0 and 2 correspond to the 410 nm excitation and levels 1 and 2 to 451 nm excitation. Taking the ratio of *a* and *b*, as expressed in Eqn. 6.2, yields two quantities; these include *R(T)* on the numerator, and *f(T)* on the denominator.

$$\frac{a}{b} = \frac{(F_a/I_{12})|_{\nu_{451}} \Big/ (F_b/I_{02})|_{\nu_{410}}}{\int_0^\infty (F_a/I_{12})\,d\nu \Big/ \int_0^\infty (F_b/I_{02})\,d\nu} = \frac{R(T)}{f(T)} \tag{6.2}$$

This then allows the frequency locked ratio, *R(T),* to be computed theoretically by modelling the ratio *a/b* as a function of temperature at the given locked wavelengths, in addition to the function of temperature, *f(T),* originating from the TLAF equation. Rearrangement of Eqn. 6.2 leads to Eqn. 6.3.

$$R(T) = \left(\frac{a}{b}\right) f(T) \tag{6.3}$$

The ratio, *R(T)*, can be computed for a range of temperatures at the locked wavelengths. This is shown for $1200 < T < 2200$ K in Fig. 6.3. The theoretically derived plot then allows temperature to be computed from

experimentally derived values of *R(T)*, without recourse to calibration to a reference temperature measurement.

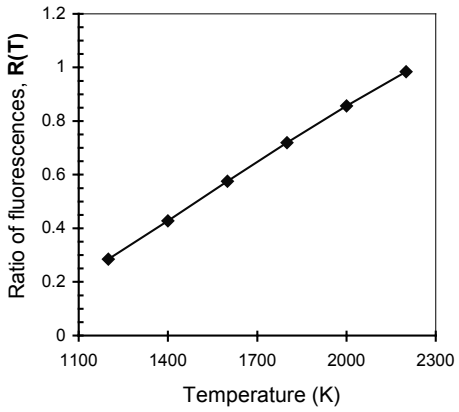

Figure 6.3: The plot shows the relationship between measured temperature and the ratio of normalised fluorescence from the 451 nm laser to that of the 410 nm laser, expressed as: $R(T) = (F_a/I_{451}) / (F_b/I_{410})$ for the locking positions (shown in Fig. 6.2) on the indium spectra.

6.3 Experimental Method

In this work the indium that was used as a temperature marker was excited *via.* the $5^2P_{1/2}$ - $6^2S_{1/2}$ transition near 410 nm, where the filtered fluorescence signal from the $5^2P_{3/2}$ - $6^2S_{1/2}$ transition is recorded near 451 nm on a photomultiplier tube (PMT, see Fig. 6.4). Subsequently, a second laser excites the $5^2P_{3/2}$ - $6^2S_{1/2}$ transition and resonance fluorescence is detected near 451 nm on the same PMT. Two custom designed ECDLs, whose design is fully described by Hult *et al.* (2005), were used to excite the indium transitions in the linear regime, with output powers of approximately 17 Wcm^{-2} (410 nm) and 8 Wcm^{-2} (451 nm) at the measurement volume.

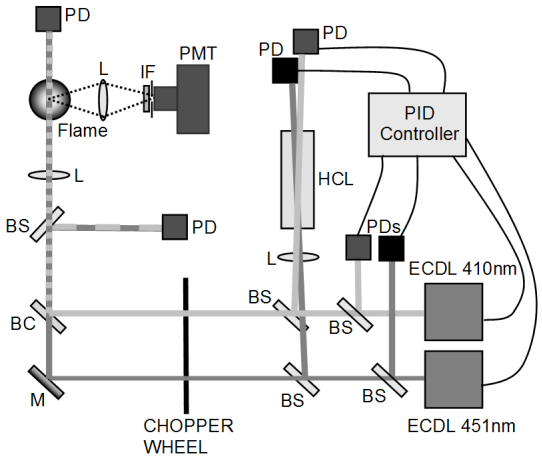

Figure 6.4: Components of the setup comprise a photodiode (PD), lens (L), photomultiplier (PMT) complete with interference filter (IF), beam splitter (BS), beam combiner (BC), mirror (M), hollow cathode lamp (HCL) and the two ECDLs.

To lock the wavelengths of the lasers near to the peaks of the indium transitions, weak reflections of the beams were directed through an indium hollow cathode lamp (HCL). The reference and transmitted powers were digitised (National Instruments PCI-6014), and a LabView program was used to lock the wavelength to the flank of one of the lamp lines by feedback control. Figures 6.2 (a) and (b) show the wavelength positions for the two lasers, which were chosen to balance precision in temperature on the one hand and sensitive PID control on the other. The latter was achieved by wavelength locking to a position near the maximum slope of the HCL spectral lineshapes. This establishes the greatest sensitivity for PID control, such that drifts in the ECDL output could be kept to a tight minimum. The monitored absorbance was maintained to a tight tolerance within 2 %. Once the lasers were locked, a

rotary chopper was used to switch rapidly between them; the rates of modulation (*i.e.* measurement speed) used in this study ranged from 500 Hz to 20 kHz. A weak reflection of the beam was diverted onto a photodiode, which was calibrated using a thermopile powermeter (Melles Griot 13PEM001) allowing the laser power in the measurement volume to be calculated. The modulated beams were focussed by a 300 mm lens onto the axis of the flame and the indium fluorescence was imaged at right angles at $f_{\#} = 2.4$ onto a 150 μm pinhole situated in front of a filtered ($\Delta\lambda = 3$ nm) photomultiplier tube (Hamamatsu, R3788). The signal was preamplified before being recorded on a four-channel oscilloscope (Tektronix TDS5034B). Laser powers before and after the flame were simultaneously recorded, in order to compute the absorbance through the flame.

In an effort to ensure sensible temperatures were being computed from the fast TLAF technique described here, initial experiments were performed in a well characterised laminar flat flame to validate the technique. This was done by employing a flat flame burner (Hartung *et al.* 2006), whose reactant inflow was seeded with indium. As described in chapter 5, the seeding of the reactants with $InCl_3$ was performed using a nebuliser assembly containing aqueous $InCl_3$. The $InCl_3$ particles seeded to the reactants volatise near the flamefront, where neutral indium atoms are formed. Fast TLAF measurements were made within these laminar flames, whose temperatures can be compared to the temperatures recorded from the scanning TLAF technique for the same flame. It was found that there was an equivalence in temperatures derived from both the fast- and scanning-TLAF methods, demonstrating that the setup, in addition to the spectral calibration, was correctly configured.

The steady laminar flat flame was also used to characterise the precision of the fast TLAF technique set up here. The composition of the reactants was fixed to that of the acoustically-forced Bunsen flame, whose details are described later. This is so that the measurement precision associated with the Bunsen flame can be characterised using the steady laminar test flame under the same inlet composition. Hence, the equivalence ratio was fixed to 1.1, and the level of seeding was fixed such that 12 % peak absorbance near 410 nm occurred. This absorbance level would correspond to 3 % in the Bunsen flame, in order to achieve the same level of fluorescence. Four times the absorbance is required, since the beam path is also four times longer than the Bunsen flame. A 3 % absorbance in the Bunsen flame was chosen since it provides a compromise between sufficient signal, and the introduction of systematic error to the measured temperature. The systematic error, caused by the absorbance of the laser beam, is introduced through the normalisation of the fluorescence by the incident laser power. By maintaining a low absorbance, the fluorescence can be normalised by the incident laser beam power instead of the actual power at the measurement volume without significant biasing. We found that maintaining an absorbance of less 3% did not introduce more than 1 % error in a temperature range of 1700 – 2100 K. The biasing introduced by the 12 % absorbance in the laminar flame could however be corrected for, since the flame is steady and whose geometry is known. This therefore allows the correct temperature to be calculated in the test flame, and hence the precision. To achieve these absorbances in both the flat flame burner (described above) and the acoustically-forced Bunsen burner (described below), an aqueous $InCl_3$ solution of 0.03 M was used.

During the initial experiments using the flat flame burner, the rate of modulation (measurement speed) between the two lasers was varied to investigate any influence on the precision of the resulting temperature measurements. For each modulation frequency the relative temperature uncertainty was recorded at a range of heights above the flamefront of the laminar flat flame. The uncertainty here is defined as the standard deviation of measured temperatures divided by the mean, obtained from 100 repetitions in the laminar steady flame. It was found that relative uncertainty decreases with an increase in measurement height, as can be seen in Fig. 6.5.

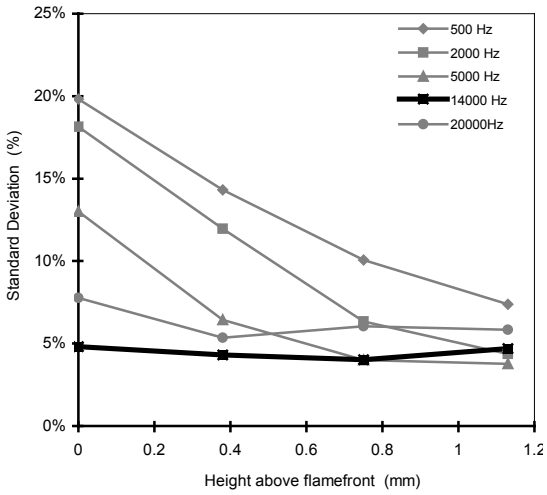

Figure 6.5: Plots of percentage uncertainty in measured temperature as a function of height above the flamefront for different rates of laser beam modulation.

Interestingly, the largest uncertainties near the flamefront are observed with slower measurement speeds, with relative errors increasing nearly 4-fold when decreasing measurement speeds from 14 kHz to 500 Hz at the flamefront. We attribute this finding to fluctuations in indium concentrations,

which are caused by the seeding process. If the time between the sequential detection of fluorescence originating from 410 and 451 nm laser excitation is too long, the indium concentration in the measurement volume may change resulting in a signal ratio that does not correspond to the correct temperature. We believe that these fluctuations in concentration are a consequence of the arrival of discrete solid particles of $InCl_3$ at the flamefront, causing atomic indium to be liberated in discontinuous bursts (Alkemade 1972). With increasing height these concentration differences even out, whilst the role of shot noise increases with modulation frequency. There is thus an optimal measurement speed (around 14 kHz) for the flame and setup employed in the present case, at which the uncertainty in temperature is at a minimum, which is evident in Fig. 6.5.

The repetition rate of 14 kHz for measuring temperature is in excess of turbulent flame timescales for some flames, which can possess Batchelor frequencies towards the lower end of the range: 2 – 20 kHz (Wang *et al*. 2005). The option of downsampling the 14 kHz temperature dataset, improves the precision of the temperature measurement. This is best shown by Fig. 6.6, where the 14 kHz dataset is downsampled to 3.5 kHz. Here, it can be seen that downsampling improves the measurement precision from 5 % (as already shown in Fig. 6.5) to 1.5 % at a mean temperature of ~2000 K. The use of a lower effective measurement rate of 3.5 kHz permits more precise measurements to be made for flames with lower Batchelor frequencies. As an example, the range of frequencies in a benchmark laboratory-scale non-premixed jet flame ("DLR_A", Re = 15,200 (Wang *et al.* 2005)) is 3 – 12 kHz depending on the distance from the jet nozzle. At the upper reaches of the

flame, the Batchelor frequencies are close to 3 kHz. This therefore gives an indication of the temporal resolutions that are needed for quasi-continuous thermometry.

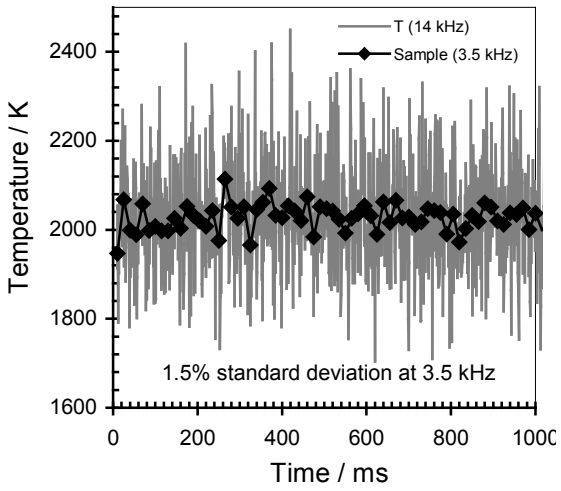

Figure 6.6: Trace of measured temperature at 14 kHz over a 1 second period in the steady laminar flat flame. Downsampling the 14 kHz data to 3.5 kHz yields a standard deviation of 1.5 % at a mean temperature of ~2000 K close to the flamefront.

To demonstrate the capability of fast TLAF to resolve dynamic flame features, measurements were conducted in an acoustically-forced Bunsen flame, similar to the flame described by Frank and Settersten, (2005). Reactants were premixed, with an equivalence ratio of 1.1, and passed through a tube of 10 mm diameter. Pressure perturbations were imposed on the flow by means of a loudspeaker situated 1 m upstream of the burner exit. An air co-flow was used to shield the flame from atmospheric perturbations. To further demonstrate the precision of the fast TLAF technique under

transient conditions, temperature measurements were made in the acoustically-forced Bunsen burner with regular periodicity. Experiments involving the sinusoidal-forcing of the reactant flow at a frequency of 114 Hz were performed. This frequency was chosen as it corresponded to one of the resonances of the burner tube, thus yielding an appreciable amplitude in the forced gases. This was necessary in order to obtain enough of an amplitude within the flame pulsation.

In order to check for reproducibility in the temperature measurements of the regularly forced flame, the amplitude was kept sufficiently low such that the flame would always be within the laminar regime. It could be identified by inspection whether the forced flame were turbulent from its sound. As soon as the flame became turbulent, as could be seen by eye, the flame emitted a rasping sound. This phenomenon is attributable to mini pressure-waves emanating from the fluctuation of the flamefront in space due to the turbulent flow field (Doroshenko and Furletov 1969). Nevertheless, to thoroughly check whether the flame was laminar throughout the entire cycle of the acoustic forcing, indium chemiluminescence images at 451 nm were taken using a triggered high resolution ICCD camera (Lavision Nanostar). This required the PMT to be replaced by the camera in the experimental configuration. The chemiluminescence images were phase-averaged, in which a number of images were taken at fixed phase angles over the acoustic cycle. This allowed mean chemiluminescence to be determined for a particular phase angle, and is referred to here as ‘phase-averaged’. The phase-averaged images were then compared to single-shot images. It was found that there was

little difference between them, owing to the overlap of the laminar flamefronts at each phase in the cycle.

As part of the demonstration to test how well fast TLAF can resolve dynamic flame features, measurements were conducted within pulsed flames on the Bunsen burner. The flame was pulsed by using a speaker that was driven with an all-positive saw-tooth wave with a two-second period and a 100 % duty cycle. This is long enough for perturbations to die-out before the next pulse. The resultant flame structure was visualised by imaging chemiluminescence at various points through the cycle using the triggered ICCD camera. Temperature measurements were made in the pulsed flame, in an effort to reveal the rapid dynamics caused by the steep edge of the saw-tooth and to demonstrate the temporal resolution capability. This was done by using the PMT (*i.e.* in the setup shown in Fig. 6.4), in order to capture instantaneous temperature transients within the pulsed flame.

The fast TLAF setup shown in Fig. 6.4 was modified slightly to accommodate the ICCD camera for performing one-dimensional (1-D) temperature measurements within the pulsed Bunsen flame. The procedure for deriving temperature is similar to the point measurements using the PMT described above. The following differences arise from: the use of a camera to image a line of pixels instead of a point, and the removal of the rotary chopper. 4x4 pixel binning was used to give an effective spatial resolution of 120 μm/pixel using a 60 mm focal length lens in a 2*f* imaging configuration. Owing to the inability of the camera to capture images quasi-continuously at kHz rates, sequential recording of fluorescence from 410 and 451 nm excitation was not

possible. Sequential recording would enable capture of fluorescence stemming from alternating laser output as a result of using the rotary chopper. Each temperature measurement is calculated from the sequentially recorded fluorescences during one cycle. As discussed earlier with regard to Fig. 6.5 and the problem of uneven seeding, if the time between the sequentially recorded fluorescences (*i.e.* the modulation rate) is too slow, the fluorescences will not be correlated and this would lead to random error in the temperature measurement. To overcome this problem in relation to the slow camera, the captured fluorescence was averaged in order to level-out the effect of the unevenness of the seeding. The average here was a 'phase-average' and so the averaging was made possible in this transient flame due to the periodicity of the pulsed flame. The procedure involved firstly removing the chopper, which allowed for the continuous excitation of the seeded flame by each laser. The exposure time on the camera was set to 100 μs, in order to capture, and hence time-resolve, the fluorescence originating from either laser. The camera was triggered to capture the fluorescence with this exposure time, thus allowing the time-resolved temperature measurements to be matched to the 3.5 kHz downsampled dataset described earlier. The fluorescence images corresponding to 410 nm excitation were accumulated first, and then the same procedure was repeated for the 451 nm transition. The values of phase-averaged temperatures were then computed from the phase-averaged values of fluorescence along the line.

6.4 Results and Discussion

6.4.1 Demonstration of Reproducibility

The first set of results presented here concerns the reproducibility of the temperatures measured within the sinusoidally-forced flame on the Bunsen burner. Continuously time resolved temperature measurements were made at a fixed point within the flame, as denoted by the cross in Fig. 6.7. Figure 6.7 shows the phase-averaged chemiluminescence images of the sinusoidally-forced flame at intervals of 40^{o} though the forcing cycle. From these images, the flamefront can be identified from the intense thin region of chemiluminescence. During the cycle, the flamefront passes the point of measurement at the position of the cross. The corresponding instantaneous temperatures are shown in Fig. 6.8 (a).

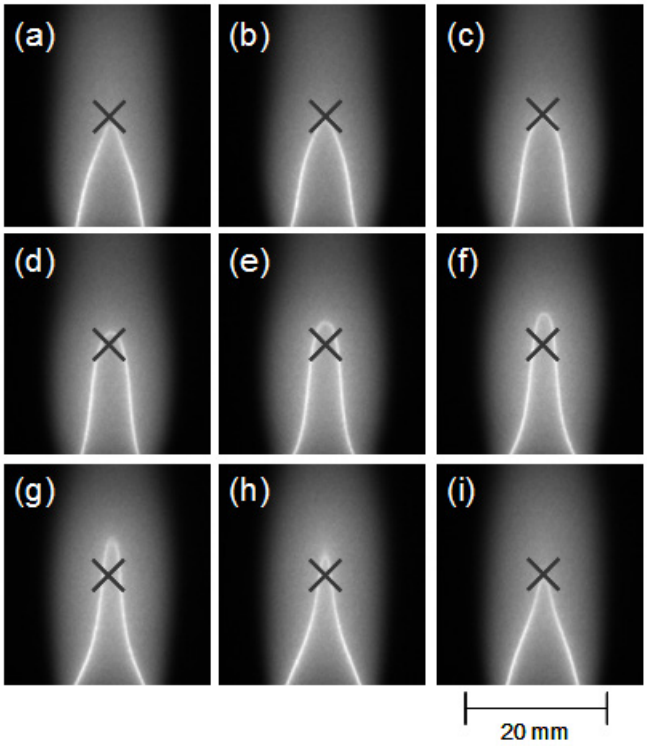

Figure 6.7: (a)-(i) of indium chemiluminescence shows the flamefront evolution as a result of sinusoidal forcing at 114 Hz, in steps of 40^{o} through the cycle.

Figure 6.8 (a) shows instantaneous temperature for four example cycles in the flame. The temperature was measured at 14 kHz in order to minimise the error, and then downsampled to an effective measurement speed of 3.5 kHz. This is shown in the legend of Fig. 6.8 (a). During the cycle it can be seen that there is a consistent rise and fall of temperature, which corresponds to the crossing of the flamefront with the measurement point as shown by the cross in Fig. 6.7. The gaps showing no data occur as a result of the lack of signal at the lower temperatures through the cycle. This is due to the lack of atomic indium, as a result of insufficient volatisation. Furthermore, it is clear that

temperatures measured using fast TLAF are qualitatively reproducible, as shown by the regular variation for the four example cycles.

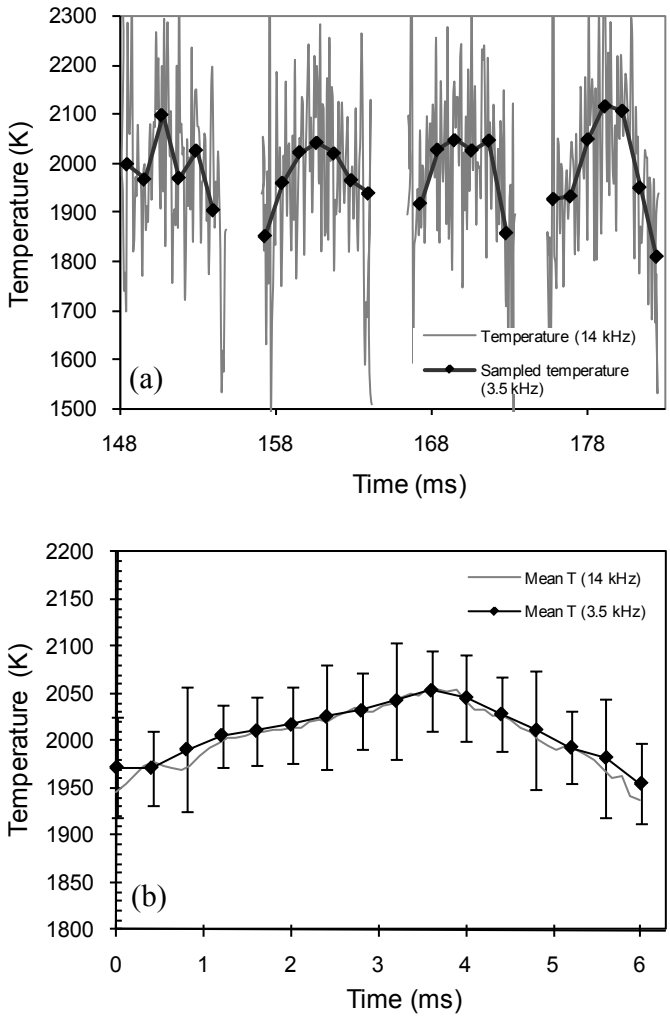

Figure 6.8: (a) – time trace showing the instantaneous temperature measurements at 114 Hz forcing for four cycles. (b) – the phase-average of 100 cycles.

However, in order to gain a more quantitative measure of the reproducibility of the data a phase-averaged plot complete with error bars was constructed. This is presented in Fig. 6.8 (b), where the error bars are shown for the downsampled data at 3.5 kHz. It is seen that the uncertainty in the phase-averaged downsampled temperature is consistently within the limits of 2 - 3 %. This is in accord with the precision that was estimated from the laminar flat flame, as shown in Fig. 6.6. The relatively small uncertainty in temperature demonstrates and confirms the good reproducibility of the measurements in the periodically forced flame. It is noteworthy that the uncertainty does not suddenly increase close to the flamefront. The points of data at the two ends of the plot in Fig. 6.8 (b) approximately correspond to where the flamefront crosses the measurement point. For one of these datum points at a time of 6 ms, the uncertainty is only 2.2 %. The level of precision is of the same order in relation to the other error bars during the cycle. This behaviour is also consistent with the independence of the temperature uncertainty in relation to the distance from the flamefront, as shown by the profile corresponding to the measurement speed of 14 kHz in Fig. 6.5.

6.4.2 Resolution of Dynamic Flame Features

To further demonstrate the capability of the technique to resolve dynamic flame features, measurements were conducted within a pulsed Bunsen flame similar to one described in Frank and Settersten, (2005). The flame was visualised with an intensified CCD camera and shown in Figs. 6.9 (a) – (f). The time separation between subsequent images is 1 ms. A small flame “globule” is pinched-off and convects downstream following each pressure

pulse. The point marked with a cross on the images denotes the position where time resolved TLAF measurements were performed at a measurement speed of 14 kHz. The corresponding instantaneous temperature trace is shown on the bottom pane (grey line: raw data, black line: average over 4 temperature samples, giving an effective sampling rate of 3.5 kHz.). A sample trace of the raw fluorescence signal is also shown for a snapshot in time over 7 cycles at 14 kHz, where the three signals at 410 and 451 nm, along with the background, are shown for each cycle.

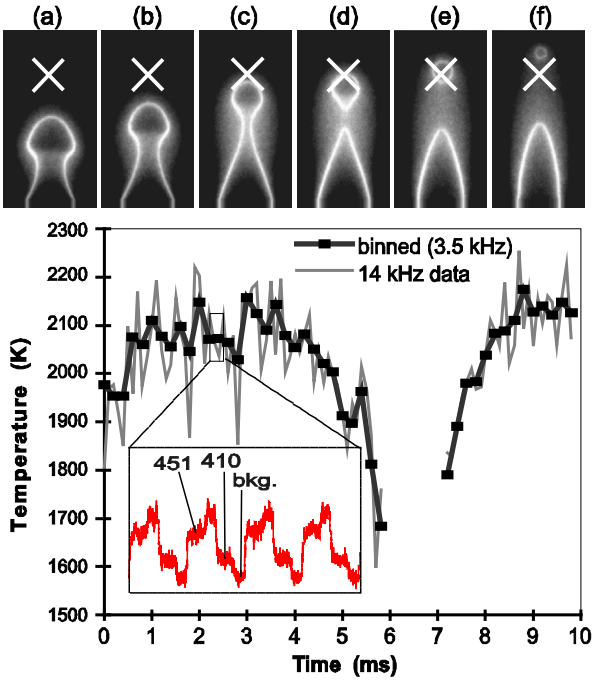

Figure 6.9: (a)-(f) of indium chemiluminescence shows the flamefront evolution after a pulse in steps of 1 ms. The corresponding plot shows time resolved temperatures at point X in the flame along with the original fluorescence trace. A sample fluorescence trace is also shown for a snapshot in time for 4 cycles at 14 kHz.

At a 3.5 kHz effective sampling rate - which corresponds to a realistic convective Batchelor frequency in many flames (Cabra *et al.* 2002) – our measurement precision is 1.5 % at a temperature of ~2000 K, which compares very favourably with results obtained in previous experiments using laser powers up to 80 times larger than presently used (Dec and Keller 1986). Furthermore, the spatial resolution of our technique, which is limited by the 150 μm diameter pinhole of the PMT, is good enough to resolve Batchelor length scales of 200 - 500 μm (Wang *et al.* 2005). The temperature trace in Fig. 6.9 exhibits a pronounced dip in temperature when the laser beam is inside the flame globule where cool reactants are present. No data from the cool reactants within the flame bubble were available due to the lack of free In atoms in this location. As the bubble passes through the measurement location the temperature rises once again. Note that the temperature profile is not symmetric in time because the flame bubble is changing shape as it convects upstream since the flame consumes the reactants inside, it becomes progressively smaller in time.

6.4.3 One Dimensional Measurements

Further to the demonstration of the time resolution capability of fast TLAF, the potential to spatially resolve in 1-D was tested. This involved the use of an ICCD camera to capture the fluorescence on a line of pixels on the chip. The chip underwent 4x4 binning, which gave an effective spatial resolution of 120 μm/pixel with 2*f* imaging and f = 60 mm. 1-D imaging was tested at three different vertical positions within the pulsed flame at one point during the pulsed cycle; this is shown in Fig. 6.10 (d). The results of the spatial

resolution test are exhibited in Figs. 6.10 (a) – (c), and these plots show the phase-averaged result of 100 cycles for the three vertical positions.

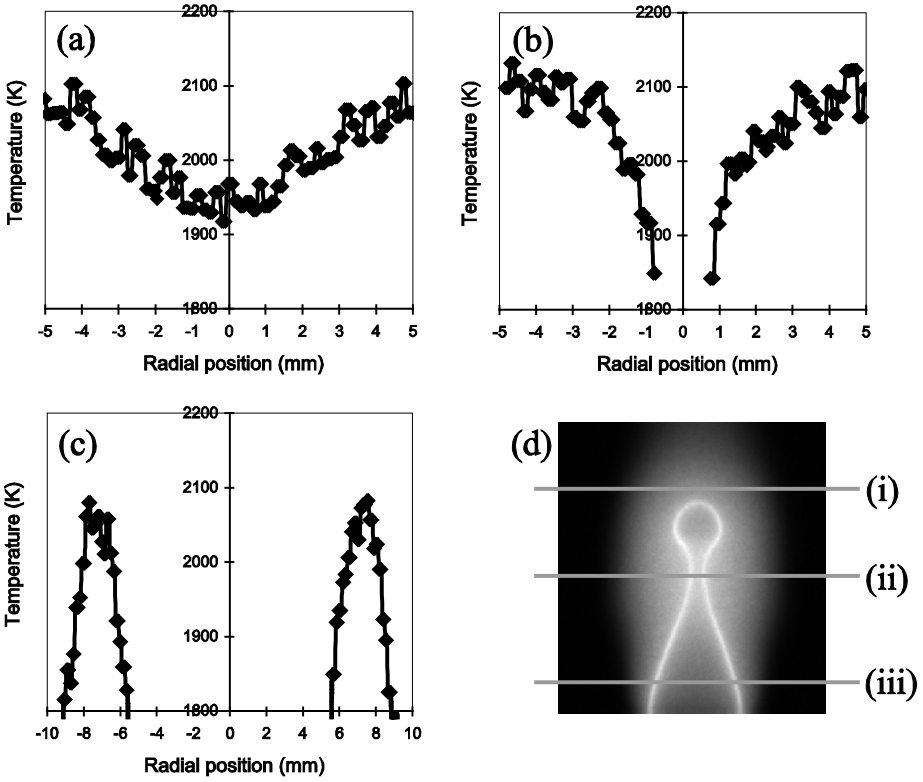

Figure 6.10: (a)-(c) shows one-dimensional temperature profiles, whose paths intersect the burner's axis. The vertical positions of the paths through the flame are shown in (d) within chemiluminescence images at the phase shown through the acoustic cycle.

Figs. 6.10 (a) – (c) show the phase-averaged temperature profiles of the flame at a point in time after the pulse. For vertical position (i), the corresponding profile in Fig. 6.10 (a) shows that the temperature rises slightly by about 150 K. In view of the fact that path (i) is ~1 mm above the flamefront, the slight temperature increase is thought to be attributable to the slow exothermic

oxidation reaction ($CO + OH \rightarrow CO_2 + H$) that occurs beyond the flamefront (Echekki and Chen 1996). Other features can be identified through the profiles. These include the regions of the flame that have omitted temperature data due to the lack of signal in these regions. This corresponds to the small gap between the two flamefronts, which are almost touching at the middle of path (ii) of Fig. 6.10 (d), and the corresponding larger gap in path (iii).

The limitations of the 1-D implementation are considered here. Despite the similar spatial and temporal resolution to the point measurements demonstrated earlier using the PMT, larger uncertainties exist in the temperatures. The best precision that can be achieved is approximately 4 %, close to the hottest locations in the profile of Fig. 6.10 (c); this is more than the 1.5 % error seen for the point measurements. The camera exposure time used here was ~100 μs, which corresponds to the signal collection time for a modulation frequency of 3.5 kHz in the point measurements. The reason for the lower precision in the 1-D case owes to the use of the ICCD camera, which had a quantum efficiency of ~20 % at 451 nm detection; this is lower than for a PMT by ~10 %. Furthermore, the camera was incapable of quasi-continuous recording of fluorescence, and therefore the phase-averaged method was used instead to overcome the problem of uneven seeding (as described earlier in section 6.3). When the temperature precision is calculated from the uncertainties of the 100 repeated fluorescence measurements in the phase-averaging, the covariance between the signals corresponding to 451 and 410 nm excitation could not be computed, since the covariance is unknown. This is because, due to the low repetition rate of the camera, sequential detection of the signals from 451 and 410 nm excitation could not be

achieved. This results in signals that are not correlated between the two excitation wavelengths. Sequential detection would otherwise allow covariance to be estimated, and would lead to a lower estimate of the temperature uncertainty. For this reason, the temperature uncertainty here is overestimated. However, the use of next generation ICCD camera technology would permit quasi-continuous recording, and hence sequential detection, at up to 50 kHz rates. This results in more accurate estimates of temperature precision, but more importantly it would allow quasi-continuous temperature measurements to be made in 1-D. Nevertheless, the implementation of indium TLAF with an ICCD camera here provides a demonstration in 1-D with approximate values of temperature uncertainty. The indium TLAF technique detailed in this work together with the use of better camera technology would extend the capabilities of the point measurement implementation described here.

6.5 Conclusions

In conclusion, we have shown for the first time that low power diode lasers can be used in combination with indium TLAF to measure spatially and temporally resolved temperatures quasi-continuously with favourable precision. The setup required is comparatively simple and economical compared to alternative techniques. We show that indium concentration fluctuations within the flame can exacerbate errors at slow measurement speeds and that, for the conditions used in the present experiments, an optimal precision is obtained at a measurement speed of around 14 kHz for locations near the flamefront. By downsampling from 14 kHz, we demonstrated quasi-

continuous temperature measurements at an effective rate of 3.5 kHz within a steady laminar test flame, which yielded an estimate of the technique's precision of 1.5 % at ~2000 K. Further experiments were conducted at 3.5 kHz within a sinusoidally-forced Bunsen flame, which resulted in regular variations in the measured temperatures, whose standard deviations did not exceed 3 % within the hot gases where there was sufficient volatised indium. Fast TLAF was also applied to a pulsed Bunsen flame demonstrating the resolution of dynamic flame features at an effective measurement speed of 3.5 kHz. This showed that it was possible to capture transient small-scale features that would otherwise be impossible using many other thermometric techniques. Moreover, the potential to spatially resolve in 1-D was tested within the same pulsed flame. This was done by modifying the setup where a triggerable ICCD camera was used instead of a PMT in the absence of a chopper. Phase-averaged measurements were recorded with an exposure time that matched an effective measurement speed of 3.5 kHz. The spatial resolution of 120 μm/pixel is less than typical Batchelor lengthscales of 200 - 500 μm in turbulent flames. The precision of these measurements is of the order of 5 %. Nevertheless, fast TLAF has shown to be able to spatially and temporally resolve dynamic flame features that would otherwise be impossible with static thermometry techniques. Ultimately, there is scope for this technique to collect data in turbulent systems, for use in CFD code validation and model development.

Chapter 7

Conclusions and Future Work

The development and application of laser based diagnostic techniques in this work have led to several conclusions, which have been discussed extensively in the previous chapters. In the following sections, we provide general conclusions and list the achievements with regard to the aims outlined in chapter 1. Finally, future recommendations are also made to build on the present effort.

7.1 Overview

The overarching goal of the work in this thesis has been the application of laser based diagnostic techniques to either validate or provide accurate input temperature data for CFD models in technical combustion. Part of this goal has also consisted of the development of existing laser based techniques to obtain more accurate and precise data. Such high fidelity data is required because of the use of CFD models, whose output is a sensitive function of temperature. CFD models are a powerful tool for predicting and controlling combustion behaviour, however they rely on the need for underlying assumptions that simplify aspects of the modelled combustion physics owing

to limited computational resources. These assumptions need to be tested, and this is done by comparing the output of such models with accurate experimental data. The work presented in this thesis comprise of a number of related studies, in which either experimental data is acquired for model validation or new laser techniques are developed for the purpose of validation. The main results of the work here are summarised below.

7.2 Summary of Main Results

In chapter 3, an improved method for the computation of curvature and its application to turbulent premixed flame correlations had been developed and tested in this study. Qualitative differences of the correlations of integrated HRR and flamefront curvature were identified between our results and that of Ayoola *et al*. (2006). It was shown by using our improved method of computing curvature that an identifiable trend exists between all three flames studied, which was not evident in (Ayoola *et al*. 2006). Furthermore, agreements were found between the experimental correlations reported here and the behaviour that would be expected based on the thermodiffusive argument put forth by Williams, (1986), in addition to the DNS results in the literature.

In chapter 4, CARS was applied to an acoustically-forced turbulent lean premixed flame stabilised on a model burner, whose design was modelled to mimic phenomena of relevance in industrial combustors. Previously, two-line OH PLIF had been applied to the flame and it was suspected that the associated results were inaccurate. By using CARS, this was shown to be the

case for the inner region of the flame where there was up to a 47 % discrepancy in temperature.

In chapter 5, it was shown for the first time that temperature measurements with excellent accuracy and precision in low pressure sooting flames could be performed without recourse to calibration. This was achieved by employing extended cavity diode lasers in combination with two-line atomic fluorescence of seeded indium. The accuracy achieved was better than ~ 1.7 % with a precision of 1.4 %, which is a significant achievement for sooting thermometry. Both the high precision and accuracy of the technique allowed for the deduction that the temperature in the flames studied here is relatively insensitive to pressure in contrast to soot volume fraction, in the pressure range of 18.7 kPa – 26.7 kPa.

Finally in chapter 6, we had shown for the first time that low power diode lasers can be used in combination with indium TLAF to measure spatially and temporally resolved temperatures quasi-continuously with favourable precision. We demonstrated quasi-continuous temperature measurements at an effective rate of 3.5 kHz in a steady laminar test flame, which yielded an estimate of the technique's precision of 1.5 % at ~2000 K. Fast TLAF was also applied to a pulsed Bunsen flame demonstrating the resolution of dynamic flame features at an effective measurement speed of 3.5 kHz. This showed that it was possible to capture transient small scale features that would otherwise be impossible using many other thermometric techniques.

7.3 Future Work

In this section, possible extensions of the work presented in this thesis are suggested, in order to develop further insight into combustion processes by either application of the experimental data generated in this work to models, or advancement of the techniques developed here. This includes the development of URANS and LES models by validating with the CARS generated temperatures to understand the dynamics of the acoustically forced flame. Development of sooting flame models for methane combustion at low pressure is also another candidate, where experimentally determined temperatures can be used. Finally, the fast TLAF technique has potential for further development through use of more advanced detection technology.

7.3.1 Development of URANS and LES Models

In chapter 4, it was shown by using CARS that temperature in the acoustically forced flame could be measured with greater accuracy than with OH PLIF. This enables improved CFD models to be developed for the burner, where the boundary conditions for temperature can be made more realistic in contrast to the previous adiabatic assumptions by Armitage *et al.* (2006). Currently, improvement of URANS models for the burner are underway at Cranfield University by Armitage. Adoption of improved boundary conditions would yield different spatial distributions of temperature in a newly developed URANS model of the flame. The temperatures could then be compared to that from CARS in this work. It should be noted that some of the regions of the flame where temperature was measured using CARS were relatively

unaffected by the biasing towards pockets of colder temperatures in the measurement volume, as seen in chapter 4. This was because these regions were relatively thermally homogeneous. These homogeneous regions resulted in reliable phase-averaged temperatures, as they were unaffected by the biasing. This permits the direct comparison with URANS results. Alternatively, if LES models were developed for this burner, there is scope that all the temperature distributions from CARS could be used for the purpose of model validation, irrespective of biasing; this is possible for the following reasons. LES models randomly fluctuating small scale structures in the flowfield. In the case of a region representing the CARS measurement volume within the LES model, there would exist small pockets of cooler gas similar to the experiments described in chapter 4 that result in biasing. In the recording of the phase-average, there will be fluctuations in the proportion of cool gas in the volume from measurement to measurement. This would result in a histogram of measurement volume temperature. As a way to validate LES thoroughly, such frequency distributions of temperature could be regenerated. This could be done by artificially generating CARS spectra over the measurement volume, which would allow 'mixed' spectra to be computed. The 'mixed' spectra that results from the thermal heterogeneity of the measurement volume would then be fitted to CARS spectra. These fits to the 'mixed' spectra would serve to regenerate the temperature histograms presented in this work. A direct comparison of the temperature statistics would then be possible, thereby permitting the validation of the LES model.

7.3.2 Development of Sooting Flame Models

In chapter 5, the application of indium TLAF thermometry to sooting flames was made at the University of Lille under carefully controlled conditions. Temperature profiles were measured at equivalence ratios and pressures to contribute to the concerted effort towards understanding the early stages of soot formation in methane flames. The temperatures would be used as input data to numerical models of the laminar sooting flame. Further experimental data is also being generated for this purpose, which include concentration profiles of PAHs and aromatics (Mercier *et al.* 2008). These are being recorded prior to the impending development of the numerical model of soot formation in methane flames at the University of Lille.

7.3.3 Rapid 2-D TLAF Thermometry

A development of the indium TLAF thermometric technique was presented in chapter 6, where temperature could be measured at kHz rates. There is scope for improvement to this technique, which is proposed in the following. Firstly, the seeding process could be improved by seeding the reactant flow with an organic indium compound. This could be introduced by evaporation into the flow, where the compound in its gaseous state would decompose and liberate indium atoms at the flamefront. In contrast to seeding with indium chloride as in this work, the new method would circumvent the problem of incomplete, and hence discontinuous, seeding at the flamefront. Smoother seeding would result in lower uncertainties introduced by incomplete seeding, and hence provide better precision in measured temperature. Secondly, the use of newly developed ICCD camera technology, which can operate at up to 50 kHz frame

rates, would permit the quasi-continuous capture of modulated 451 and 410 nm fluorescence. This would extend the capability of the fast TLAF technique to 1-D measurements, as detailed in chapter 6. Moreover, the use of more powerful blue diode lasers, which are currently available, would also permit 2-D measurements to be made by expansion of the laser beam in the measurement plane with acceptable signal-to-noise levels. This would ultimately lead to the ability to resolve complex dynamic flame features in a measurement plane at turbulent flame time scales.

Appendix A

Derivation of 2-D Coordinate-Transformation Invariant Curvature

In chapter 3, a formulation for the curvature of flamefronts was presented; here, a rigorous treatment is given.

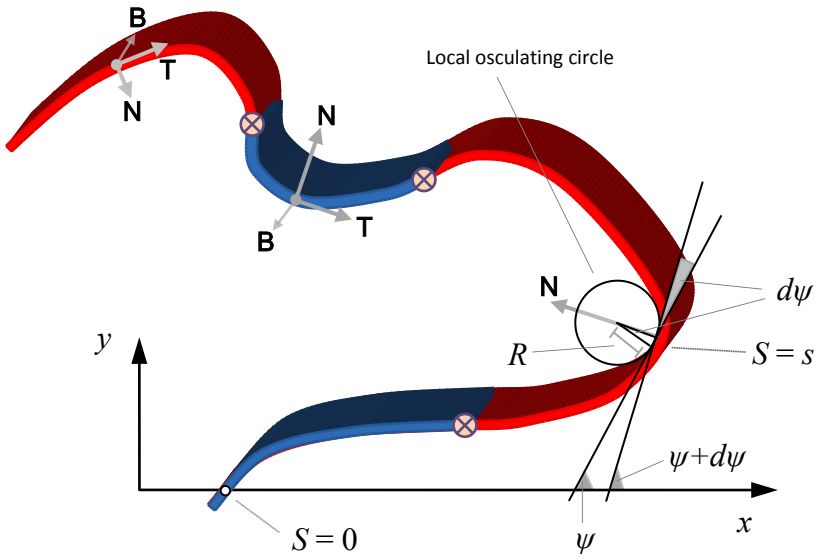

Figure A1: Illustration of a typical flamefront configuration and its associated coordinate-transformation invariant curvature. The sign of the curvature is denoted by a colour change and the crosses mark the points of inflexion. **T** and **N** are the unit-tangent- and normal-vectors respectively. The intrinsic coordinates are represented by S and ψ, and R is the radius of curvature.

An illustration is shown in Fig. A1, which represents a likely flamefront configuration. Using intrinsic coordinates to derive a measure of curvature from the osculating circle, a definition of unsigned curvature can be related to the radius of curvature:

$$\kappa_{unsigned} = \frac{1}{R} = \left|\frac{d\psi}{ds}\right| = \frac{\left|\frac{d^2y}{dx^2}\right|}{\left[1+\left(\frac{dy}{dx}\right)^2\right]^{\frac{3}{2}}} = \frac{|x'y''-y'x''|}{\left[(x')^2+(y')^2\right]^{\frac{3}{2}}} \qquad \text{(A1)}$$

Here, the dashed terms represent differentiated variables with respect to the curvilinear coordinate, *s*. It should be noted that the last form of the unsigned curvature in Eqn. A1, which is parametric, is the most useful for arbitrary curves that cannot be expressed as a many-to-one function in *x*. This overcomes the problem of the possibility of the gradient *dy/dx*, and its derivative, becoming undefined, at the locations where *dx/dy* = 0. Nevertheless, this definition is not yet complete without including the directional sense of curvature; this is termed 'signed curvature' and is treated with the following vectorial argument, with the aid of Fig. A1.

Consider a unit-tangential vector, **T**:

$$\mathbf{T} = \frac{dx}{ds}\mathbf{i} + \frac{dy}{ds}\mathbf{j} \qquad \text{(A2)}$$

Consider a normal vector, **N**:

$$\mathbf{N} = \frac{d^2x}{ds^2}\mathbf{i} + \frac{d^2y}{ds^2}\mathbf{j} \tag{A3}$$

The tangential vector is defined in such a way that the *x*- and *y*-components always ensure that the tangential direction is in accord with a continuous change in *s*. The normal vector is defined such that it always points toward the centre of the local osculating circle (Dörrzapf 2006), which can be seen from Fig. A1. The binormal vector can now be derived from a vector cross-product of **T** and **N**, hence:

$$\mathbf{B} = \mathbf{T} \times \mathbf{N} = \left[x'y'' - y'x''\right]\mathbf{k} \tag{A4}$$

The sign of the *z*-component of **B** determines which side of the curve the normal vector lies, and hence whether the curve is locally concave or convex. But more importantly, it should be noted that the *z*-component of **B** is concurrent with the argument of the numerator in the parametric form of Eqn. A1, such that a signed curvature can now be derived from removing the magnitude operator in Eqn. A1, hence the fully defined curvature that has been used in this work becomes:

$$\kappa_{signed} = \frac{x'y'' - y'x''}{\left[(x')^2 + (y')^2\right]^{\frac{3}{2}}} \overset{!}{\equiv} \frac{1}{R} \tag{A5}$$

Equation A5 shows that the signed curvature is not identical to the inverse radius of curvature, as the radius of curvature can only adopt positive values; this is often misunderstood and neglected in the combustion literature.

Appendix B

Estimation of Thermal Boundary Layer Thickness

As part of the argument in chapter 4 towards the implausibility of the extent of cooling within the burned gases of the acoustically-forced flame implied by the results from OH PLIF (Ayoola *et al.* 2009), we estimated the thermal Boundary Layer (BL) thickness using the analogy set in the following section. The BL thickness indicates the intensity of conduction of heat away from the hot burned gases to the relatively cool metal bluff body, as seen in chapter 4.

Here, we obtain an approximate magnitude of what the thermal BL thickness may be based on an analogous scenario. This scenario is illustrated in Fig. B1 in which uniform laminar flow at temperature T_o is directed over a flat plate at temperature T_w. Figure B1 also shows how the thermal boundary layer develops from the laminar to the turbulent regime. The BL thickness, denoted as $\delta_{th,}$ is defined as the distance over which the temperature changes from T_w to $0.99T_o$ at a horizontal distance Z, where $T_o > T_w$.

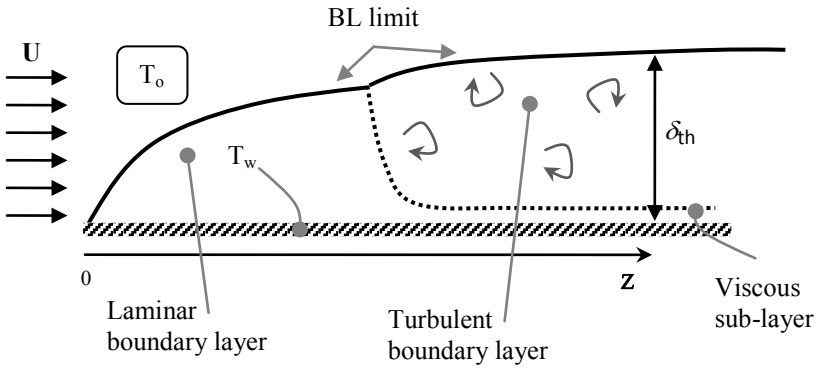

Figure B1: Illustration of an analogous case of a turbulent thermal boundary layer (BL) for uniform laminar flow over a flat plate. Here, the BL limit for temperature is taken as 99 % of T_o.

The analogous situation shown in Fig. B1 is similar to the case in chapter 4 where the burned gases within the inner recirculation zone flow over the bluff body surface from the burner axis (radial position of zero) to the lip of the bluff body where the flame is stabilised (radial position of 12 mm). Close to the bluff body surface, the flow is similar to the case of laminar flow over a flat plate - only in the phase-averaged sense. This is because the instantaneous flow in the acoustically-forced flame is turbulent, yet when phase averaged the flow field exhibits uniformity. The setup shown in Fig. B1 can be imagined to be similar in that the plate represents the bluff body surface, and the oncoming flow originates from the recirculation of the burned gases from further above in the flame at a radial distance Z = 0 from the burner axis. In our flame, the entire flow field is turbulent and therefore no such laminar boundary layer exists. As an approximation, an upper bound of the thermal BL thickness in our real flame is estimated from the turbulent BL thickness of

the flat plate case. The turbulent regime for the plate occurs at a Reynolds number Re_z in excess of 10^5 (Incropera and De Witt 1996).

Here, we derive a conservative estimate of the thermal BL thicknesses present at the bluff body surface in our flame. We employ the Prandtl-Taylor analogy (Incropera and De Witt 1996) using the following definitions:

Reynolds number: $\mathrm{Re}_z = \dfrac{\rho U Z}{\mu}$

Prandtl number: $\mathrm{Pr} = \dfrac{\mu C_p}{k}$

Nusselt number: $\mathrm{Nu} = \dfrac{hd}{k}$

Stanton number: $\mathrm{St} = \dfrac{hZ}{\mu C_p \,\mathrm{Re}_z}$

j-factor: $j_\mathrm{H} = \mathrm{St} \cdot \mathrm{Pr}^{2/3}$

The Prandtl-Taylor analogy formulation is given by:

$$\mathrm{Nu} = 0.036 \cdot \mathrm{Re}_z^{0.8} \cdot \mathrm{Pr}^{0.33} \tag{B1}$$

$$j_\mathrm{H} = 0.036 \cdot \mathrm{Re}_z^{-0.2} \tag{B2}$$

The fluid parameters used in the above formulation are taken at the average of the two temperatures T_w and T_o, and are presented in Table B1.

Parameter	Value	Unit
Density, ρ	0.3	kg/m^3
Viscosity, μ	53×10^{-6}	Pa.s
Specific heat capacity, C_p	1200	J/kg/K
Thermal conductivity, k	0.05	W/m/K

Table B1: Parameters evaluated at averaged temperature**.**

For turbulent conditions at the lower bound $Re_z = 10^5$, using the above formulation and parameters, we obtain the heat transfer coefficient h = 1900 $W/m^2/K$ at the upper bound Z = 12 mm at the lip of the bluff body. The thermal BL thickness can now be estimated from the Nusselt number in conjunction with the heat transfer coefficient, giving: $\delta_{th} \sim 8$ mm.

It should be noted that if a higher Reynolds number were selected, for example: 10^6, then δ_{th} would be ~9 mm. With one order of magnitude increase in Re_z, there is virtually little change in δ_{th}. This insensitivity thus demonstrates the unimportance of the choice of Re_z for the purpose of merely acquiring an approximation of δ_{th} in our argument for the implausibility of the previous OH PLIF results of the flame (Ayoola *et al.* 2009).

Appendix C

Estimation of Uncertainties in TLAF Temperatures

As discussed in chapter 5, systematic uncertainties exist in the measured temperatures from the implementation of the sooting TLAF scheme. In this appendix, estimates are derived for the potential error sources: the powermeter calibration, the vertical misalignment of the two laser beams and Mie scattering from soot.

C.1 Error from the powermeter

This calculation estimates the error that might have arisen from the calibration of the photodiodes with the blackbody thermopile powermeter. For systematic errors, the general formulation for the propagation of uncertainties in all variables is:

$$du = \frac{\partial u}{\partial x}\Delta x + \frac{\partial u}{\partial y}\Delta y + \frac{\partial u}{\partial z}\Delta z + \ldots \qquad \text{(C1)}$$

Here, du is the systematic error in u for uncertainties in dependent variables, x, y and z *etc*.

Application of Eqn. C1 to the TLAF temperature formulation (derived in chapter 2) yields the relative error in temperature. The systematic error is given by:

$$\frac{dT}{T} = \frac{kT}{\Delta E}\left(\frac{\Delta M_{451}}{M_{451}} - \frac{\Delta M_{410}}{M_{410}}\right) \tag{C2}$$

Here, M_λ is the powermeter reading (in milliwatts) corresponding to excitation wavelength λ. The parameters are given below for the error estimates in Table C1.

Parameters	Best case	Worst case
T = 1850 K	**|dT/T|= 0.4 %**	**|dT/T|= 1.7 %**
M_{410} = 0.9 mW	ΔM_{410} = 0.01 mW	ΔM_{410} = 0.01 mW
M_{451} = 0.55 mW	ΔM_{451} = 0.01 mW	ΔM_{451} = -0.01 mW

Table C1: Powermeter error estimates

It is seen that a zero-error that has an offset of up to 0.01 mW that is of different sign for the two parts of the calibration can result in a larger error of 1.7 %. Since the relative error is proportional to temperature, the maximum temperature of 1850 K in our experiments was chosen. This was done to yield an upper bound of the powermeter calibration error in these experiments.

C.2 Error from vertical misalignment of beams

Another appreciable source of error may result from careless overlapping of the laser beams from the two diode lasers. This could result in either misalignment in the horizontal or vertical planes. The former is not an issue since gradients of temperature and indium fluorescence in these directions are small in comparison to the vertical direction. To estimate the largest possible error from imperfect overlap, a hypothetical vertical misalignment is considered here.

Application of Eqn. C1 to the TLAF temperature formulation yields the relative error in temperature. The systematic error is given by:

$$\frac{dT}{T} = \frac{kT}{\Delta E}\left(\frac{1}{F_{410}}\right)\left(\frac{\partial F_{410}}{\partial L}\right)\cdot \Delta L \qquad \text{(C3)}$$

Here, the worst case scenario of the 410 nm beam being misaligned by amount ΔL is considered because the rate of change in 410 fluorscence with change in height is greater than that for 451 nm. The group of terms preceding ΔL in Eqn. C3 was plotted with height, and it was found that the highest value occurred close to the steepest parts of the profiles of temperature and $\partial F_{410}/\partial L$. The plot of how the magnitude of the relative error in temperature varies with misalignment is shown in Fig. C1.

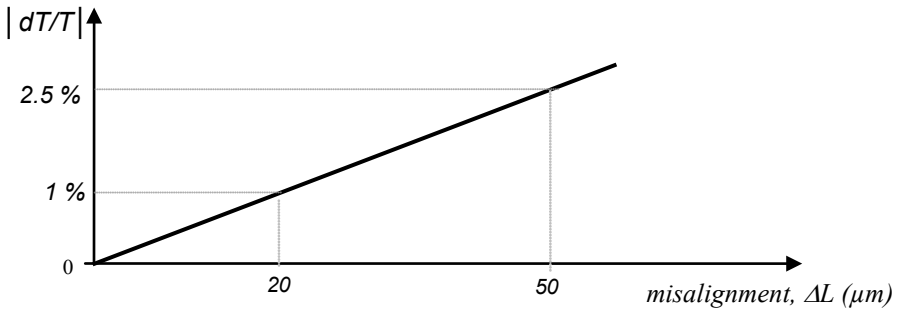

Figure C1: Illustration of the relationship between relative error in temperature and vertical misalignment at the most sensitive conditions (see text).

C.3 Error from soot scattering

The aim of this error calculation is to estimate the maximum systematic error from the contribution of soot scattering to the signal detected at 451 nm resonance fluorescence.

Application of Eqn. C1 to the TLAF temperature formulation (derived in chapter 2) yields the relative error in temperature - considering only the error in the signal at 451 nm.

$$\frac{dT}{T} = \frac{kT}{\Delta E}\left(\frac{\Delta F_{451}}{F_{451}}\right) \tag{C4}$$

Here, k is the Boltzmann constant, ΔE is the energy difference between the two lower levels in the TLAF scheme used here, and F_{451} is the integrated signal at 451 nm resonance fluorescence.

The error caused by Mie scattering from soot originates from the error in the integrated signal at 451 nm (*i.e.* ΔF_{451}). A derivation of the error is given below. It should be noted that all the variables below are corrected for background. These variables include: $g(\nu)$, $L(\nu)$ and $f(\nu)$, which are the detected scatter, laser power and signal at 451 nm respectively, as illustrated in Fig. C2.

In the process of computing temperature from the TLAF spectra, the raw spectra, $f(\nu)$, are normalised by the laser power, $L(\nu)$, to yield a normalised spectrum:

$$\frac{f(\nu)}{L(\nu)} = F(\nu) \tag{C5}$$

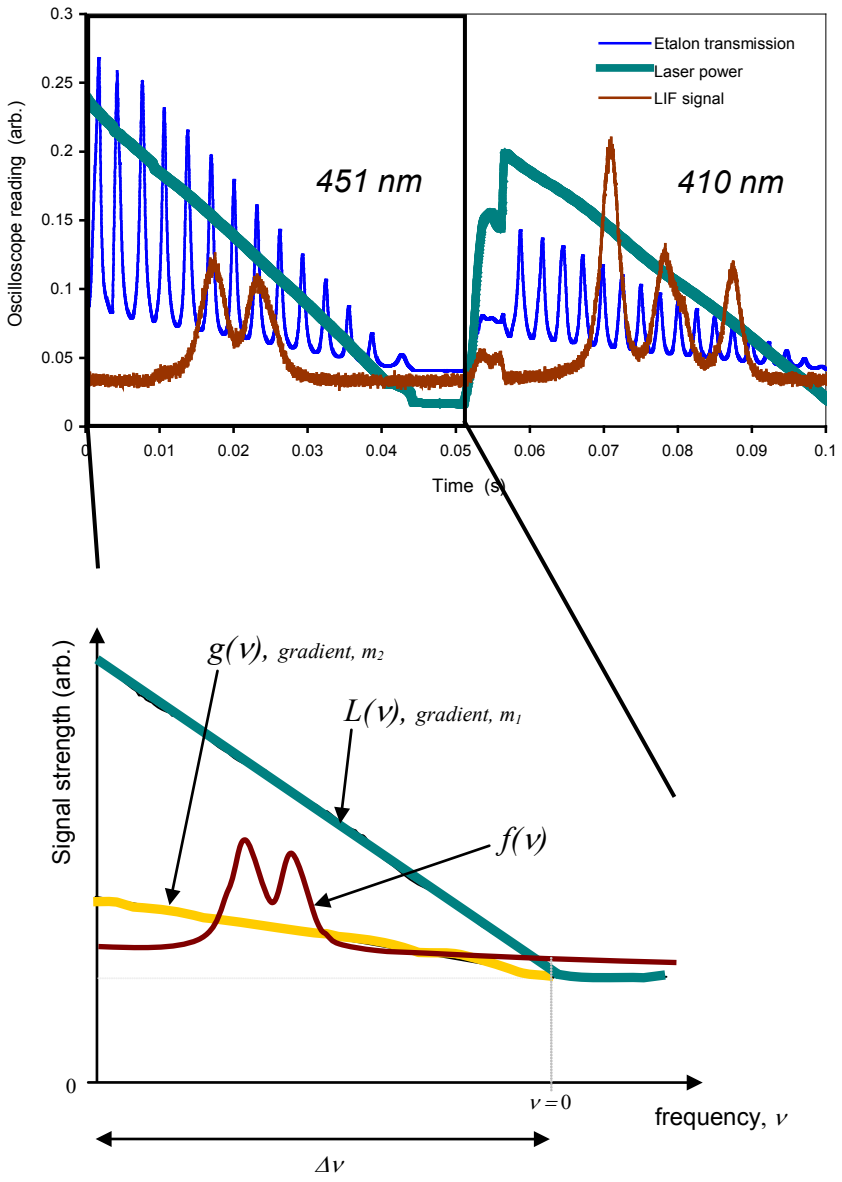

Figure C2: Illustration of the traces $g(\nu)$, $L(\nu)$ and $f(\nu)$, which are the detected scatter, laser power and signal at 451 nm respectively, over a window of $\Delta\nu$.

However in the presence of scattering, a linear contribution, $g(\nu)$, is added to the fluorescence signal during the wavelength scan, as illustrated in Fig. C2. Upon normalisation, this results in:

$$\frac{f(\nu)+g(\nu)}{L(\nu)} = F(\nu)+\frac{g(\nu)}{L(\nu)} \tag{C6}$$

Integration of both Eqns. C5 and C6 allows ΔF_{451} to be determined:

$$\Delta F_{451} \equiv \int_0^{\Delta\nu}\left(F(\nu)+\frac{g(\nu)}{L(\nu)}\right)d\nu - \int_0^{\Delta\nu}F(\nu)\,d\nu = \Delta\nu\left(\frac{m_2}{m_1}\right) \tag{C7}$$

The above holds because both $g(\nu)$ and $L(\nu)$ are linear with gradients m_2 and m_1 respectively. This results in an expression for the relative error in temperature as a function of soot volume fraction, shown in Eqn. C8.

$$\frac{dT}{T} = \frac{kT}{\Delta E}\Delta\nu\left(\frac{m_2}{m_1}\right)\frac{1}{F_{451}} \propto \left(\frac{kT}{\Delta E}\frac{\Delta\nu}{F_{451}}\right)w_{soot} \tag{C8}$$

This is because m_2 is proportional to both the laser power, m_1, and soot volume fraction, w_{soot}. This results in a linear relationship, as shown in Fig. C3.

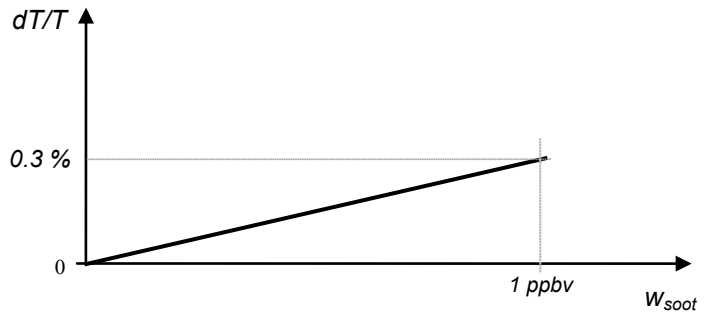

Figure C3: Illustration of the relationship between relative error in temperature and soot volume fraction at constant temperature and integrated signal strength, F_{451}.

The specific values chosen for dT/T and w_{soot} for the linear relation shown in Fig. C3 correspond to the most sooting flame at a measurement location with the greatest soot loading. This corresponds to a pressure of 26.7 kPa, $\phi = 2.32$ at $T = 1630$ K and a height above the burner of 40 mm. This gives an upper bound to the error from Mie scattering in our experiments. The fraction w_{soot} was determined from previous experiments by Desgroux *et al.* (2008) in the same flame. The data of which is shown in Fig. C4, and clearly shows that the soot volume fraction is an order of magnitude larger for a 25 % increase in pressure and at the same equivalence ratio of 2.32.

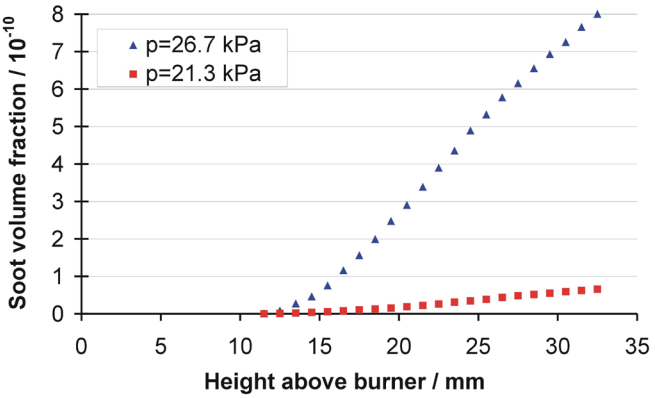

Figure C4: Profiles of soot volume fraction measured by LII and calibrated by CRDS (adapted from Desgroux *et al.* (2008)).

The value of 0.3 % for the relative error was calculated from spectral fitting. This involved firstly normalising a 451 nm spectrum by the laser power, and then subtracting the baseline value from the normalised spectrum. This subtraction corresponds to the systematic error $g(\nu)/L(\nu)$, see Eqn. C6. The correction is simply the offset m_2/m_1. Temperature can then be computed for both the scatter-corrected normalised spectrum and the one including scatter. This results in a relative error of ~ 0.3 % at the sootiest conditions. It is therefore clear that the error from Mie scattering has been less than 0.3 % in this experimental campaign.

References

ALLEN, J.O., DOOKERAN, N.M., SMITH, K.A., SAROFIM, A.F., TAGHIZADEH, K. & LAFLEUR, A.L. (1996). Measurement of polycyclic aromatic hydrocarbons associated with size-segregated atmospheric aerosols in Massachusetts. *Environmental Science and Technology,* **30**, 1023.

AL-OMARI, S.A.B., KAWAJIRI, K. & YONESAWA, T. (2001). Soot processes in a methane-fueled furnace and their impact on radiation heat transfer to furnace walls. *International Journal of Heat and Mass Transfer,* **44**, 2567.

ARMITAGE, C.A, RILEY, A.J., CANT, R.S., DOWLING, A.P. & STOW, S.R. (2004). Flame transfer function for swirled LPP combustion from experiments and CFD. *ASME Turbo Expo. 2004,* 2004-GT-53820.

ARMITAGE, C.A., BALACHANDRAN, R., MASTORAKOS, E. & CANT, R.S. (2006). Investigation of the nonlinear response of turbulent premixed flames to imposed inlet velocity oscillations. *Combustion and Flame*, **146**, 419.

ATAKAN, B. & HARTLIEB, A.T. (2000). Laser diagnostics of NO reburning in fuel-rich propene flames. *Applied Physics B,* **71**, 697.

AXNER, O., GUSTAFSSON, J., OMENETTO, N. & WINEFORDNER, J. (2004). Line strengths, A-factors and absorption cross-sections for fine structure lines in multiplets and hyperfine structure components in lines in atomic spectrometry—a user's guide. *Spectrochimica Acta Part B - Atomic Spectroscopy,* **59**, 1.

AYOOLA, B. (2005). *Laser-based measurement of heat release rate and temperature in turbulent premixed flames*. Ph.D. thesis, University of Cambridge, Department of Chemical Engineering, Cambridge, UK.

AYOOLA, B., BALACHANDRAN, R., FRANK, J., MASTORAKOS, E. & KAMINSKI, C. (2006). Spatially resolved heat release rate measurements in turbulent premixed flames, *Combustion and Flame*, **144**, 116.

AYOOLA, B., HARTUNG G., ARMITAGE C., HULT, J., CANT, R. & KAMINSKI, C. (2009). Temperature response of turbulent premixed flames to inlet velocity oscillations, *Experiments in Fluids*, **46(1)**, 27.

BALACHANDRAN, J. (2005). *Experimental Investigation of the Response of Turbulent Premixed Flames to Acoustic Oscillations*. PhD thesis, University of Cambridge.

BALACHANDRAN, R., AYOOLA, B.O., KAMINSKI, C.F., DOWLING, A.P. & MASTORAKOS, E. (2005). Experimental investigation of the nonlinear response of turbulent premixed flames to imposed inlet velocity oscillations. *Combustion and Flame*, **143**, 37.

BANWELL, C. & MCCASH, E. (1994). *Fundamentals of Molecular Spectroscopy*. London. McGraw-Hill.

BATCHELOR, G. K. (1959). Small-scale variation of convected quantities like temperature in a turbulent fluid. Part 1. General discussion and the case of small conductivity. *Journal of Fluid Mechanics,* **5**, 113.

BENGTSSON, P.E., ALDEN, M., KROLL, S. & NILSSON, D. (1990). Vibrational cars thermometry in sooty flames - quantitative-evaluation of C_2 absorption interference . *Combustion and Flame,* **82,** 199.

BESSLER, W.G. & SCHULZ, C. (2004) Quantitative multi-line NO-LIF temperature imaging *Applied Physics B,* **78**, 519.

BESSLER, W.G., HILDENBRAND, F. & SCHULZ, C. (2001). Two-line laser induced fluorescence imaging of vibrational temperatures in a NO-seeded flame. *Applied Optics*, **40**, 748.

BLANQUART, G. & PITSCH, H. (2009). Analysing the effects of temperature on soot formation with a joint volume-surface-hydrogen model. *Combustion and Flame,* **156(8),** 1614.

BOHM, B., HEEGER, C., BOXX, I., MEIER, W. & DREIZLER, A. (2009). Time-resolved conditional flow field statistics in extinguishing turbulent opposed jet flames using simultaneous high speed PIV/OH-PLIF. *Proceedings of the Combustion Institute,* **32**, 1647.

BOHM, H., HESSE, D., JANDER, H., LUERS, B., PIETSCHER, J., WAGNER, H.G. & WEISS, M. (1988). *Proceedings of the Combustion Institute,* **22**, 403.

BOQUILLON J.P., PEALAT, M., BOUCHARDY, P., COLLIN, G., MAGRE, P. & TARAN, J.P. (1988). Spatial averaging and multiplex coherent anti-stokes raman-scattering temperature-measurement error. *Optics Letters*, **13(9),** 722.

BRAND, J.C.D. (1956). The electronic spectrum of formaldehyde, *Journal of the chemical society*. **APR**, 858.

BURNS, I.S. (2006). *A sensor for combustion thermometry based on blue diode lasers*. Ph.D. thesis, University of Cambridge, Department of Chemical Engineering, Cambridge, UK.

BURNS, I.S., CHRYSTIE, R.S.M., MERCIER, X., WARTEL, M., FACCINETTO, A., DESGROUX, P., LAMOUREUX, N., HULT, J. & KAMINSKI, C.F. Accurate spatially-resolved thermometry in low-pressure sooting flames by two-line atomic fluorescence, (to be published).

BURNS, I.S., HULT, J. & KAMINSKI, C.F. (2004) Spectroscopic use of a novel blue diode laser in a wavelength region around 450 nm. *Applied Physics B*, **79**, 491.

BURNS, I.S., LAMOUREUX, N. & KAMINSKI, C.F. (2008). Diode laser atomic fluorescence temperature measurements in low-pressure flames. *Applied Physics B*, **93(4)**, 907.

CATTOLICA, R. (1981). OH rotational temperature from two-line laser excited fluorescence. *Applied Optics,* **20**, 1156.

CHAKRABORTY, N. & CANT, R. (2005). Influence of Lewis number on curvature effects in turbulent premixed flame propagation in the thin reaction zones regime. *Physics of Fluids*, **17**, 105105.

CHANG, A.Y., BATTLES, B.E. & HANSON, R.K. (1990). Simultaneous measurements of velocity, temperature, and pressure using rapid-cw wavelength-modulation laser-induced fluorescence of OH. *Optics Letters,* **15 (12)**, 706.

CHEN, Y.C. & BILGER, R.W. (2002). Experimental investigation of three-dimensional flame- front structure in premixed turbulent combustion—I: hydrocarbon/air bunsen flames. *Combustion and Flame,* **131**, 400.

CHEN, Y.C. & MANSOUR, M.S. (1997). Simultaneous Rayleigh scattering and laser-induced CH fluorescence for reaction zone imaging in high-speed premixed hydrocarbon flames. A*pplied Physics B,* **64**, 599.

CHRYSTIE, R.S.M., BURNS, I.S., HULT, J. & KAMINSKI, C.F. (2008). On the improvement of two-dimensional curvature computation and its application to turbulent premixed flames. *Measurement Science and Technology,* **19,** 125503.

CHRYSTIE, R.S.M., BURNS, I.S., HULT, J. & KAMINSKI, C.F. (2009). High-repetition-rate combustion thermometry with two-line atomic fluorescence excited by diode lasers. *Optics Letters*, **34(16)**, 2492.

CLARK, G., PALMER, R. & FARROW, R. (1990). CARSFIT computer code, developed at Los Alamos and Sandia National Laboratories.

DAILY, J.W. (1997) Laser induced fluorescence spectroscopy in flames. *Progress in Energy and Combustion Science,* **23(2)**, 133.

DAVIS, M.B., PAWSON, M.D. & VESER, G. (2000). Methane oxidation over noble metal gauzes: An LIF study. *Combustion and Flame,* **123(1-2)**, 159.

DEC, J. & KELLER, J. (1986). High speed thermometry using two-line atomic fluorescence. *Twenty-First Symposium (International) on Combustion (The Combustion Institute, Pittsburgh, Pa, 1986)* 1737.

DEMTRÖDER, W. (2004). *Laser Spectroscopy: Basic Principles*. Springer, 4th edition.

DESGROUX, P., GASNOT, L., PAUWELS, J.F. & SOCHET, L.R. (1995). Correction of LIF temperature-measurements for laser-absorption and fluorescence trapping in a flame - application to the thermal perturbation study induced by a sampling probe. *Applied Physics B,* **61**, 401.

DESGROUX, P., MERCIER, X., LEFORT, B., LEMAIRE, R., THERSSEN, E. & PAUWELS, J.F. (2008). Soot volume fraction measurement in low-pressure methane flames by combining laser-induced incandescence and cavity ring-down spectroscopy: Effect of pressure on soot formation. *Combustion and Flame,* **155,** 289.

DEVERALL, G.V., MEISSNER, K.W. & ZISSIS, G.J. (1953). Hyperfine structures of the resonance lines of indium (In115). *Physical Review*, **91**, 297.

DOCKERY, D.W., POPE, C.A., XU, X., SPENGLER, J.D.,WARE, J.H., FAY, M.E., FERRIS, B.G.& SPEIZER, F.E.N. (1993). An association between air-pollution and mortality in 6 united-states cities. *The New England Journal of Medicine,* **329**, 1753.

DOWLING, A.P (March, 2000). Vortices, Sound and Flame – a damaging combination, *The Aeronautical Journal of the RaeS*.

DOWLING, A.P. (May, 2000). Active control of instabilities in gas turbines. *RTO VT Symposium on 'Active control technology for enhanced performance operational capabilities of military aircraft, land vehicles and sea vehicles, Branunschweig, Germany, RTO MP-051*.

DREIZLER, A., LINDENMAIER, S., MAAS, U., HULT, J., ALDEN, M. & KAMINSKI C.F. (2000). Characterisation of a spark ignition system by planar laser-induced fluorescence of OH at high repetition rates and comparison with chemical kinetic calculations. *Applied Physics B*, **70(2)**, 287.

DRUET, S. & TARAN, J.P. (1981). CARS spectroscopy. *Progress in Quantum Electronics*, **7**, 1.

DURANT, J.L., BUSBY, W.F., LAFLEUR, A.L., PENMAN, B.W. & CRESPI, C.L. (1996). Human cell mutagenicity of oxygenated, nitrated and unsubstituted polycyclic aromatic hydrocarbons associated with urban aerosols. *Mutation Research,* **371,** 123.

EBERZ, J., HUBER, G., KUHL, T. & ULM, G. (1984). Pressure Broadening and Pressure Shift of the 410-nm Indium Line Perturbed by Foreign Gases. *Journal of Physics B-Atomic Molecular and Optical Physics,* **17,** 3075.

ECHEKKI, T. & CHEN, J. (1996). Unsteady strain rate and curvature effects in turbulent premixed methane/air flames. *Combustion and Flame*, **106**, 184202.

ECKBRETH, A. & HALL, R. (1981). CARS concentration sensitivity with and without non-resonant background suppression. *Combustion Science and Technology,* **25(5),** 175.

ECKBRETH, A. (1996). *Laser Diagnostics for Combustion Temperature and Species*. Gordon & Breach Publishers.

EISNER, A. & ROSNER, D. (1985). Experimental studies of soot particle thermophoresis in non-isothermal combustion gases using thermocouple response techniques. *Combustion and Flame,* **61**, 153.

ELDER, M., ZIZAK, G., BOLTON, D., HORVATH, J. & WINEFORDNER, J. (1984). Single pulse temperature measurements in flames by thermally assisted atomic fluorescence spectroscopy. *Applied Spectroscopy,* **38,** 113.

ENGSTRÖM, J., NYGREN, J., ALDÉN, M. & KAMINSKI, C.F. (2000). Two-line atomic fluorescence as a temperature probe for highly sooting flames. *Optics Letters,* **25**, 1469.

FAYOUX, A., ZAHRINGER, K., GICQUEL, O., ROLON, J.C. (2004). Experimental and numerical determination of heat release in counterflow premixed laminar flames. *Proceedings of the Combustion Institute*, **30(1)**, 251.

FRANK, J.H. & SETTERSTEN, T.B. (2005). Two-photon LIF imaging of atomic oxygen in flames with picosecond excitation. *Proceedings of the Combustion Institute,* **30**, 1527.

GASHI, S., HULT, J., JENKINS, K.W., CHAKRABORTY, N. & CANT, R.S. (2005) Curvature and wrinkling of premixed flame kernels—comparison of OH PLIF and DNS data. *Proceedings of the Combustion Institute,* **30,** 809.

GLASSMAN, I. (1996). *Combustion*. Academic Press, 3rd edn.

GORDON, R.L., MASRI, A.R. & MASTORAKOS, E. (2009). Heat release rate as represented by [OH] x [CH2O] and its role in auto-ignition, *Combustion Theory and Modelling*, **13,** 645.

GUO, Z.M., ZHANG, H.Q., CHAN, C.K. & LIN, W.Y. (2003). Presumed joint probability density function model for turbulent combustion. *Fuel*, **82**, 1091.

HAQ, M.Z., SHEPPARD, C.G.W., WOOLLEY, R., GREENHALGH, D.A. & LOCKETT, R. D. (2002) Wrinkling and curvature of laminar and turbulent premixed flames. *Combustion and Flame,* **131,** 1.

HARTLIEB, A.T., ATAKAN, K. & KOHSE-HÖINGHAUS, K. (2000). Temperature measurement in fuel-rich non-sooting low-pressure hydrocarbon flames *Applied Physics B,* **70**, 435.

HARTUNG, G., HULT, J. & KAMINSKI, C.F. (2006) A flat flame burner for the calibration of laser thermometry techniques. *Measurement Science and Technology*, **17,** 2485.

HARTUNG, G., HULT, J. BALACHANDRAN, R., MACKLEY, M.R., KAMINSKI, C.F. (2009) Flame front tracking in turbulent lean premixed flames using stereo PIV and time-sequenced planar LIF of OH. *Applied Physics B,* **96,** 843.

HARTUNG, G., HULT, J.F., KAMINSKI, C.F, ROGERSON, J.W. & SWAMINATHAN, N. (2008). Effect of heat release on turbulence and scalar-turbulence interaction in premixed combustion. *Physics of Fluids,* **20**, 035110.

HAYASHIDA, K. (2005). LIF thermometry in sooty flames using NO D-2 Sigma(+) <- X-2 Pi(0,1) and OH A(2)Sigma(+) <- X-2 Pi(3,0) bands. *Energy*, **30**, 497.

HAYHURST, A. & KITTELSON, D. (1977). Heat and mass transfer considerations in use of electrically heated thermocouples of iridium versus an iridium-rhodium alloy in atmospheric-pressure flames. *Combustion and Flame,* **28,** 301.

HAYNES, B.S., & WAGNER, H. (1981). Soot formation. *Progress in Energy and Combustion Science,* **7**, 229.

HERZBERG, G. (1950). *Molecular Spectra and Molecular Structure*. New York, Van Nostrand Reinhold.

HILBERT, R., TAP, F., EL-RABII, H. & THÉVENIN, D. (2004). Impact of detailed chemistry and transport models on turbulent combustion simulations. *Progress in Energy and Combustion Science*, **30**, 61117.

HULT, J., BURNS, I.S. & KAMINSKI, C.F. (2004). Measurements of the indium hyperfine structure in an atmospheric-pressure flame by use of diode-laser-induced fluorescence. *Optics Letters,* **29**, 827.

HULT, J., BURNS, I.S. & KAMINSKI, C.F. (2005). Two-line atomic fluorescence flame thermometry using diode lasers. *Proceedings of the Combustion Institute,* **30**, 1535.

INCROPERA, F.P. & DE WITT, D.P. (1996). *Fundamentals of heat and mass transfer.* John Wiley and Sons, New York.

JOKLIK, R.G. & DAILY, J.W. (1982). 2-line atomic fluorescence temperature-measurement in flames – an experimental study. *Applied Optics,* **21**, 4158.

JU, Y., MATSUMI, H., TAKITA, K. & MASUYA, G. (1998). Combined effects of radiation, flame curvature, and stretch on the extinction and bifurcations of cylindrical CH4/Air premixed flame. *Combustion and Flame*, **116**, 580592.

KADOWAKI, S. & HASEGAWA, T. (2005). Numerical simulation of dynamics of premixed flames: flame instability and vortex-flame interaction. *Progress in Energy and Combustion science*, **31(3)**, 193.

KEE, R.J., GRCAR, J.F., SMOOKE, M.D. & MILLER, J.A. (1985) *Sandia Report* **SAND 85-8240**, Sandia National Laboratories.

KOHSE-HÖINGHAUS, K. & JEFFRIES, J. (2002). *Applied Combustion Diagnostics,* Combustion: An International Series, Taylor and Francis.

KRONEMAYER, H., IFEACHO, P., HECHT, C., DREIER, T., WIGGERS, H. & SCHULZ, C. (2007). Gas-temperature imaging in a low-pressure flame reactor for nano-particle synthesis with multi-line NO-LIF thermometry. *Applied Physics B*, **88,** 373.

KYCHAKOFF, G., HOWE, R.D. & HANSON, R.K., (1984). Spatially resolved combustion measurements using cross-beam saturated absorption spectroscopy. *Applied Optics*, **23**, 303.

KYCHAKOFF, G., PAUL, P.H., VANCRUYNINGEN, I. & HANSON, R.K., (1987). Movies and 3-d images of flowfields using planar laser-induced fluorescence. *Applied Optics,* **26,** 2498.

LAW, C.K. (1988). Dynamics of stretched flames. *Proceedings of the Combustion Institute,* **22,** 1381.

LEE, M.P., PAUL, P.H. & HANSON, R.K. (1987). Quantitative imaging of temperature-fields in air using planar laser-induced fluorescence of O_2. *Optics Letters,* **12,** 75.

LEE, S. & CHEN, I. (1996). Axis switching in the (B)overtilde(2) A'(X)overtilde(2)A' transition of HCO and fluorescence lifetimes of the (B)overtilde(2)A'(0,0,0) rotational states. *Journal of Chemical Physics*, **105**, 25832590.

LIEUWEN, T., NEUMEIER, Y. & ZINN, B.T. (1998). The role of un-mixedness and chemical kinetics in driving combustion instabilities in lean premixed combustors. *Combustion Science and Technology,* **135** 193.

LINNEKEN, H. (1977). Viscosity-Temperature behaviour of gases at moderate pressure. *Forschung im Ingnieurwesen*, **43(1),** 19.

LUQUE, J. & CROSLEY, DR. (1999). Transition probabilities and electronic transition moments of the A (2)Sigma(+)-X (2)Pi and D (2)Sigma(+)-X (2)Pi systems of nitric oxide, *Journal of Chemical Physics*, **111**, 7405.

LYONS, K.M., WATSON, K.A., CARTER, C.D., DONBAR, J.M. (2007). Upstream islands of flame in lifted-jet partially premixed combustion. *Combustion Science and Technology,* **179,** 1029.

MANTEL, T. & SAMANIEGO, J. (1999). Fundamental mechanisms in premixed turbulent flame propagation via. vortex-flame interactions Part I: Experiment. *Combustion and Flame*, **118**, 537556.

MANTEL, T. & SAMANIEGO, J. (1999). Fundamental mechanisms in premixed turbulent flame propagation via vortex-flame interactions Part II: Numerical Simulation. *Combustion and Flame*, **118**, 557582.

MASTORAKOS, E. (2009). Ignition of turbulent non-premixed flames. *Progress in Energy and Combustion Science*. **35**, 57.

MCQUARRIE, D. (2000). *Statistical Mechanics*. University Science Books, 2nd edition.

MEDWELL, P., CHAN, Q., KALT, P., ALWAHABI, Z., DALLY,. B. & NATHAN, G. (2009). Development of temperature imaging using two-line atomic fluorescence. *Applied Optics,* **48**, 1237.

MERCIER, X., PILLIER, L., EL-BAKALI, A., CARLIER, M., PAUWELS, J.F., DESGROUX, P. (2001). NO reburning study based on species quantification obtained by coupling LIF and cavity ring-down spectroscopy. *Faraday Discussions,* **119**, 305.

MEYER, T.R., ROY, S., ANDERSON, T.N., MILLER, J.D., KATTA, V.R., LUCHT, R.P. & GORD, J.R. (2005). Measurements of OH mole fraction and temperature up to 20 kHz by using a diode-laser-based UV absorption sensor. *Applied Optics,* **44,** 6729.

MILLS, I., CVITAS, T., HOMANN, K., KALLAY, N. & KUCHITSU, K. (1988). *Quantities, Units and Symbols in Physical Chemistry*. Oxford, UK, Blackwell Scientific Publications.

MORLEY, C. (1997). *Gaseq: Chemical equilibria in perfect gases*. Version 0.77a.

MUSICK, M., VAN-TIGGELEN, P.J., VANDOOREN, J. (1996). Experimental study of the structure of several fuel-rich premixed flames of methane, oxygen, and argon. *Combustion and Flame,* **105,** 433.

NAJM, H. & WYCKOFF, P. (1997). Premixed flame response to unsteady strain rate and curvature. *Combustion and Flame*, **110**, 92112.

NAJM, H., PAUL, P., MUELLER, C. & WYCKOFF, P. (1998). On the adequacy of certain experimental observables as measurements of flame burning rate. *Combustion and Flame*, **113**, 312332.

NEFEDOV, A.P., SINEL'SHCHIKOV, V.A. & USACHEV, A.D. (1999). Collisional broadening of the Na-D lines by molecular gases. *Physica Scripta,* **59(6),** 432.

NYGREN, J., ENGSTROM, J., WALEWSKI, J., KAMINSKI, C.F. & ALDEN, M., (2001). Applications and evaluation of two-line atomic LIF thermometry in sooting combustion environments. *Measurement Science & Technology,* **12,** 1294.

OMENETTO, N., BENETTI, P. & ROSSI, G. (1972). Flame temperature measurements by means of atomic fluorescence spectrometry. *Spectrochimica Acta Part B-Atomic Spectroscopy,* **B27,** 453.

ÖTTINGER, H. (2005). *Beyond Equilibrium Thermodynamics*. Wiley.

PALMER, J.L. & HANSON, R.K. (1996). Temperature imaging in a supersonic free jet of combustion gases with two-line OH fluorescence. *Applied Optics,* **35**, 485.

PARAMESWARAN, T. & SNELLING, D.R. (1996). Effect of spatial averaging on CARS derived temperatures. *Combustion and Flame,* **106**, 511.

PAUL, P. & NAJM, H. (1998). Planar laser induced fluorescence imaging of flame heat release rate. *Proceedings of the Combustion Institute,* **27**, 4350.

PEALAT, M., BOUCHARDY, P., LEFEBVRE, M. & TARAN, J.P. (1985). Precision of multiplex CARS temperature measurements. *Applied Optics*, **24(7),** 1012.

PETERSON, K.A. & OH, D.B. (1999) High sensitivity detection of CH radicals in flames by use of a diode-laser based near ultraviolet light source. *Optics Letters,* **24,** 667.

PITSCH, H. (2002). A G-equation formulation for large eddy simulation of premixed turbulent combustion, *Centre for Turbulence Research Annual Research Briefs*, 314.

QIN, W., CHEN, Y.L. & LEWIS, J.W.L. (2005). Time-resolved temperature images of laser-ignition using OH two-line laser induced fluorescence (LIF) thermometry. *Tech. Rep. Article Number 200508, IFRF Combustion Journal*.

RENARD, P., THÉVENIN, D., ROLON, J. & CANDEL, S. (2000). Dynamics of flame/vortex interactions. *Progress in Energy and Combustion Science*, **26**, 225282.

RENOU, B,, BOUKHALFA, A., PEUCHBERTY, D. & TRINITÉ, M. (2000). Local scalar flame properties of freely propagating premixed turbulent flames at various Lewis numbers. *Combustion and Flame,* **123,** 507.

RICHTER, H. & HOWARD, J.B. (2000). Formation of polycyclic aromatic hydrocarbons and their growth to soot - a review of chemical reaction pathways. *Progress in Energy and Combustion Science,* **26**, 565.

RUTLAND, C. & FERZIGER, J. (1991). Simulations of flame vortex interactions. *Combustion and Flame*, **84**, 343360.

RUTLAND, C. & TROUVÉ, A. (1993). Direct simulations of premixed turbulent flames with non unity lewis numbers. *Combustion and Flame*, **94**, 4157.

SEEGER, T. & LEIPERTZ, A. (1996). Experimental comparison of single-shot broadband vibrational and dual-broadband pure rotational coherent anti-Stokes Raman scattering in hot air. *Applied Optics,* **35,** 2665.

SEEGER, T., WEIKL, M.C., BEYRAU, F. & LEIPERTZ, A. (2006). Identification of spatial averaging effects in vibrational CARS spectra. *Journal of Raman Spectroscopy,* **37**, 641.

SEITZMAN, J.M., HANSON, R.K., DEBARBER, P.A. & HESS, C.F. (1994). Application of quantitative two-line OH planar laser-induced fluorescence for temporally resolved planar thermometry in reacting flows. *Applied Optics,* **33**, 4000.

SHEPHERD, I., PORTER, F.M. & GREENHALGH, D.A. (1990). Spatial Resolution of CARS in Turbulent Premixed Combustion Thermometry. *Combustion and Flame,* **82**, 106.

SHY, S.S., LEE, E.I. & YANG, T.S. (1999) Experimental analysis of flame surface density modelling for premixed turbulent combustion using aqueous autocatalytic reactions. *Combustion and Flame,* **118,** 606.

SNELLING, D., SMALLWOOD, G., SAWCHUK, R. & PARAMESWAREN, T. (1987). Precision of multiplex CARS temperatures using both single-mode and multimode pump lasers. *Applied Optics*. **26(1),** 99.

SOIKA, A., DINKELACKER, F. & LEIPERTZ, A. (2003). Pressure influence on the flame front curvature of turbulent premixed flames: comparison between experiment and theory. *Combustion and Flame,* **132,** 451.

STEELE, R.C., MALTE, P.C., NICHOL, D.G., & KRAMLICH, J.C. (1995). NO_x and N_2O in Lean-Premixed Jet-Stirred Flames. *Combustion and Flame* **100**, 440.

STERN, N. (2006). *Stern Review on The Economics of Climate Change. Executive Summary*. HM Treasury, London.

TAMURA, M., LUQUE, J., HARRINGTON, J.E., BERG, P.A., SMITH, G.P. & CROSLEY, D.R. (1998). Laser-induced fluorescence of seeded nitric oxide as a flame thermometer. *Applied Physics B,* **66**, 503.

TH, C. & ALKEMADE, J. (1972). *Flame Emission and Atomic Absorption Spectrometry*, Marcel Dekker, New York.

THUMANN, A., SEEGER, T. & LEIPERTZ, A. (1995) Evaluation of two different gas temperatures and their volumeric fraction from broadband N_2 coherent anti-Stokes Raman spectroscopy spectra. *Applied Optics,* **34(18),** 3313.

TSUJISHITA, M. & HIRANO, A. (1996). Two-dimensional quenching lifetime measurement of OH:A(2)Sigma(+)(v'=1) and NO:A(2)Sigma(v'=0) in atmospheric-pressure flames. *Applied Physics B,* **62**, 255.

TURNS, S. (2000). *An Introduction to Combustion.* McGraw-Hill, USA, 2nd edn.

UPATNIEKS, A., LABERTEAUX, K. & CECCIO, S.L. (2002). A kilohertz frame rate cinemagraphic PIV system for laboratory-scale turbulent and unsteady flows. *Experiments in Fluids,* **32,** 87.

VEYNANTE, D. & VERVISCH, L. (2002). Turbulent Combustion Modelling, *Progress in Energy and Combustion Science*, **28,** 193.

WANG, G., CLEMENS, N. & VARGHESE, P. (2005). Two-point, high –repetition-rate Rayleigh thermometry in flames: techniques to correct for apparent dissipation induced by noise. *Applied Optics,* **44,** 6741.

WANG, G.H. & BARLOW, R.S. (2008). Spatial resolution effects on the measurement of scalar variance and scalar gradient in turbulent non premixed jet flames. *Experiments in Fluids,* **44**, 633.

WARNATZ, J., MASS, U., & DIBBLE, R.W. (1996). *Combustion*. Springer-Verlag, Berlin Heidelberg, New York.

WILLIAMS, F.A. (1986) *Combustion Theory: The Fundamental Theory of Chemically Reacting Flow Systems,* Reading, MA: Addison-Wesley.

ZILWA, S.R.N., UHM, J.H. & WHITELAW, J.H. (2000). Combustion oscillations close to the lean flammability limit. *Combustion Science and Technology*. **160,** 231.

ZIZAK, G., OMENETTO, N. & WINEFORDNER, J.D. (1984). Laser-excited atomic fluorescence techniques for temperature-measurements in flames – a summary. *Optical Engineering*, **23**, 749.